Mixed-fidelity CFD Simulations for Aero-engines

A Fan-intake Interaction Study

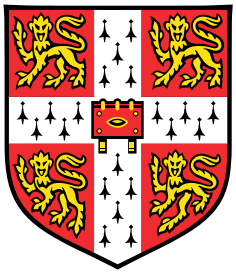

Ma, Yunfei

Department of Engineering
University of Cambridge

This dissertation is submitted for the degree of
Doctor of Philosophy

Churchill College March 2019

Declaration

This thesis is the result of my own work conducted in the Department of Engineering, University of Cambridge, from April 2016 to March 2019. It includes nothing which is the outcome of work done in collaboration except as declared in the Preface and specified in the text. It is not substantially the same as any that I have submitted, or, is being concurrently submitted for a degree or diploma or other qualification at the University of Cambridge or any other University or similar institution except as declared in the Preface and specified in the text. I further state that no substantial part of my thesis has already been submitted, or, is being concurrently submitted for any such degree, diploma or other qualification at the University of Cambridge or any other University or similar institution except as declared in the Preface and specified in the text. It does not exceed the prescribed word limit for the relevant Degree Committee.

Ma, Yunfei
March 2019

Acknowledgements

I would like to express my great appreciation to Prof Paul Tucker and Dr Xu Liping. Their in-depth knowledge and extraordinary wisdom enlightened me; their careful, well-organised guidance and encouragement also ensure the quality and creativity of the research. Thanks to their help, I can finish the project in time.

Cambridge life is far more exciting and rewarding than I expected. I would like to describe it as a combination of "Opportunities of time vouchsafed by Heaven, advantages of situation afforded by the Earth, the union arising from the accord of Men" (天时地利人和), quoted from Mencius. The idea of the project was inspired by actual industrial needs, the research was finished in a comfortable, friendly environment, and numerous supports from my colleagues also contributed substantially. Dr Nagabhushana Rao Vadlamani reviewed my first paper sentence by sentence and provided very insightful suggestions. Dr Cui Jiahuan generously provided his URANS data for validation and constructive discussion about coding in HYDRA. Dr Rob Watson paved the way for building IBM framework in the code and helped me a lot in many technical issues. Dr Ashley Scillitoe kindly shared his profound knowledge of turbulence modelling. Dr Zhong-Nan Wang carefully advised a wide variety of numerical techniques. Mr Bryn Ubald offered his warm-hearted and expert help in mesh morphing. Mr Will Trojak gave his very professional comments at every corner on each slide before an important academic presentation. Dr James Tyacke, as the most senior leader in the lab, suggested many promising applications of the proposed method and sent me impressive CFD pictures. Prof Liu Yangwei, during his visit to the lab, significantly contributed a range of innovative ideas for the research. Dr Cao Teng, also my senior alumnus in BUAA, equipped me with his expertise in turbomachinery. Mr Sun Wei recommended his valuable studies for reviewing turbulence modelling. These talented colleagues are the precious wealth for the lab and for my career. A famous poet, Wang Bo from my home province said, "A bosom friend afar brings a distant land near" (海内存知己，天涯若比邻). I really cherish the friendship with them. I should also appreciate the very high quality of language training provided by the university

language centre and language unit in the department. Without their help, my English writing and speaking skills could not progress so greatly.

During my study, Churchill College also offered an amazing place to live: three year accommodation, a vast grassland, exquisite gardens, free banquets, piano rooms, etc. Many students from the world top universities, including mathematicians, physicians, historians, musicians and anthropologies also inspired me in the leisure time. Thanks to my college and non-college mates, especially (in the surname order to avoid any conflicts) Andrew Ballin, James Bevan, Marya Chebysheva, Chen Hao, Chow Chun Man, Simon Corkery, Ding Bowen, Alexander Hannon, Li Benxuan, Liu Xuanzuo, Lyu Benshuai, Chiara Monaco, Bill Moriarty, Ou Zhiyuan, Qiao Yujun, Matthew Robinson, Simon Schäfer, Sun Mengchen, Xiang Xue, etc. They occupied my non-working hours but made it very enjoyable. In the department, I was immersed in a very English lab, speaking British English and playing British jokes, whereas back to the college, highly influenced by other Chinese, European and American cultures. The college mates taught me how to cook southern Chinese, British, Italian, Spanish and 'Immigration countries' food, how to understand British and American talk shows and jokes, how to do Scottish and Irish dancing, how to drive a manual car at midnight, how to row in a river full of other competitors, etc.

In these fruitful years, many academic or non-academic trips also offered me a great opportunity to explore the Europe and North America, and to have an insight into this western hemisphere. I travelled more than 200,000 kilometres, 300 hours in the air, and 25 countries in three continents. These visits include 16 great universities (Harvard, MIT, Stanford, Caltech, UC Berkeley, Oxford, Imperial College, University of Edinburgh, ETH, EPFL, KTH, HU Berlin, ParisTech, Trinity College Dublin, University of Copenhagen, Sapienza University of Rome), 14 great concert/opera halls (Royal Albert Hall, Sheldonian Theatre, Royal Festival Hall, Queen's Theatre, Palais Garnier, Teatro la Fenice, Teatro alla Scala, Wiener Musikverein, Vienna Staatsoper, Konzerthaus Berlin, Semperoper Dresden, Rudolfinum Prague, Boston Symphony Hall, Hollywood Bowl), mountains/rivers/lakes/glaciers that nurtured different cultures or triggered wars, and palaces/castles/fortresses where influential families and heroes came and left. The complicated Western story line from Athens, to Rome, to Venice, to Seville, to Paris, to Berlin, to Vienna, to London, to Boston, to San Francisco, attracted me to learn how the cultures, sciences and thoughts were developed till now, via books and feet.

Finally, I should give my special thanks to my parents Mr Ma Hailin and Mrs Huo Yuchuan, and my brother Huo Pengfei, for their endless support! The financial support

from the China Scholarship Council, the Ford of Britain Fund, and the Churchill College Travel Grants, the computational resources from UKTC and the Cambridge HPC centre are gratefully acknowledged.

Abstract

Mixed-fidelity CFD Simulations for Aero-engines: A Fan-intake Interaction Study

Ma, Yunfei

Engine system consists of complex components, where aerodynamics can be coupled. In these coupled problems, flow separation may exist and the multiscale turbulence needs to be finely resolved to obtain an accurate solution. A high-fidelity simulation in such scenarios, however, is still infeasible for industrial applications due to the limitation of current computational resources. To make it possible, a mixed-fidelity CFD method based on the Immersed Boundary Method (IBM) is proposed. In this hierarchical method, geometries can be replaced by forces, i.e. the standard IBM or eIBM, whereas turbulence can be resolved by the Large Eddy Simulation. The thesis proposed this method and applied it to an important issue for engine design: fan-intake interaction. The method was validated on a Darmstadt Transonic Rotor with a distortion generator to replicate the unsteady distortion at incidence, the NASA Rotor 67 with steady pressure distortion, and a triangular prism for turbulence statistics. The results indicated that this method can accurately simulate the performance map, separation transfer and total pressure distributions, compared to the experimental data and Direct Mesh Resolved (DMR) case. The method was then applied to reveal the mechanism of fan influence on intake distortion. It was shown that there are two aspects of such influence: the suction effect of a fan can accelerate the flow in the upstream and directly change its streamline curvature; on the other hand, the recirculating flows can also intensify the turbulence, indirectly increase the mixing process and finally alleviate the distortion. The main flow effect was further investigated in different parameters of fan type, location and distortion size. Results showed that a tip-loaded fan is more effective in suppressing intake separation; a nearer fan to the upstream has more significant reduction of distortion; a greater distortion can be suppressed more. These results demonstrate that a fan can be an essential component for intake distortion control. Further investigations of the results from RANS and LES interpreted the

dominance of the influence via main flow or turbulence. It was found that stronger main flow acceleration by a fan can mitigate the inaccuracy of turbulence models. This indicates that for a short intake design, conventional turbulence models may be capable of predicting flow separation.

List of Contributions

Journal Papers

1. Ma, Y., Cui, J., Vadlamani, N. R., and Tucker, P. (2018). Effect of Fan on Inlet Distortion: Mixed-fidelity Approach. AIAA Journal, 56(6):2350–2360.
   DOI: 10.2514/1.J056858

2. Ma, Y., Cui, J., Vadlamani, N. R., and Tucker, P. (2018). A Mixed-fidelity Numerical Study for Fan–distortion Interaction. ASME. J. Turbomach., 140(9):091003.
   DOI: 10.1115/1.4040860

3. Ma, Y., Vadlamani, N. R., Cui, J., and Tucker, P. G. (2018, December). Comparative Studies of RANS versus LES for Fan-intake Interaction. ASME. J. Fluids Eng.
   DOI: 10.1115/1.4041393

4. Ma Y, Cui J, Vadlamani N R, et al. Hierarchical geometry modelling using the immersed boundary method. Computer Methods in Applied Mechanics and Engineering, 2019, 355: 323-348.
   DOI: 10.1016/j.cma.2019.06.019

5. Cui, J., Watson, R., Ma, Y., and Tucker, P. (2019). Low Order Modeling for Fan and Outlet Guide Vanes in Aero-Engines. ASME. J. Turbomach., 141(3), 031002.
   DOI: 10.1115/1.4042202

6. Tyacke, J., Vadlamani, N. R., Trojak, W., Watson, R., Ma, Y., and Tucker, P. G. (2019). Turbomachinery simulation challenges and the future. Progress in Aerospace Sciences, 100554.
   DOI: 10.1016/j.paerosci.2019.100554

Conference Papers

1. Ma, Y., Cui, J., Vadlamani, N. R., and Tucker, P. (April, 2019). Filtered geometry modelling for fan-intake interaction based on the immersed boundary method. European Turbomachinery Conference 13, Lausanne, Switzerland.

2. Ma, Y., Cui, J., Vadlamani, N. R., and Tucker, P. (June 2018). A Mixed-Fidelity Numerical Study for Fan-Distortion Interaction. ASME Turbo Expo 2018: Turbomachinery Technical Conference and Exposition, Lillstrøm, Norway.

3. Ma, Y., Cui, J., Vadlamani, N. R., and Tucker, P. (September, 2018). Mixed-Fidelity Studies for the Fan Effect via Turbulence and Main Flow. ISUAAAT15, Oxford, UK.

4. Ma, Y., Cui, J., Vadlamani, N. R., and Tucker, P. (December, 2017). Effect of Fan on Inlet Distortion: Mixed-fidelity Approach. ISROMAC 2017, Maui, Hawaii.

5. Cui, J., Ma, Y., Ubald, B. Tucker, P. (December, 2017). Multi-fidelity simulation for a transonic compressor with inflow distortions. ISROMAC 2017, Maui, Hawaii.

6. Watson, R., Cui, J., Ma, Y., et al. (June, 2017). Improved Hierarchical Modelling for Aerodynamically Coupled Systems. ASME Turbo Expo 2017: Turbomachinery Technical Conference and Exposition, Charlotte, NC, USA.

Table of Contents

List of Contributions **xi**

List of Figures **xvii**

List of Tables **xxi**

Nomenclature **xxiii**

1 Introduction **1**
1.1 Next-generation Engine Design 1
1.2 Challenges for Engine Simulations 3
1.3 Mixed-fidelity Method 5
1.4 Objectives 6
1.5 Scope 7

2 Literature Review **9**
2.1 Fan-intake Interaction 9
2.2 Turbulence Simulations for Flow Separation 11
2.2.1 Defects of Turbulence Modelling Approach 12
2.2.2 Applications of Eddy Resolving Approach 17
2.2.3 Limitations of Eddy Resolving Approach 19
2.3 Geometry Representation 22
2.3.1 Immersed Boundary Method 22
2.3.2 Body Force Models 24
2.4 Concluding Remarks 26

3 Methodology **29**
3.1 Geometry Modelling 29
3.1.1 Standard IBM 29

3.1.2 Euler IBM . . . 30
3.2 Turbulence Modelling . . . 36
3.2.1 Navier–Stokes Equations . . . 36
3.2.2 RANS . . . 37
3.2.3 URANS . . . 41
3.2.4 LES . . . 41
3.3 Equation Solving . . . 45
3.3.1 Governing Equations . . . 45
3.3.2 Spatial Discretisation . . . 46
3.3.3 Temporal Discretisation . . . 49
3.3.4 Grid Technique . . . 50

4 Validation of Mixed-fidelity Method 51
4.1 Darmstadt Transonic Rotor . . . 52
4.1.1 Case Framework . . . 52
4.1.2 Performace Map . . . 53
4.1.3 Flow Features . . . 56
4.1.4 Quantitative Comparisons . . . 68
4.2 NASA Rotor 67 . . . 76
4.2.1 Case Framework . . . 76
4.2.2 Flow Features . . . 77
4.3 Triangular Prism . . . 81
4.3.1 Case Framework . . . 81
4.3.2 Flow Features and Turbulence . . . 82
4.4 Concluding Remarks . . . 84

5 Mechanisms of Fan Influence 85
5.1 Case Framework . . . 85
5.1.1 Computational Settings . . . 85
5.1.2 Geometry simplification . . . 86
5.1.3 Mesh quality . . . 87
5.2 Flow Features . . . 88
5.2.1 Instantaneous Flow Field . . . 88
5.2.2 Time-averaged Flow Field . . . 90
5.3 Turbulence Statistics . . . 90
5.4 Turbulence Structure . . . 97
5.5 Concluding Remarks . . . 101

6 Suppression of Intake Distortion 103
6.1 Case Framework . . . 103
6.2 Blade Type . . . 104
6.3 Fan location . . . 107
6.4 Inlet Distortion . . . 109
6.5 Concluding Remarks . . . 111

7 Prediction of Intake Distortion 113
7.1 Case Framework . . . 113
7.2 Distortion without Fan . . . 114
7.3 Distortion with Fan Effect . . . 114
7.3.1 Effects of Fan Location . . . 114
7.3.2 Effects of Beam Height . . . 117
7.4 Acceleration and Discrepancies . . . 120
7.5 Concluding Remarks . . . 122

8 Conclusions 125
8.1 Mixed-fidelity Method . . . 125
8.2 Fan-intake Interaction . . . 126
8.3 Future Work . . . 127

References 131

Appendix A eIBMl for Flow Frequencies 145

Appendix B Discrepancy between RANS and LES 149

List of Figures

1.1 Flow separation at an intake during landing stage, originally from Rolls-Royce . . . 2
1.2 Aircraft engine components, from Rolls-Royce . . . 2
1.3 Simulation results of various fidelity turbulence modelling approaches . . . 4
1.4 Mesh size for engine components, from Tucker [149] . . . 5
1.5 Hierarchy of turbulence and geometry modelling . . . 6
1.6 Tool sets and potential applications . . . 7

2.1 Overview of the unsteady flow phenomena in turbomachinery, and corresponding turbulence treatments, originally from Gourdain [60] . . . 12
2.2 Characteristic traces of periodic flows, from Tucker [149] . . . 12
2.3 Spectral distribution: (a) Spectral gap, required for (U)RANS (b) Spectral merging, need to be resolved, originally from Tucker [149] . . . 16
2.4 Force distribution by (a) standard IBM, (b) Body Force Method . . . 22

3.1 Euler IBM with local force . . . 34
3.2 Control volume for interior and boundary nodes . . . 46

4.1 Full-annulus case: boundary conditions and monitored planes . . . 52
4.2 Test cases with (a) Body-fitted mesh, (b) eIBMl/eIBMg mesh, (c) Coarsened Body-fitted mesh (d) Coarsened eIBMl/eIBMg mesh (e) Force Region . . . 54
4.3 Performance map of the Darmstadt Rotor at (a) 100% speed and (b) 65% speed. SC represents Smooth Casing and B120 for a 120° beam. . . . 55
4.4 Radial distribution of mass flux from eIBMg modelling and Resolved cases, 100%RS and 16.0kg/s . . . 56
4.5 Iso-surface of Q-criterion 5×10^6, coloured by axial velocity, 100%RS and 16.0kg/s . . . 58

4.6 Distribution of total pressure at (a) Rotor upstream, (b) Stator downstream, 100%RS and 16.0kg/s 58
4.7 Distribution of (a) static pressure and (b) absolute Mach number near casing (within tip clearance), 65%RS and 10.6kg/s 59
4.8 Separation bubbles predicted by eIBMl and DMR, 65%RS and 10.6kg/s 60
4.9 Spectrum of the spatial frequencies 60
4.10 Distribution of x-vorticity induced by blade tip clearance, non-dimensionalised by U_0/H, 65%RS and 10.6kg/s 62
4.11 Static pressure coefficient on blade surfaces at midspan 63
4.12 Static pressure distribution at the blade leading edge 63
4.13 Static pressure distribution at the blade mid-chord 64
4.14 Static pressure distribution at the blade trailing edge 65
4.15 Coordinates for profiles across blade passages 66
4.16 Profiles across blade passages: (a) 10% blade span, (b) 50% blade span (c) 80% blade span, in terms of parallel velocity, static and total pressure 67
4.17 Separation region downstream the beam 69
4.18 Total pressure distribution at the rotor inlet 70
4.19 Total pressure distribution at the rotor outlet 71
4.20 Total pressure distribution at the stator outlet 72
4.21 Total pressure distribution at the hub of the stator outlet 73
4.22 Total pressure distribution at the midspan of the stator outlet 74
4.23 Total pressure distribution at the shroud of the stator outlet 75
4.24 Sketch of the numerical framework for NASA Rotor 67 77
4.25 Distribution of total pressure ratio at the mid-span plane, snapshot . . 77
4.26 Time-averaged, circumferential distributions of (a) static pressure (b) mass flux at three axial locations upstream of the rotor 78
4.27 Distributions of quantities at (a) rotor outlet and (b) stator outlet . . . 79
4.28 Circumferential distributions of total pressure ratio π_t and total temperature ratio τ_t at (a) rotor outlet (b) stator outlet 80
4.29 Sketch of flows around a triangular prism 81
4.30 Distribution of axial velocity at $x = 1Dand2D$ 82
4.31 Contours of turbulence intensity: a. experiment[4], b. DMR case, c. IBM case 83
4.32 Distribution of TKE Production at x=2D,3D,4D 83

5.1 Experiment settings for the 30° sector case 86
5.2 Inflectional points of the separation bubble 87

5.3 Mesh quality . . . 89
5.4 Flow distribution of LES cases with different grid size at $x = 4.5H$(time averaged, with fan) . . . 89
5.5 Total pressure distribution of the instantaneous flow . . . 90
5.6 Iso-surfaces of Q-criterion in different views . . . 91
5.7 Velocity profile at different streamwise locations (The blue dash-dotted line denotes the leading edge of the fan) . . . 92
5.8 Turbulent Kinetic Energy and Reynolds stresses . . . 93
5.9 TKE convection and production . . . 95
5.10 Terms of TKE Production $\langle u'v' \rangle \, \partial U/\partial y$ . . . 96
5.11 Anisotropy componentality contours: red: one-component, green: two-components, blue: isotropic . . . 98
5.12 Barycentric maps . . . 100

6.1 Sketch of the test cases for varying (a) fan-locations and (b) beam heights 104
6.2 Mesh sensitivity study from LES showing the radial variation of (a) velocity and (b) TKE at x=4.5H, without fan . . . 105
6.3 Angle distribution of the original blade and new blade . . . 105
6.4 Characteristics of original and new blades . . . 106
6.5 Effects of a fan on intake distortion . . . 106
6.6 Q-isosurfaces ($Q = 1 \times 10^7$) coloured with axial velocity for different fan-locations (a) $x = 6.2H$ and (b) $x = 7.2H$ . . . 107
6.7 Effects of different blade locations on (a) mass flux and (b) total pressure ratio . . . 108
6.8 Recovery Factor with varying (a) fan-locations and (b) beam heights . 109
6.9 Q-isosurfaces (Q=1×10^7) coloured with axial velocity for different beam heights . . . 109
6.10 Total pressure loss with increasing beam height . . . 110
6.11 Effects of different degrees of distortion on (a) mass flux and (b) total pressure ratio in the absence of fan . . . 110
6.12 Effects of different degrees of distortion on (a) mass flux and (b) total pressure ratio. 'Loc0' corresponds to the case with fan placed at $x = 5.2H$ and 'Duct' corresponds to the case without fan. . . . 111

7.1 Carpet plots comparing the (a) Velocity profiles and (b) TKE profiles between RANS and LES for the case 'Duct, H' . . . 115

7.2 Carpet plots comparing velocity profiles predicted by RANS against LES for a given distortion generator of height, H and varying fan-locations: cases (a) Loc 0 (b) Loc 1 (c) Loc 2 116
7.3 Radial distributions of (a) total pressure ratio (b) acceleration parameter (c) angle of incidence predicted by RANS and LES at x = 4.5H. Cases compared for same beam height, H and varying fan-location: Loc0, Loc1, Loc2. Test case without fan (Duct, H) is also shown. 118
7.4 Carpet plots comparing the velocity profiles predicted by RANS and LES for a given fan-location 'Loc0' and varying beam heights (a) H (b) H/2 (c) H/4 119
7.5 Radial distributions of (a) total pressure ratio (b) acceleration parameter (c) angle of incidence predicted by RANS and LES at x = 4.5H. Cases compared for same fan location, 'Loc0' and varying beam heights: H, H/2, H/4. 121
7.6 Variation of maximum discrepancy in the incidence angle $\Delta\theta^\circ$ (typically observed at the casing) with acceleration parameter for all the test cases with varying fan-locations and beam heights 122
7.7 Carpet plot comparing the prediction of TKE from LES against k-omega SST model for case Loc0, H 123
7.8 Carpet plot showing LES predictions of (a) velocity profiles and (b) TKE profiles at two different Reynolds numbers for case Loc0, H . . . 123

8.1 Modelling for a pseudo layer around fan blades 128
8.2 Sketch for the prediction of jet noise, from Tyacke [154] 129
8.3 Q-criterion for studies of blade tip clearance 130
8.4 Typical design process of aero-engines 130

A.1 22.5° sector Case: probes for flow frequency collection 146
A.2 Iso-surface of Q-criterion 1×10^6 for the sector case, coloured by static pressure 146
A.3 Separation bubbles predicted by eIBMg and eIBMl 147
A.4 Contours of the dilation in $x - r$ and $x - \theta$ domains 147
A.5 Flow frequencies around/within the separation bubble 148

B.1 Comparison of TKE profiles obtained from LES against RANS (with frozen velocity field from LES), for the case 'Duct H' 150

List of Tables

2.1 Near-wall grid requirements for DNS and LES, from Piomelli[120] . . . 20
2.2 Computational resources and number of grids and iterations needed for flows at different Reynolds number, from Slotnick [140] 20
2.3 Near-wall grid resolution parameters and their impacts, from Sagaut[120] 21

4.1 Key parameters of the Darmstadt Transonic Compressor, from Wartzek[168] 52
4.2 Main design characteristic parameters of NASA Rotor 67 76

5.1 Grid distribution 88

Nomenclature

$\boldsymbol{f}$	force
a	speed of sound
C_S	Smagorinsky constant
c_p	specific heat capacity
$\mathcal{D}e$	destruction
$\mathcal{D}i$	diffusion
$\mathcal{F}$	distribution function, flux
J_H	high-order flux
J_L	low-order flux
k	Turbulence Kinetic Energy
$\mathcal{L}$	Laplacian operator
N	the number of blade passages
n_0	unit normal vector
O	numerical order
$\mathcal{P}$	TKE production
p	pressure
n_0	unit tangential vector

$\boldsymbol{q}$	primitive quantities
R	engine inlet radius
S_{ij}	Strain tensor
S_{ij}	strain rate
$\mathcal{T}$	trip contribution
T	temperature
t	time, blade thickness
t_i	turbulence characteristic
t_p	unsteady period
$\boldsymbol{u}$	velocity
U, V	main flow velocity
u, v	velocity scalar
v_x	axial velocity
x	x coordinate
$\boldsymbol{x}_0$	body/surface coordinate
x^+	$x^+ = \frac{Ux}{\nu}$dimensionless streamwise distance
y^+	$y^+ = \frac{Uy}{\nu}$dimensionless wall distance
z^+	$z^+ = \frac{Uz}{\nu}$dimensionless spanwise distance
α,β	feedback force coeffcient
γ	heat capacity ratio
Δ	Filter width
δ	turbulence boundary layer
δ_{ij}	Kronecker delta

ϵ	Turbulence Kinetic Energy
λ	blockage factor
μ	molecular viscosity
μ_t	turbulent viscosity
ν	kinetic viscosity
Φ	smoothing function
ϕ	flow general variables
ϕ	general variables
ρ	density
σ	shear stress tensor
τ	stress
u_τ	friction velocity
Ω	specific rate of dissipation
ω	rotational speed
I	Inviscid
i, j	index
l	time level
V	viscous
C	Central difference scheme
L	left
R	right
U	Upwind scheme

ACARE Advisory Council for Aviation Research and innovation in Europe

BFM Body Force Models

CAD Computer-aided Design

CFD Computational Fluid Dynamics

CFL Courant–Friedrichs–Lewy

DMR Directly Mesh Resolving

DNS Direct Numerical Simulation

HPC High Performance Computing

eIBM Euler Immerse Boundary Method

eIBMg Euler Immerse Boundary Method with Global Force

eIBMl Euler Immerse Boundary Method with Local Force

IBM Immerse Boundary Method

KEP Kinetic Energy Perserving

LES Large Eddy Simulation

OGV Outlet Guided Vane

PIV Particle Image Velocimetry

RANS Reynolds Averaged Navier-Stoke

RHS Right Hand Side

SA Spalart-Allmaras

SAE Society of Automotive Engineers

SGS Subgrid Scale

TVD Total Variation Diminishing

URANS Unsteady Reynolds Averaged Navier-Stokes

Chapter 1

Introduction

1.1 Next-generation Engine Design

In the recent published Strategic Research and Innovation Agenda [3], ACARE has proposed ambitious technology goals in the near future, one of which is to reduce carbon emissions by 75%. Correspondingly, Rolls-Royce sets a challenging target, reducing 30% of current engine fuel consumption. To achieve this goal, the UltraFan project [130] was proposed and to be expected for launching in 2025. The project aims to improve the efficiency of core compression and turbine system and also substantially increase bypass ratio to 15:1, treble the size of Trent 700. To accommodate such a high bypass ratio, a large intake is required but on the other hand it also increases the turbulent wetted area at the same time and hence results in significant drag penalties. A common way to compensate these penalties and minimise total engine weight is to shorten the intake. However, the drawback of using a shorter intake is an intensive interaction between the downstream fan and the boundary layer development over the intake. This is particularly a difficult issue because at the landing or taxiing stage of an air plane, the rotational speed of an engine is much lower (usually by around 65% of a design speed) and the flow is prone to separate over the intake lip at an extremely high angle of incidence (Fig. 1.1). The extent of the separated flows can almost reach the intake radius [149]. Even under moderate angles of attack, Defoe [36] found that when the flow chokes within an intake, the boundary layers can be extended by up to a third of the inlet radius. As a consequence, this distorted flow is convected to the downstream and deteriorates fan performance [95]. Previous research found that the presence of a fan can have a recovery effect on inlet distortions [124]. Hence, to understand such flow physics, it is crucial to accurately simulate both the separated flow region and fan influence.

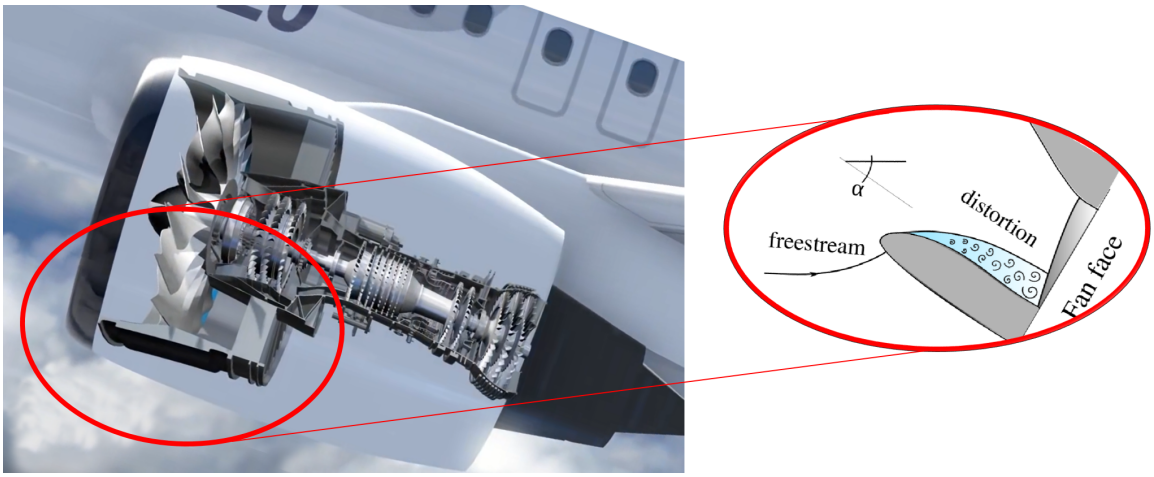

Fig. 1.1 Flow separation at an intake during landing stage, originally from Rolls-Royce

Other types of challenging flows that need to be finely resolved may also exist in the interactions of core components in aero-engines. Figure 1.2 shows the Rolls Royce UltraFan, which contains a range of components with complicated geometries: intake, fan, compressor, combustor, turbine, etc. Each component is highly influenced by the upstream/downstream parts, and thus various physical interactions may occur. For example, fan-intake interaction may substantially impact the engine performance;

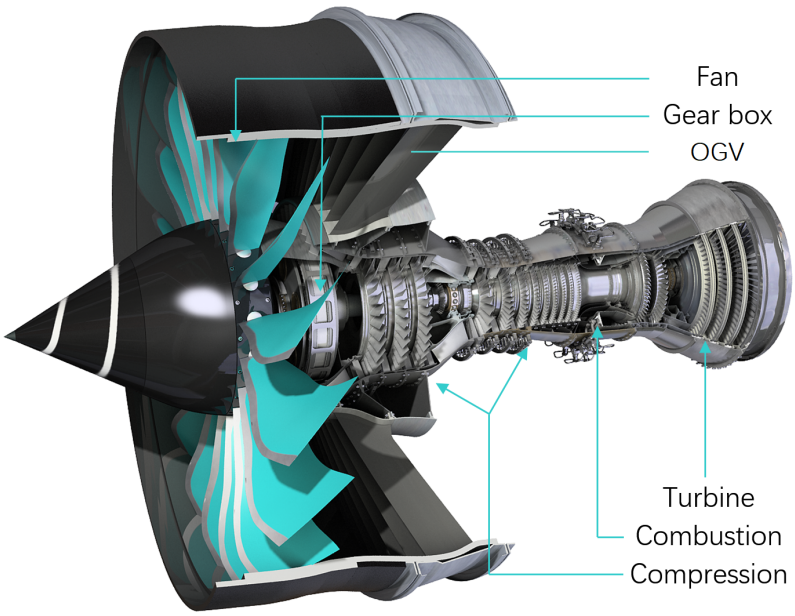

Fig. 1.2 Aircraft engine components, from Rolls-Royce

the interaction of fan-OGV and OGV-nozzle can also generate massive tonal and broadband noise. To accurately predict these phenomena and have an insight of

the physics, detailed flow information is required. It enables engineers to optimise conventional designs thus improving the performance and efficiency of a whole system. Correspondingly, a high-fidelity simulation with low costs is desired to achieve such goals. Hence, the thesis will address this issue and focus on the fan-intake interaction. The proposed method can be also potentially applied to investigate the noise within blade passages, which would be a research plan for the next stage.

1.2 Challenges for Engine Simulations

In order to simulate the flow in these scenarios accurately, conventional CFD tools with a range of RANS models are applied at the design stage. However, for aero engines under off-design conditions, flow separation can occur and hence contains multiscale turbulence. Due to well-known drawbacks of turbulence models [150], these methods may fail to provide an accurate and reliable solution for highly-unsteady separated flows. The development of turbulence models able to accurately predict complex vortical flows remains a significant challenge [93, 91]. To avoid the problems associated with modelling for complex flows, high-fidelity methods, such as DNS, LES, and hybrid RANS—LES have been applied. Such methods have been demonstrated to provide very accurate and promising results for the prediction of flow separation [92, 179], transition [124], anisotropy [1], heat transfer [60], etc. Figure 1.3 illustrates the simulation results of these different methods. It can be seen that the RANS in Frame (a) only provides very crude flow patterns, whereas when the resolution is refined from Frame (b) to (c), turbulence structures are presented in more detail by higher fidelity modelling. However, the mesh resolution requirements are very demanding. Piomelli [120] provided details concerning the near-wall requirements for DNS and LES. For example, the constraints for wall resolved LES are $x^+ = 50 \sim 130$ and $z^+ = 15 \sim 30$, compared to $x^+ \leqslant 1000, z^+ \leqslant 1000$ for RANS. This means that when simulating flows with the same Reynolds number, the grid points for LES could be as much as 20 and 60 times the size of RANS in the streamwise and spanwise directions respectively. Figure 1.4 shows the mesh requirement for different components of a typical engine [149]. For the simulation of an engine intake, the mesh size for LES could be 5×10^8. In addition, the requirement of CFL number can further increase temporal resolution significantly. Hence, limited by the current computational resources, these methods are currently infeasible for industrial applications.

One possible solution is to use hybrid RANS–LES [63], in which RANS is applied in the near wall region and LES in the far field. This could be feasible for simple

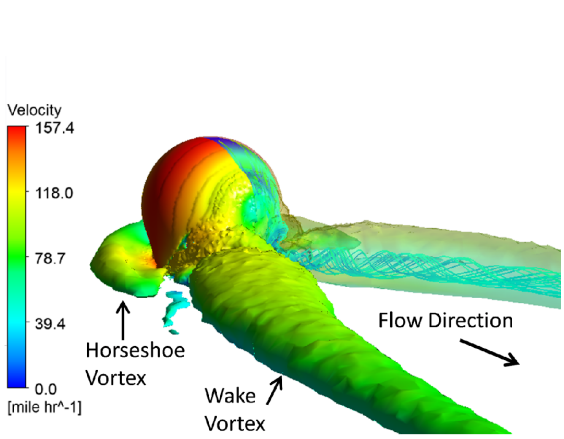

(a) RANS, from ITI RCS[125]

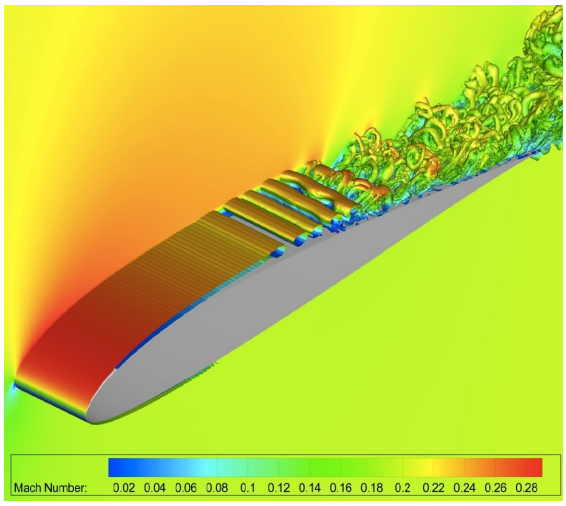

(b) Hybrid RANS-LES, from Delville [37]

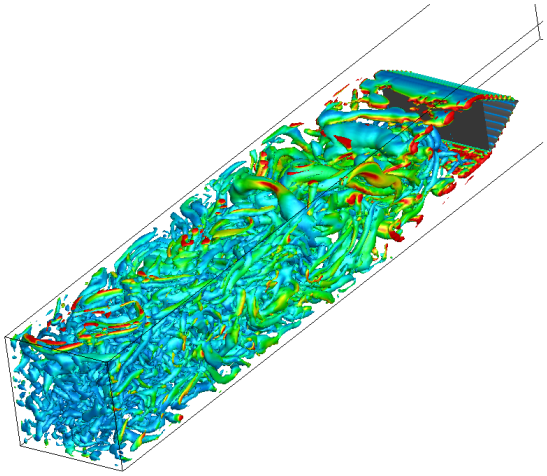

(c) LES, from Roach[127]

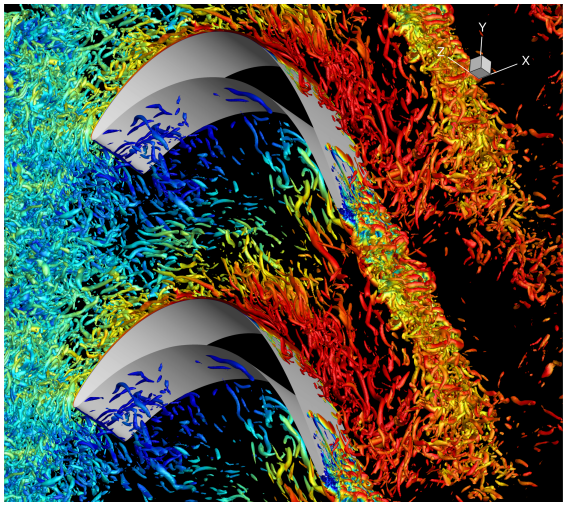

(d) DNS, from Sandberg et al.[133]

Fig. 1.3 Simulation results of various fidelity turbulence modelling approaches

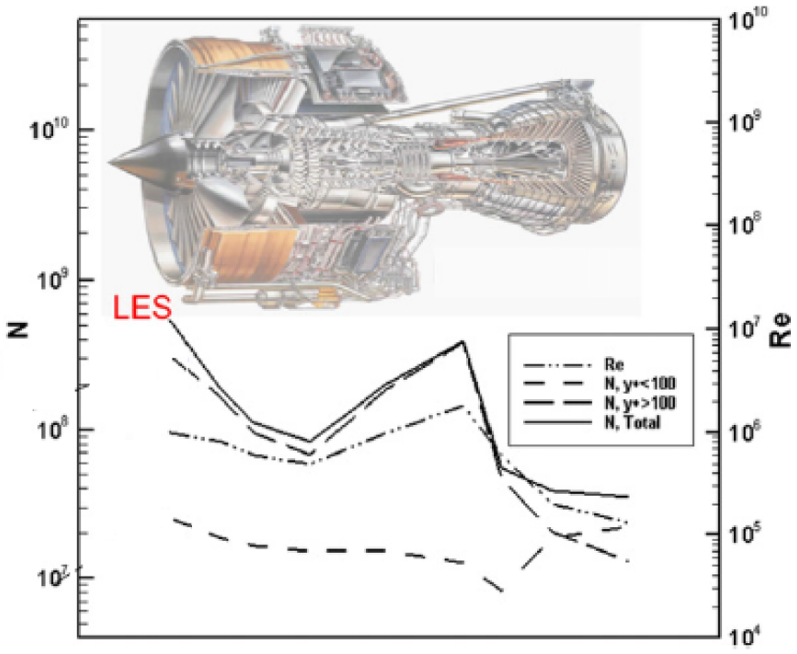

Fig. 1.4 Mesh size for engine components, from Tucker [149]

computational domains, however, complex geometries can still significantly increase the meshing and computing time. For example, components such as rotational or static blade passages, temperature/pressure probes and distortion generators need to be meshed using CAD tools and then imported into the computational domain of a CFD solver. The complexity of this process and requirement of mesh quality can be extremely high.

1.3 Mixed-fidelity Method

The thesis proposes a mixed-fidelity method that can significantly reduce computational costs whilst preserving numerical accuracy. The basic idea behind the mixed-fidelity method is to apply high-fidelity approaches to turbulent flows in the core region and low-order models as surrogates for surrounding components. It works as long as the calibrated low-order models can provide a proper boundary condition to create the same background flow.

Figure 1.5 shows the hierarchy of both turbulence and geometry modelling available for engine simulations. The previous section has discussed the performance of these turbulence modelling approaches. On the other side, the geometry modelling includes the conventional Direct Mesh Resolving (DMR), standard Immersed Boundary Method

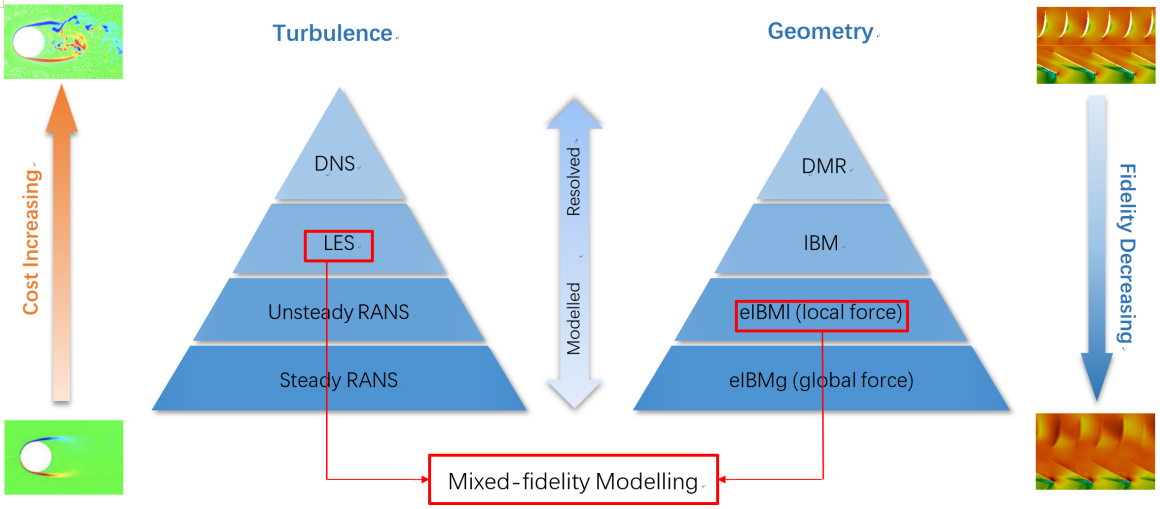

Fig. 1.5 Hierarchy of turbulence and geometry modelling

(IBM) , Euler IBM with local force and global force (eIBMl and eIBMg) . The fidelity decreases as the geometry is represented by lower order models. Details of these models and their development will be reviewed in the next chapter.

By combining the tools in each modelling hierarchy, the method mixes different fidelity techniques and creates a range of tools (Fig.1.6) for corresponding industrial needs. For example, LES+eIBMg can be applied for studying the influence of a fan on intake distortion, in which the fan is modelled by eIBMg and the turbulence within the separation is resolved by LES. This strategy can provide a powerful tool for engine optimisation heuristics, especially for those coupled problems with various flow physics. Figure 1.6 shows a tool package of this mixed-fidelity method, which contains the tools and their applications in the thesis. The present research will focus on the fan-intake interaction and apply these tools to study the mechanism, distortion suppression and numerical prediction in this context.

1.4 Objectives

The thesis provides a mixed-fidelity CFD method and explores a range of modelling approaches shown in Fig.1.6. They are applied to investigate fan-intake interaction and understand the corresponding fan performance. The aim is to optimise fan design so that the performance of an engine at high incidence can be improved. The approaches are expected to achieve high-fidelity turbulence simulations with lower costs. The research seeks to answer the following questions.

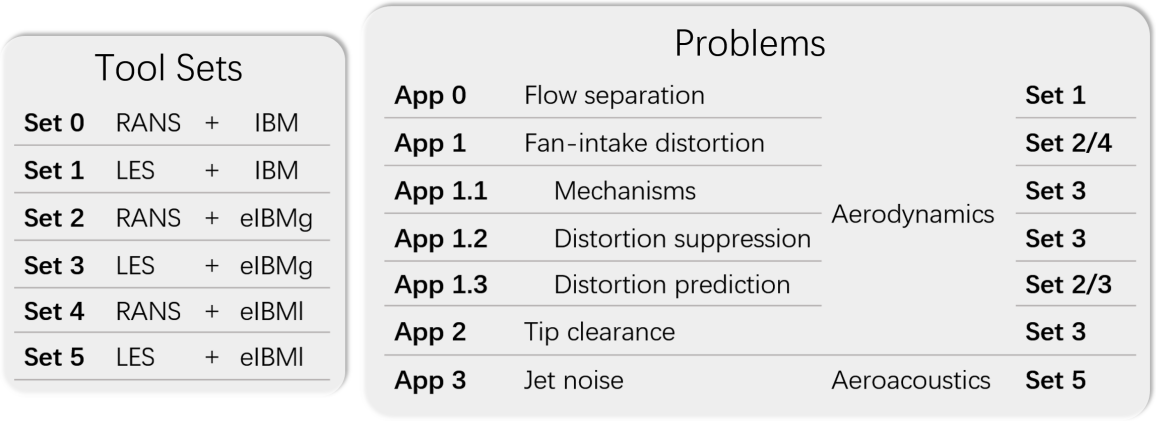

Fig. 1.6 Tool sets and potential applications

(1) How effective does such mixed-fidelity method perform for fan-intake interaction? The focus will be on the validation of the modelling approaches and discussion of their advantages and drawbacks. These methods will be tested against experiment results and their applicability will be assessed.

(2) Some research showed the presence of a fan may affect intake distortion. Thus, what is the mechanism of fan influence on intake distortion? This will be revealed by analysing the mean and turbulence characteristics computed using the mixed-fidelity method.

(3) How does the mechanism potentially instruct fan design? What are the key factors that need to be considered? Parametric studies will explore a range of fan types, fan locations and distortions.

(4) When optimising fan parameters in the scenario of high intake incidence, can turbulence modelling method like RANS achieve the same goals as eddy resolving method? What is the main influence factor for any potential discrepancies in these predictions?

1.5 Scope

This thesis is organised as follows. Chapter 2 reviews previous studies of fan-intake interaction and turbulence and geometry modelling approaches, evaluates their advantages and drawbacks and then identifies the gaps of current research on this topic. Chapter 3 introduces the approaches in this mixed-fidelity scheme and all the relevant technical details addressed in the simulations. In Chapter 4, the geometry modelling methods, including the IBM and eIBM, are validated on a Darmstadt Rotor in terms

of potential flows, and a triangular prism for turbulence information. The effectiveness of the mixed-fidelity models is discussed. With the validated method, Chapter 5 delves into the mechanism of fan influence on intake distortion, using a sector case with periodic boundary conditions derived from the Darmstadt Rotor. The mechanism is then applied to provide instructions for fan design in Chapter 6, including parametric studies of blade types, fan locations and distortion sizes. Predicted results from RANS and LES are compared in Chapter 7 and this also reveals the fan influence, i.e. flow acceleration, on the accuracy of prediction. Final conclusions and future work are discussed in Chapter 8.

Chapter 2

Literature Review

This chapter reviews the literature about both experimental and numerical studies of fan–intake interaction, the existing drawbacks of turbulence simulations and previous applications of geometry modelling. The existing problems will be highlighted and corresponding research objectives will be formed.

2.1 Fan-intake Interaction

Fan-intake interaction is a key issue for the design of both components in the aero-engine industry. This topic contains two aspects: the attenuation or suppression caused by a downstream fan, and the influence of distortion on fan performance. These are coupled problems, meaning that the change in fan performance due to the distortion may also impact the suppression process. Plourde and Stenning [121] have noted that the impact on the distortion from the change in fan performance can be neglected. Hence, this slight difference is not considered in the thesis. In terms of the types of intake distortion, a survey from Longley and Greitzer [96] concluded that the distortion in an aero-engine system can be induced by the loss of total pressure and total temperature, swirl flows or their combinations. Accordingly, the cause of the distortion discussed in fan-intake interaction can be classified as a combination of (a) unsteady shear flows induced by the intake edge and (b) the total pressure loss resulted from flow separation. Experiments regarding steady distortion may start from Dunham [40], who did extensive studies of total pressure distortions within an axial compressor. Considering the influence of a downstream fan, Pearson and McKenzie [116] further found that the profiles of both flow velocity and static pressure can be redistributed near the fan face. Parametric studies in this topic were done by Reid [126], who used a range of obstacles to generate steady-state total pressure distortion

and investigated the response of downstream axial compressors. The distortion in his research was altered by varying the area of the obstacle in both the circumferential and radial directions, with angles covering 22.5° to 360° and radial positions from tip to hub. Results showed that the distortion can be alleviated by a downstream compressor. The investigation of compressor tolerance suggested that long chord blades can lead to a greater attenuation of inlet distortion. More systematic studies about the influence of different scales of total pressure distortions can be found in SAE document APR1420 [175]. These indeed revealed a positive role of fan in dealing with intake distortions. However, most were induced by a total pressure loss and thus the investigations are limited to the steady influence with turbulence information missing.

Hence, we need to examine how the unsteady turbulent flow impacts the downstream fan performance. To do this, distortion generators with various shapes were designed, aiming at triggering unsteady turbulence towards fan or compressors. Lesser [85] proposed a rectangular frame to reproduce periodic disturbances induced by fuselage wakes. Wartzek [168] designed a delta wing for creating longitudinal vortices, and found that this type of distortion was minimal to the overall fan performance but could influence the flow at casing. Measurement campaigns from Hah et al. [64] also found that a rotor tends to be more tip-critical. Hence, most fan-intake distortion studies focused on the regions around blade tip. In Wartzek's [167] test rig, a bevelled beam was set in the upstream of rotor blade tip to create separations and unsteady turbulent flows. This was demonstrated to be able to imitate an intake with high incidence, and hence could be applied as a major configuration for the present study. In the test, both the circumferential and spanwise intake distortions were investigated, as well as the flow patterns of rotor-distortion interaction. Results showed that this type of distortion had massive influence on the inflow and compressor: it reduced the local massflow rate by 20% and deteriorated the total pressure ratio by around 3.5%. Further surveys of characterisation and quantification of the distortions were conducted by Bitter [16] using pressure-sensitive paint. This research provided distortion data in detail for the cases ranging from peak efficiency to near-stall points. Tests from Wartzek [168] also supplemented previous ones with axial and radial distortion at rotor and stator outlets, plotted by using total pressure probes.

The effectiveness of those distortion generators for imitating real engine environment has been analysed by Longley [95], Seddon [137] and Lesser [85]. They verified that intake distortions in actual flight context can be imitated by laboratory equipment. Although these experiments have provided very useful information for understanding

such interaction, numerical simulations are still necessary to provide abundant flow patterns and data and can also offer an insight of the flow phenomena.

The numerical studies of inlet distortion started from simplified models such as actuator disks [121, 26, 69] and parallel compressors [116, 103]. Most of these, however, are one or two dimensional simulations and cannot reflect realistic and complex flows around compressor blades. Recent three dimensional calculations were performed by steady or unsteady Reynolds-averaged Navier–Stokes ((U)RANS). Fidalgo [47] ran an unsteady, three-dimensional RANS simulation for the NASA Rotor 67 with steady total pressure distortion covering 120° at inlet. The test demonstrated the suitability of CFD application for fan-distortion interaction and revealed that the redistribution effect of a stage makes rotor tolerate a strong circumferential inlet distortion. Regarding the unsteady distortion, a typical source is from a high incidence angle. Relevant URANS simulations from Cao et al. [28] revealed that a fan can accelerate upstream flows and alleviate the distortion. The studies of the fan effect provided a potential mechanism of fan influence and hence further investigations need to be done on how a fan suppresses inlet distortion. In addition, Barthmes et al. [10] examined the distortion generated by a beam with URANS. The result showed that this type of distortion can be strongly influenced by an altered blade loading. Hence, the influence of fan loading also needs to be studied. These numerical studies indicate that unsteady simulation is an indispensable part for gaining an insight of fan-distortion interaction. Nevertheless, the limitation still exists: failing to provide high-order turbulence, the simulations cannot dive into the mechanisms of such interaction. Also, Longley and Greitzer [96] noted that the length scale of these inlet distortions can be as large as the mean radius. This does not only indicate that interactions among components can be much stronger, but also means that (U)RANS may suffer from severe limitations due to the “time averaged" features and poor resolution of turbulence [150]. Predictions may vary significantly when different RANS models are employed [150, 93, 90]. For these flows, eddy resolving simulations such as DNS, LES, hybrid RANS–LES, etc. are demonstrated to yield much more promising results [142, 92, 52].

2.2 Turbulence Simulations for Flow Separation

The previous section pointed out the potential failure of (U)RANS turbulence models. Hence, this section reviews different strategies of turbulence simulations, i.e. modelling and resolving for turbulent flows in the intake distortion under high incidence. Their suitability and costs will be examined and compared.

2.2.1 Defects of Turbulence Modelling Approach

Flow features in turbomachines, where there is periodic blade passing, were categorised by Hodson [68] and also illustrated by Gourdain [60] shown in Figure 2.1. A generic way

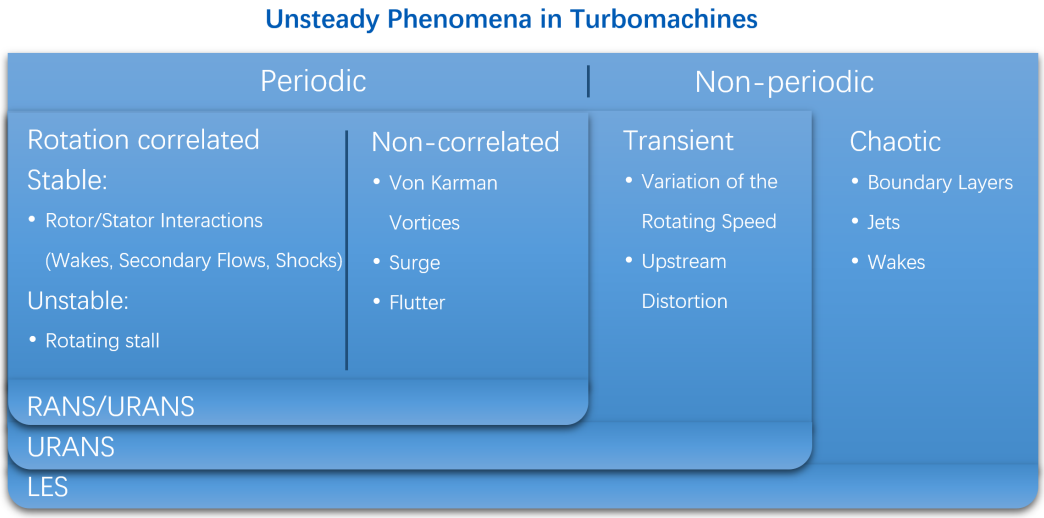

Fig. 2.1 Overview of the unsteady flow phenomena in turbomachinery, and corresponding turbulence treatments, originally from Gourdain [60]

to describe these flows is to use a triple decomposition, $\phi = \bar{\phi} + \phi'' + \phi'$ [149]. Hence the original instantaneous quantities are split into time averaged term $\bar{\phi}$, unsteadiness term ϕ'' and turbulent fluctuations ϕ'. Some typical flows that apply this decomposition are shown in Fig.2.2.

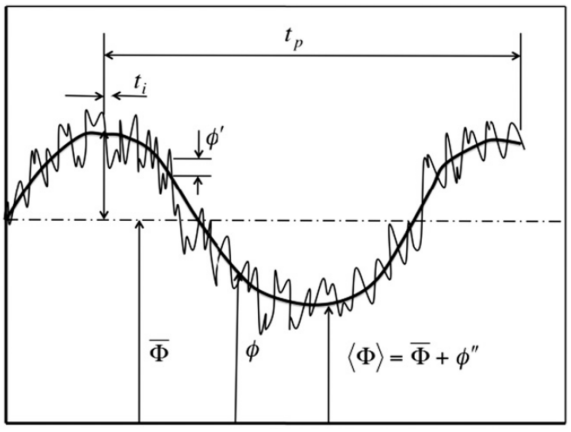

Fig. 2.2 Characteristic traces of periodic flows, from Tucker [149]

Among the flow phenomena noted by Gourdain, RANS is mainly used to solve steady flows or time-averaged periodic flows because it totally smears the unsteadiness;

by contrast, URANS can capture unsteady transient or periodic flow features. The two methods apply the Reynolds decomposition ($\langle\phi\rangle = \bar{\phi} + \phi''$) but introduce an additional fluctuating term, i.e. the Reynolds stress $\langle\phi\rangle = \langle-\rho\bar{u_i'u_j'}\rangle$. It is governed by the Reynolds stress equation

$$\begin{aligned}\frac{\partial\rho\overline{u_i'u_j'}}{\partial t} + \overline{U_k}\frac{\rho\partial\overline{u_i'u_j'}}{\partial x_k} = &-\left(\overline{u_i'\frac{\partial p'}{\partial x_j}} + \overline{u_j'\frac{\partial p'}{\partial x_i}}\right) - \frac{\partial\rho\overline{u_i'u_j'u_k'}}{\partial x_k} + \nu\frac{\partial^2\rho\overline{u_i'u_j'}}{\partial x_k^2} \\ &- \rho\overline{u_i'u_k'}\frac{\partial U_j}{\partial x_k} - \rho\overline{u_j'u_k'}\frac{\partial U_i}{\partial x_k} - 2\rho\nu\overline{\frac{\partial u_i'}{\partial x_k}\frac{\partial u_j'}{\partial x_k}}.\end{aligned} \tag{2.1}$$

The stress can be approximated by a range of turbulence models, such as the Mixing Length [122, 21], Spalart-Allmaras [142] and $k-\omega$ model [174]. Literature for the studies of periodic flows has demonstrated the performance of a range of turbulence modelling approaches. Johansson [74] used URANS with $k-\varepsilon$ model to investigate flows around and behind a triangular flameholder; Bosch [19] studied a square cylinder with high Reynolds number flow using a range of conventional and modified turbulence models. It showed that with proper grid resolution, these modelling approaches are able to approximately characterise vortices and predict both main velocities and fluctuations.

It should be noted that, however, such linear decomposition is based on the fact that the turbulence characteristic time t_i shown in Figure 2.2 is far smaller than the unsteady period t_p. For flows with intermittency, separation or boundary layer transition, t_i can be in the same order as t_p. Hence, this linear decomposition could be inaccurate for capturing unsteady features [49]. Although there are many modified turbulence models for improvement, most of them are validated by simple benchmark problems. Hence, their applications are limited to certain types of flows.

Specifically, there are several flow phenomena that need to be drawn attention to for the intake at high incidence: strong shear flows at the intake edge, substantial changes of streamline curvature, strong pressure gradients, large scale separations, etc., each of which can result in the failure of turbulence models. To investigate such failure, the exact form of the shear stress below is compared to the modelled one, with the assumption of 2D and incompressible flow for simplicity. The exact production term for shear stress in the Reynolds stress governing equation 2.1 is

$$\mathcal{P}_{ij} = -\rho\overline{u_i'u_k'}\frac{\partial U_j}{\partial x_k} - \rho\overline{u_j'u_k'}\frac{\partial U_i}{\partial x_k}. \tag{2.2}$$

Thus the shear stress $-\rho\overline{u'v'}$ is produced by

$$\begin{aligned}\mathcal{P}_{12} &= -\rho\overline{u'u'}\frac{\partial V}{\partial x} - \rho\overline{u'v'}\left(\frac{\partial U}{\partial x} + \frac{\partial V}{\partial y}\right) - \rho\overline{v'v'}\frac{\partial U}{\partial y} \\ &= -\rho\overline{u'u'}\frac{\partial V}{\partial x} - \rho\overline{v'v'}\frac{\partial U}{\partial y}.\end{aligned} \tag{2.3}$$

Note that for imcompressible flows, the final term considers the continuity equation

$$\frac{\partial U}{\partial x} + \frac{\partial V}{\partial y} = 0. \tag{2.4}$$

This shear stress is proportional to its rate of generation $\mathcal{P}_{12}$ multiplied by a turbulent time-scale k/ϵ, which gives:

$$-\rho\overline{u'v'} \propto \frac{k}{\epsilon}\left(\frac{\partial V}{\partial x} + \frac{\overline{v'v'}}{\overline{u'u'}}\frac{\partial U}{\partial y}\right) \tag{2.5}$$

On the other hand, with eddy viscosity models the shear stress is estimated by

$$-\rho\overline{u'v'} \propto \frac{k}{\epsilon}\left(\frac{\partial V}{\partial x} + \frac{\partial U}{\partial y}\right) \tag{2.6}$$

At the intake edge, the shear layer is created either by high incidence or crosswind and then the flow turns to axial direction. This results in a curved shear layer, meaning $\partial V/\partial x$ cannot be neglected. Also, there exists a strong vortex stretching process and hence highly anisotropic turbulence. Leschziner [84] noted that the normal stress is typically 25% in the flow normal direction of the one in streamline direction, i.e. $\overline{v'v'} \simeq 0.25\overline{u'u'}$. This indicates that the shear stress in Eq.2.6 obtained by the Boussinesq hypothesis is incorrect. Vaz et al. also [160] demonstrated that traditional isotropic RANS can fail to predict shear-layer predominant flows. Although this problem could be improved by adding a Richardson correction [128], predictions may still vary and sometimes give worse results [139].

When the reverse flow vertically hits the wall and reattaches, there is also an extensive strain problem at the stagnation point. At the stagnation point, the Reynolds stresses has the relation $\rho\overline{u'u'} \gg \rho\overline{v'v'} > 0$, due to the presence of the wall. Thus, the TKE production is

$$\mathcal{P} = -\rho\overline{u'u'}\frac{\partial U}{\partial x} - \rho\overline{v'v'}\frac{\partial V}{\partial y} = (\rho\overline{u'u'} - \rho\overline{v'v'})\frac{\partial V}{\partial y}, \tag{2.7}$$

where the continuity equation has been substituted. But on the other hand, the eddy viscosity assumption gives

$$\mathcal{P} = 2\mu_t \left(\frac{\partial U}{\partial x}\right)^2 + 2\mu_t \left(\frac{\partial V}{\partial y}\right)^2 \quad = 4\mu_t \left(\frac{\partial V}{\partial y}\right)^2 . \tag{2.8}$$

The flow decelerates towards the wall and thus $\partial V/\partial y < 0$. This leads to a negative $\mathcal{P}$ for Eq.2.7 but a positive value for Eq.2.8. Hence, the TKE production and turbulence can be overestimated by the model and this further results in the reduction of separation. The problem can be partially solved by the Yap [180] or Kato and Launder [76] corrections.

The problems above are mainly caused by turbulence anisotropy, but the non-equilibrium features can also lead to significant inaccuracy. This is because the shear flow at the intake edge also creates a recirculation area where strong adverse pressure gradients and flow separation exist. On one hand, the recirculating flows in this region can generate mild centrifugal body forces that interact with the turbulence and cause non-negligible energy backscatter [90]. This can be partially improved by adding terms to account for the impact of rotation on turbulence, which has been carried out by Bardina [9] and Wilcox [172]. Similarly, Liu et al. [90] applied a velocity helicity correction. On the other hand, such large scale separation bubbles also contain a range of multiscale eddies. For the large eddies, the size or the integral length scale is dependent on the relevant geometrical size. The turbulence at this scale contains most energy and is anisotropic and non-equilibrium. However, conventional eddy viscosity models apply equilibrium assumptions. This leads to an inaccurate prediction. There are indeed some non-equilibrium turbulence models [2, 115, 25] to help deal with this, but modelling all these multiscale eddies, from the integral down to the Kolmogorov length scale, by a single averaged eddy viscosity μ_t can also be a major failure for (U)RANS.

To understand this, Figure 2.3 shows a schematic depicting flow unsteadiness (the discrete bars) and turbulence (the curve) in the energy versus wave number ($E - k$) domain. Frame (a) represents a typical periodic flow that has a spectral gap (separated by a dashed line). The URANS is able to resolve some flows with periodic unsteadiness and simulate the turbulence with an appropriate model. An example is the Kármán vortices downstream a bluff body [74, 19], which can be resolved by some (U)RANS models. This is because the frequency of vortex shedding is low and dominant and thus the gap with turbulence is clear. For intake separation, however, the spectrum of turbulence ranges from a very low level to the Kolmogorov time scale. The frequency

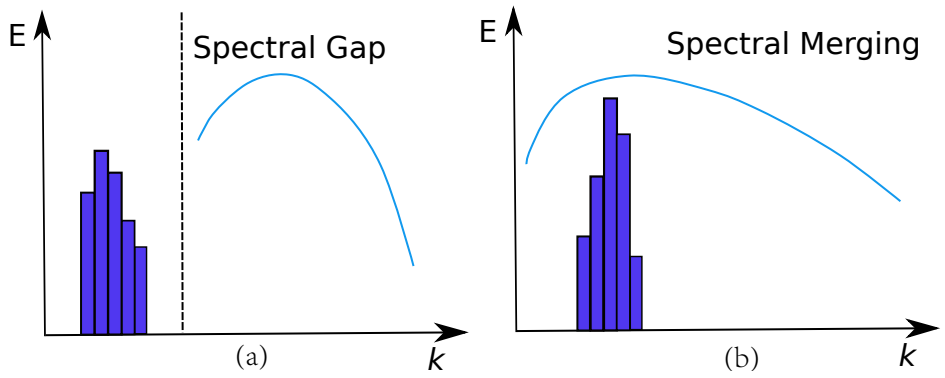

Fig. 2.3 Spectral distribution: (a) Spectral gap, required for (U)RANS (b) Spectral merging, need to be resolved, originally from Tucker [149]

of flow unsteadiness overlaps with that of the turbulence. This is shown by the curve in Frame (b), where the bars represents other flow unsteadiness, e.g. blade passing frequencies. From the point of view in the time domain, this also indicates that $t_p \sim t_i$ and the linear decomposition shown in Fig.2.2 does not apply. As a result, URANS models the turbulence from large scale to small scale turbulence, but at the same time, it also resolves the large scale turbulence, hence double accounting the result and leading to inaccuracy [149]. The investigation of backward cylinder separation, from Tucker and Liu [151], showed that the eddy viscosity can differ by more than two orders of magnitude when using various RANS models.

There are indeed many flow phenomena in aero-engines that do not have such spectral gaps. Tucker [149] reviewed a wide variety of flows for turbomachinery. The intake distortion shown in Figure 1.1 can have eddies of the scale of the intake radius. The interaction of these with downstream compressor can significantly affect the engine performance. Even if the flow is not too aggressive, Defoe [36] found that when the engine intake flow chokes, the boundary layer can dominate nearly 1/3 of the inlet. For eddies with such a big scale, relevant time scales are quantified as follows. The turbulence characteristic time t_i is $O(\delta/v_x)$, where δ is boundary layer thickness. Typically, the axial velocity in this formula $v_x = O(\Omega R)$, where Ω is engine rotating speed and R is the engine inlet radius. By contrast, the unsteady flow period t_p has the same order as the blade passing period $2\pi/(\Omega N)$, where N is the number of blades. Hence, the ratio can be estimated by

$$\frac{t_i}{t_p} \sim \frac{N\delta}{2\pi} = 0.15\frac{NR}{\pi}. \tag{2.9}$$

For example, in Wartzek's test, the height of distortion generator is 2/7 of intake radius, and the number of rotor blades is 16, giving $t_i/t_p \sim 0.76$. This means that the flow periodicity has the same order as turbulence and hence URANS may be inaccurate. Another example is the wakes passing through turbine blade passages, where wake frequencies could have the same order as that of turbulence [148], meaning URANS can not resolve it.

To summarise, the turbulence in the scenario of fan-intake interaction can be rather complicated and potential failures can result from turbulence anisotropy, non-equilibrium and multiscale eddy structures. This means that using a single conventional or even modified model may not tackle all the above problems. Hence, to simulate this type of flow, eddy resolving methods, such as LES and DNS are required.

2.2.2 Applications of Eddy Resolving Approach

In the hierarchy of turbulence modelling approach (Fig.1.5), the technique with the highest fidelity is DNS, which needs very fine mesh to resolve the turbulence from the largest to smallest. The result is the most accurate, but costs can be very high due to its enormous number of grid points and very small time steps. This technique is mainly applied to flows with low Reynolds numbers. For example, Freund [48] ran DNS to predict sound source in a jet flow at $R = 3600$. The mesh size is 25M which is acceptable. However, The Reynolds number for flows in a compressor can be as high as $10^6 \sim 10^7$. The wall spacing constraints can be very demanding (see Section 1.2) and thus costs can increase exponentially. This is infeasible for industrial use at the current stage [149].

By contrast, the LES can be more potentially useful. This method uses a spatial filtering with a decomposition consisting of large scale flow variables and subgrid scale quantities. Hence, it directly resolves largest eddies that contain the majority of total TKE and models the rest (smaller subgrid scale (SGS) turbulence). The concept of SGS models was first proposed by Smagorinsky [141], based on the assumption of a local production-destruction equilibrium for dissipative eddies.

There are a variety of models for approximating the interactions among SGS fluctuations. Smagorinsky's [141] is essentially an analogous eddy viscosity model. The objective of developing this model was to dissipate turbulence kinetic energy. The eddy viscosity was modelled by

$$\mu_t = \hat{\rho}(C_S\Delta)^2|\hat{S}|, \tag{2.10}$$

where C_S is the Smagorinsky constant, Δ is the filter width and the modulus of strain tensor

$$|\hat{S}| = \sqrt{\hat{S}_{ij}\hat{S}_{ij}}. \tag{2.11}$$

However, the constant C_S in this model sometimes can give excessive subgrid viscosity and hence it needs to be tuned to suit different flows. To overcome this drawback, the Dynamic Smagorinsky model [55] applies an adjusted C_s, but this can introduce instability [88]. Also, this type of Dynamic Smagorinsky still requires an expensive filtering procedure. Recently, the Smagorinsky model has been evolved into more complex reliable models, for example, the WALE [112] and σ [113] models . Hence, these techniques provide a proper way to simulate separated flows accurately. Details about the σ model can be found in Chapter 3.

A potential problem for these SGS models, however, is that the excessive numerical dissipation introduced by the models can severely affect the results. This is especially so when addressing complex, industrially challenging, high-Reynolds-number flows. In addition, for the separated flow in a channel, Frohlich et al. [50] observed that the flow can be very sensitive to various parameters of SGS models. The substantial numerical influence was also analytically investigated by Ghosal and Sandip [56] and then Chow and Moin [31] using a priori DNS. Their studies demonstrated that the LES with low order schemes may have difficulties in maintaining a numerical input that is lower than SGS model contributions. This means that the under-resolution can still be an insurmountable issue for the standard LES. In addition, the cost of model selection and the validation process for specific flows are also potentially high for ensuring accuracy. By contrast, other LES methods such as the Monotone Implicit LES (MILES) [17] and the Implicit LES can address this issue by relying on the characteristics of numerical methods. These methods replace the SGS model by numerical dissipation which can be kept at a minimal level via numerical schemes.

To understand this improvement, the numerical scheme of a 3D convection equation can be evaluated by the definition of *total variation*, which is

$$TV = \int_V \left|\frac{\partial \phi_i}{\partial x_i}\right| \mathrm{d}x. \tag{2.12}$$

Ideally, over a computational domain V the total variation TV should not increase with time. This means that

$$\int_V \left|\frac{\partial \phi_i^{n+1}}{\partial x_i}\right| \mathrm{d}x \leqslant \int_V \left|\frac{\partial \phi_i^{n}}{\partial x_i}\right| \mathrm{d}x, \tag{2.13}$$

where n is the time level. A method based on this property is thus called a Total Variation Diminishing (TVD) scheme. In this way, no new extrema within the domain is generated as time goes on, indicating that the scheme is monotonic or preserves monotonicity. Hence, with a TVD scheme, erroneous numerical oscillations can be prevented [65]. Practically, to enforce such monotonicity, various limiters were used to blend a low-order, high-resolution scheme with a high-order, low-resolution scheme. A typical one is a flux limiter for the Finite Volume Scheme, using which the total numerical flux is defined by

$$J = J^H - (1 - \varepsilon)(J^H - J^L), \tag{2.14}$$

where ε is the limiter, J^H is a high-order flux and J^L a low-order dissipative flux. The limiter ε needs to be tuned to reduce the dissipation. An investigation of this calibration was done by Roe [129]. Details of its application in the present research will be discussed in Chapter 3.

Based on the concept of monotonicity preserving , Boris [17] proposed the MILES scheme for simulating compressible, turbulent flows with high Re and complex geometry. The idea was "imitating the physics with the numerics, rather than cranking on a more formal mathematical approach" [62]. The MILES was directly derived from physical laws [18], does not add unphysical oscillations, and hence has demonstrated to behave as a SGS model for subgrid eddies [61]. With no SGS model explicitly presented in the LES equation, this method is essentially an ILES method [62], since numerical dissipation serves as a SGS model. A range of validation cases [51, 170, 176] have shown the success of the monotone-based or implicit LES methods. They provided accurate predictions for compressible flows with high Re, shocks, gradients, mixing, etc. Note that the use of models for the flow with shocks is specially compelling. The strain rate used in most SGS models tends to infinity around that region. Hence, MILES is ideal for flows with shocks. The application for jet flows in Eastwood's research [41] also showed that omitting SGS model could be a good way and thus the dissipation only comes from the numerical scheme.

2.2.3 Limitations of Eddy Resolving Approach

The computational costs of using eddy resolving method can be another important problem. To quantify the cost of eddy resolving methods, dimensionless wall distances are defined as

$$x^+ = \frac{xu_\tau}{\nu}, y^+ = \frac{yu_\tau}{\nu}, z^+ = \frac{zu_\tau}{\nu}, u_\tau = \sqrt{\frac{\tau}{\rho}} \tag{2.15}$$

Table 2.1 Near-wall grid requirements for DNS and LES, from Piomelli[120]

Grid Requirement	LES	DNS
Location of first grid point	$y^+ < 2$	$y^+ < 1$
Streamwise grid spacing	$x^+ \approx 50 - 100$	$x^+ \approx 15$
Spanwise grid spacing	$z^+ \approx 15 - 40$	$z^+ \approx 5$

Table 2.2 Computational resources and number of grids and iterations needed for flows at different Reynolds number, from Slotnick [140]

Re_c	N_{total}	$N_{iteration}$
1×10^6	1.1×10^6	4.6×10^7
1×10^7	1.1×10^7	1.5×10^8
1×10^8	9.4×10^7	4.6×10^8

where x, y, z are the coordinates in streamwise, wall-normal and spanwise directions, u_τ is the friction velocity at the nearest wall and can be calculated by the stress at the wall. Breuer [22] examined the requirement of a wall normal grid spacing and proposed $y^+ \approx 1$ for the first grid and five grid points in the viscous sub-layer (for both RANS and LES). Thus the spacing constraint y can be obtained. For the flows in the present study, the Reynolds number is $O(10^6)$, the reference length is 1.2m and hence the distance for the first grid could be as small as 4×10^{-6}m.

Outside the viscous sub-layer, what makes things more challenging is that the resolution of near wall region should also meet a high requirement: $y^+ \leqslant 100$ [22]. In this domain, turbulence plays a key role in the momentum transfer and the production of turbulent energy. Since these turbulent structures are very small, a very fine mesh is also required [38]. For wall resolved LES, $x^+ = 50 \sim 130$ in the streamwise direction, and $z^+ = 15 \sim 30$ in the spanwise direction [149]. By contrast, in these two directions, RANS only requires x^+ or $z^+ = 1000$, and only a fine resolution in wall-normal direction. Piomelli also provided the requirements for DNS, and they are compared in Table 2.1. Considering the temporal resolution for such fine mesh, this modelling approach can be significant time-consuming and expensive. For engine flows with a higher Reynolds number, the increase of the grid nodes and the required numerical calculations can be exponential, as shown in Table 2.2.

Large Eddy Simulation can be conducted on coarser meshes. Sagaut [131], however, pinpointed that coarser mesh may underpredict turbulence production and both the

Table 2.3 Near-wall grid resolution parameters and their impacts, from Sagaut[120]

Grid Resolution Parameters	Quality of mesh	Impact on Solution
$x^+ \leq 50, z^+ \leq 12$	High resolution	Good predictions of skin fiction
$x^+ \leq 100, z^+ \leq 30$	Medium resolution	Thicker and shorter streaks, error in skin friction
$x^+ \leq 100, z^+ \leq 30$	Poor resolution	Unrealistic streaks, larger error in skin friction prediction

Reynolds stress and skin friction can be underpredicted [45]. In addition to this, the log-law can be incorrectly simulated and excessive anisotropy may also appear near the wall [147]. Table 2.3 summarises the impact of LES with grids of different quality. These impacts can be exacerbated for flows at a high Reynolds number, which is often the case for compressors. Hence, high quality mesh is required for the studies of fan-intake interaction.

To reduce mesh size, a possible solution is to use hybrid RANS–LES [63], which applies a RANS layer for near wall turbulence and LES for the rest flow. A range of works [79, 42, 166, 135] have shown its performance in turbomachinery applications. By using this approach, the costs can be saved by multiple orders [102]. However, the RANS layer in this approach can lead to an inaccurate prediction of turbulence anisotropy in flow separation [134]. Also, as the compressor domain contains very complex blade passage geometries, the mesh generation process may cost a significant amount of effort. The domain is further split into static and rotational zones by rotor and stator. This means that the mixing plane can smear the information between the two zones and hence, in a time-averaged solution, the circumferential variation in the rotational zone will be lost. Therefore, an alternative method that can avoid these drawbacks while preserving numerical accuracy would represent significant progress for the industrial application of high-fidelity CFD.

2.3 Geometry Representation

2.3.1 Immersed Boundary Method

The Immersed Boundary Method (IBM) provides a potential way to replace conventional Direct Mesh Resolving (DMR) of geometry, hence improving the efficiency of flow simulations in aeroengines. The approach replaces the surfaces of complex geometric configurations by a distribution of "force". Hence, the boundaries of the components are immersed within the flow and the original complicated mesh can be substituted by a cylindrical polar mesh. Accordingly, the meshing process is greatly simplified.

Figure 2.4 illustrates the sketch of the IBM in Frame (a) and the Body Force Method (will be discussed in the next section) in Frame (b). When using the IBM, the force only exists in blade region. Since there is discontinuity for grids near blade surface, fine resolution is required and numerical stability issues may also occur for moving blades.

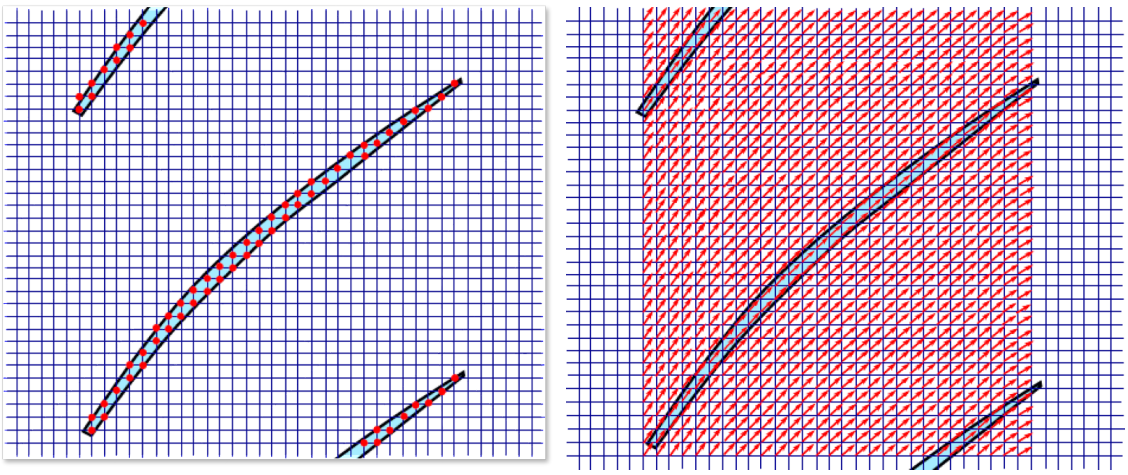

(a) Standard Immersed Boundary Method (b) Body Force Method, or eIBMg

Fig. 2.4 Force distribution by (a) standard IBM, (b) Body Force Method

The fundamental idea of replacing boundaries by forces was firstly introduced by Sirovich [138]. When solving linearised initial and boundary value problems, Sirovich converted the boundaries of the original computational domains into source terms (momentum and energy rates in his case) in the governing equations. Hence, the problem became an initial value problem in an unbounded domain. A similar approach was then applied by Vieceli [161], who provided clearer definitions of the "source terms." These are the boundary conditions for pressure and velocity, which forces flows to the desired

directions through iterations. This method was successfully applied to incompressible flows with arbitrary external boundaries. A rigorous demonstration of this method was provided by Peskin [119]. In his work the flow in the computational domain was solved using Eulerian variables and the structure in the fluid was denoted by Lagrangian variables. These two variables were linked by interaction equations, which contain the smooth approximation of a Dirac-delta function . Hence, by introducing these equations into the Navier–Stokes equations, the effect of the material boundaries and the replacing force are mathematically equivalent. This method was then successfully applied to the simulation of blood flow around an artificial heart valve [118].

When constructing the force term for IBM, different forcing strategies can be applied. According to Mittal and Iaccarino [107], these are categorised by the configuration of employing either continuous forcing or discrete forcing.

Continuous forcing , as its name implies, is continuously distributed in a computational domain via an a priori force model. The force has a certain value within rigid/elastic bodies and gradually approaches to zero in fluids. The force model takes various forms, one such commonly used model is feedback forcing. Xu [178] concluded that this feedback forcing can be regarded as a combination of proportional, integral, and derivative (PID) controllers. The PI controller was first applied by Goldstein et al. [57] to investigate flow–plate interactions. Other forms, such as the derivative controller [39], have a quicker effect but the result can be less accurate compared to integral controllers [132]. The drawback of this approach is its reliance of empirical coefficients in the force model, which, as noted by Goldstein, are dependent on the numerical scheme used and limited by the frequencies of the moving boundaries. Hence, this approach may be only suitable for static boundaries or steady simulations because it demands very small time steps in cases involving the unsteady simulation of moving bodies [57].

Discrete forcing, on the other hand, does not rely on any empirical coefficients and instead only imposes the force on the solid boundaries (strictly no imposed force within fluids, meaning that the distribution is discrete) by directly setting the conditions for flow variables. The setting can take the form of either fixing the flow primitives (direct forcing) or imposing the forces generated from the momentum and/or energy equations (indirectly containing the primitives). This method avoids the use of a priori force configurations and hence does not rely on any coefficients. However, the problem is that the IBM uses a Cartesian-like mesh so that the boundary surface is usually not aligned with the grid lines, which may result in stability problems. As a consequence, special treatments (e.g., interpolation) such as the ghost-cell [99, 46], cut-cell [32, 157],

influence matrix [73, 143] approaches, are required to satisfy either a rigid or soft no-slip wall boundary condition. These methods have been used for flow-induced vibrations [106], flapping foils [108, 70], oscillating cascades[71], and synthetic jets [158]. However, these are 2D cases and, when applied to 3D simulation, such treatments can be rather complicated and may lose their efficiency compared to the use of a body-fitted mesh. By contrast, indirect forcing does not impact the flow variables directly but uses forces created from the discretised conservative equations [14]. For three-dimensional compressible viscous flows, the conservative equations are the Navier–Stokes equations, which can be very complex and are not feasible to employ for analytical force models but may be used in numerical simulations. Mohd-Yosuf [109] proposed a force model derived from the momentum equation that captures the turning effect of the force generated by the difference between the actual flow velocity and the boundary velocity. This approach does not need any user-defined parameters and hence there are no stability requirements. However, this method needs to take into account the force distribution on actual boundaries. Hence, sufficiently accurate resolution of boundary layers at high Reynolds numbers may not be possible.

Applications of the IBM were investigated for a range of studies of 2D flows around a circular cylinder as well as 3D channel flows [11, 23, 57]. Simulations of turbulent flows around complex geometries were also carried out by Iaccarino and Verzicco [72], and Mittal and Iaccarino [107]. These studies included steady and unsteady flows at Reynolds numbers ranging from 10 to 10^6.

2.3.2 Body Force Models

When considering internal components of aero-engines, however, geometries are usually very complicated, especially the rotational blades. This means that resolving the boundary layers on the blade surfaces requires a very fine mesh and extensive computational resources. However, as discussed in previous section, the IBM uses an orthogonal mesh. This means that when simulating flows around an irregular body, the mesh configuration may not fit the fluid-solid boundaries. To improve the alignment as much as possible, it requires very fine mesh around the boundaries and thus does not show many mesh reduction compared to the DMR. To make things worse, if the "immersed boundary" is unsteady and moves over time, the computation requires very small time steps to get converged. Accordingly, a reduced-order form: Body Force Models (BFM) was proposed by Marble [100] shown in Frame (b), Fig.2.4. This method utilises the periodicity of blade passages in the compressor domain and smears blade boundaries meaning that flows within blade passages are averaged circumferentially. In this way,

the flow in blade region presents steady features albeit it is rotational. Essentially, this corresponds to an assumption of an infinite number of blades in a row of rotors or stators. Hence, the force of each blade is distributed in each computation cell within the blade region. Since no individual blade passage is resolved, the computational cost can be significantly reduced.

The BFM has various forms catering to specific aerodynamic problems. Each is derived from the momentum equation, energy equation, loss relation, perturbation relation, control theory, etc. Based on the flow physics and blade geometry, the inviscid body force model was firstly introduced by Marble [100] and was applied to force flows parallel to the blade camber line. More complex, three-dimensional blade geometries were then considered in Chima's [29] work for the study of compressor stability. Force models derived from momentum equations and loss relations can be found in both Gong's [58] and Gordon's research [57]. In Gong's model, the body force in the blade-normal direction was modelled using a steady correlation with the pressure rise. This was included in the unsteady simulation and stability analysis of compressors. By contrast, while investigating the effect of rotating tip clearance asymmetry in axial compressors, Gordon [59] employed a blade-parallel force derived from a relationship between the work of resistance and rotational total pressure loss. The BFM can be also expressed through a perturbation-response relation when studying flow stability in turbomachines. Sun et al. [144] and He et al. [67] developed models that take into account the effects of three-dimensional blade configuration (e.g., the swept airfoil design) on compressor instability. A similar model developed by Liu [89] also successfully predicted the stall margin when implemented with a casing liner.

The normal force in these models were constructed based on momentum equation, which essentially applies a derivative form. By contrast, force models with a PI controller would perhaps be easier for steady simulations [27, 169] or unsteady simulations with circumferential averaging conditions [97]. For example, in aerodynamically coupled systems, Watson et al. [169] applied this method to the investigation of the inlet distortion of a compressor using RANS, which showed features consistent with those observed in experiments [168].

Considering the loss effects in unsteady simulations, a viscous body force model proposed by Xu [177] has demonstrated a good performance for characterising the loss of the flow passing through blade passages in a high-pressure turbine. The model significantly reduced the computing time by two orders of magnitude compared to a mesh-resolving case. A similar modelling approach for the parallel force can be used to generate wakes downstream a rotor or stator. Loiodice et al. [94] developed a model

to provide a wake zone using a square wave, which distributes the parallel force in the blade region. In the model, the coefficients for imitating interblade and wake turbulence length scales need to be calibrated. The idea for distributing forces can offer a potential way to model fan geometry.

The BFM indeed performs well when the variations in the circumferential direction can be ignored. When considering full 3D simulations, however, the approach can lose some important information due to the circumferentially smeared geometry or the assumption of an infinite number of blades. Although a number of researchers [35, 36] have proposed body force perturbations to generate blade-to-blade variations, the model still relies on the prerequisite data of a single rotor passage from RANS and then a subsequent reconstruction process. Hence, to reflect more realistic flow physics in three dimensions whilst maintaining a reduced computational cost, a method that can model the rotor or stator with actual finite blades, and hence provide flow physics in blade passages is also desired.

2.4 Concluding Remarks

This chapter reviewed experiments and numerical simulations for fan-intake interaction and found that most simulations are based on conventional turbulence models and still cannot reveal the mechanisms of fan influence. These models may also suffer from severe limitations due to the coupling of highly separated flows and turbulence, i.e. the lack of spectral gap. This was followed by reasoning their potential inaccuracy. Various turbulence models were reviewed considering the scenario of fan-intake interaction. It was found that there are many potential reasons that leads to the failure of eddy modelling approaches. This includes the turbulence anisotropy, non-equilibrium and multiscale eddy structures. Consequently, the eddy resolving methods are required to tackle the problem. However, considering the extremely complex computational domains in aero-engine simulations, the costs of using eddy resolving methods can be much higher. Hence, these methods are still infeasible for industrial applications. According to the reviews of relevant applications based on the Immersed Boundary Method and Body Force Models, this can be potentially reduced by combining high-fidelity turbulence simulations and low-order geometry models. Also, a more realistic force model needs to be developed to simulate the effects of individual blades. These methods could be integrated into a mixed-fidelity method and hence the simulation for fan-intake interaction with high fidelity can be possible. With such a method, the mechanism of fan influence on unsteady distortion from an intake can be revealed,

the fan design with a range of parameters can be explored more accurately, and the applicability of RANS models can be also investigated by comparing with LES.

Chapter 3

Methodology

The study of mixed-fidelity modelling is mainly based on HYDRA, a set of Rolls-Royce's in-house codes [34, 80]. They were used for steady RANS simulations originally and developed for URANS and LES. The present research implemented the modules for mixed-fidelity modelling with IBM and eIBM. This chapter introduces the technical details and explains how they are implemented in HYDRA. This starts from the introduction of the major contribution, geometry modelling, followed by turbulence modelling techniques. The final section will describe how these two hierarchical approaches are implemented in the equation solver.

3.1 Geometry Modelling

The major contribution of the thesis is developing and implementing a range of geometry modelling approaches via the source terms in the NS equations. This section discusses technical details of the force construction and distribution, as well as their capability for different CFD schemes.

3.1.1 Standard IBM

A commonly used form for the IBM is proportional-integral feedback forcing,

$$\begin{aligned} \boldsymbol{f}(\boldsymbol{x},t) &= \alpha \int_0^t \Delta \boldsymbol{u} dt + \beta \Delta \boldsymbol{u}, \\ \Delta \boldsymbol{u} &= \boldsymbol{u}(\boldsymbol{x}_s,t) - \boldsymbol{u}_s(\boldsymbol{x}_s,t). \end{aligned} \tag{3.1}$$

The subscript s represents the solid boundary, and t is the pseudo time within each real time step. This can be applied to unsteady CFD simulations with implicit time

schemes or to steady simulations. The coefficients α and β are empirical constants that need to be calibrated by a benchmark. The term $\Delta \boldsymbol{u}$ represents the velocity difference between the local flow velocity and the target velocity. This 'error' $\Delta \boldsymbol{u}$ minimizes the forces. Once the solution converges to the target velocity distribution, the body force approaches to zero and the solution is independent of α and β.

For unsteady calculations, the time step is also bounded by the following inequality proposed by Goldstein [57] to ensure numerical stability:

$$\Delta t < \frac{-\beta - \sqrt{\beta^2 - 2\alpha k}}{\alpha}, \tag{3.2}$$

where k is a problem-dependent constant of order 1. According to this, the coefficients should, however, be carefully selected in order to speed up convergence while maintaining stability. α and β are in fact associated with two important parameters: the frequency of the integral part of the feedback forcing, $\sqrt{|\alpha|}/2\pi$, and the damping factor of the proportional part of the feedback forcing, $-2\sqrt{|\alpha|}/\beta$. Hence, α must be large enough to ensure that the frequency, $\sqrt{|\alpha|}/2\pi$, is much higher than any other frequencies within the flow [44]. This suggests that the feedback force should evolve as rapidly as possible and direct the flow to the target velocity distribution. Saiki [132] demonstrated the basic principles for the selection of these coefficients in the investigation of flows around a cylinder. For fixed bodies in compressors, Waston et al.[169] verified that the values of α and β do not influence the flow field when "$\Delta \boldsymbol{u}$" has converged to zero. Both the final flow field and the convergence speed were substantially the same for the range of values (0.1-10) of α and β investigated in his study. This force model can be used for static components such as distortion generator [97], probes [155], the bypass geometry [153], etc.

3.1.2 Euler IBM

Aero-engines contain a large number of rotational or static blades with periodic features and the Reynolds number of flows around these geometries can be very high. Consequently, the grid resolution using IBM can still be very demanding. Otherwise, a coarse Cartesian-like mesh with an IBM blade may generate substantial non-physical separations and the computation can become unstable. However, if the mesh is relatively fine, the method may lose its advantage compared to the DMR. To tackle this problem, the Euler IBM is proposed. It is essentially a "degraded" IBM method, by which fan blades can be modelled using an inviscid force combined with a loss

model. The word "Euler" is introduced because intrinsically the inviscid boundary condition on the blade is applied. The blade force is decomposed into a normal force and a parallel force. The former directs flows parallel to the blade camber line, whilst the latter decelerates flows via loss effects. The eIBM has two forms, global and local distributions for force terms, i.e. the eIBM with global force (eIBMg) and the one with local force (eIBMl). In the following sections, we first discuss the construction of the force by normal and parallel forcing and then the distribution of the force via two different ways, globally and locally.

Normal Forcing

When building normal forces and implementing it in a CFD solver, we should consider the applicability for implicit or explicit numerical schemes. This is an important issue for the construction of normal force and different forcing tools are examined by their ways of configuration.

Similar to the IBM, one way to build the normal force is to use PI feedback forcing, but only in the normal direction.

$$f_n(\boldsymbol{x}, t) = \alpha \int_0^t \Delta u_n dt + \beta \Delta u_n \tag{3.3}$$

For the eIBMg, forces are circumferentially averaged. When a fan rotates there is still no actual moving boundaries and the flow frequency for the blade region is theoretically infinitesimal. Hence, the flow frequency is much lower than the frequency of the integral part $\sqrt{|\alpha|}/2\pi$, meaning that there is no computational instability problem. However, when using the eIBMl, the forces are localised and there exists the rotational blade boundaries. With an implicit time scheme, the time t still works partially as a pseudo time and the physical time step can be set very large in order to meet the requirement $\sqrt{|\alpha|}/2\pi \gg 1/(\Delta t)$. However, for an explicit time scheme, a small time step Δt is required to keep the error in the result bounded or ensure the numerical stability. This means that flow frequencies determined by $1/\Delta t$ can be of the same order as or even higher than $\sqrt{|\alpha|}/2\pi$, meaning the computation for forcing flows may easily diverge.

To avoid this issue, cases employing explicit time schemes need to apply derivative or difference controllers which can provide an immediate change [39]. Mohd-Yusof [109] proposed an indirect force model derived from the derivative form of the Navier–Stokes momentum equation without any empirical coefficients. Hence, we apply this force model to replace the boundaries of the rotor and stator blades. The blade forces are decomposed in the normal and parallel directions. The normal force $\boldsymbol{f}_n$ can be obtained

via the momentum Navier–Stokes equations:

$$\rho\frac{\partial \boldsymbol{u}}{\partial t} + \rho\nabla(\boldsymbol{u}\boldsymbol{u}) = -\nabla p + \nu_t\nabla^2\boldsymbol{u} + \boldsymbol{f}, \tag{3.4}$$

where f is the body force. If this is discretised in time, in blade normal direction, we have

$$\rho\frac{u_n^{l+1} - u_n^l}{\Delta t} = RHS^l + f_n^{l+1/2}, \tag{3.5}$$

where l is the time level, $1/2$ denotes the process for the force configuration, and RHS^l contains convective and viscous terms and the pressure gradient. When flows fit a given blade angle, then ideally $u_n^{l+1} = V_n^{l+1}$ within the immersed blade region. The velocity is $V_n^{l+1} = \boldsymbol{r} \times \boldsymbol{\Omega} \cdot \boldsymbol{n}_0$ for the rotational rotor blades and zero for the stator. Hence, the normal force can be obtained by

$$f_n^{l+1/2} = -RHS^l + \rho\frac{V_n^{l+1} - u_n^l}{\Delta t}. \tag{3.6}$$

This force then turns the flow towards the desired angle directly without any dynamical process, as required by the PI controller. At every time step, this is determined only by the fan blade geometries regardless of the flow frequencies and constants that feedback forcing relies on. Consequently, the time step can be increased and the CPU time can be significantly reduced. In this thesis, Eq.3.3 was used to model the static components and Eq.3.6 was used to model rotational blades.

Parallel Forcing

The parallel force can be modelled using the force-velocity relation introduced by Xu [177], representing an loss effect. This model characterizes the loss of flows passing through the blade passages. In Xu's research, this simple relation performed well for the investigation of distortion transfer across blade rows in a high-pressure turbine. It significantly reduced the computing time, by two orders of magnitude compared to the mesh-resolving case. In a study of distortion for compressors, Cao et al. [27] and Watson et al. [169] developed a loss model that considers the blockage and wall viscosity near the casing and hub. These studies demonstrated a good consistency with experiments [168, 167]. In Watson's research, this force is modelled as,

$$f_p = -(4s^2 + 1)k\rho\boldsymbol{u}_{rel}^2, \tag{3.7}$$

where s is the fraction of span and the related term $4s^2 + 1$ indicates higher losses near blade hub and tip due to wall effects. The coefficient k is a constant to be calibrated by the steady performance data p_t and $\dot{m}$ from experiments or DMR cases. It was kept the same for all the operating points in the thesis, but can be further improved as a function of operation point. Noted that the velocity is not strictly zero within a blade, but slowed down by the parallel force.

Although the use of a loss model cannot provide very much detail within the blade passages, it is still able to provide a relatively accurate "boundary" for both upstream and downstream flows. For the study of the region between fan and intake, this method can provide an economic solution while preserving accuracy.

Force distribution

The eIBMg just distributes both normal and parallel forces uniformly in the circumferential direction (Fig.2.4), whereas the distribution of eIBMl forces is an essential part. For both methods, the velocity in blade region is not strictly zero but dynamically decelerated by such a parallel force. The eIBMl is expected to be able to model rotor or stator with actual finite blades, and to simulate flows within blade passages and the corresponding wave propagation. In this way, the method

1. avoids a conventional mixing plane so that the interaction between static and rotational components cannot be smeared;

2. simplifies mesh generation process significantly, which makes virtual prototype design cost-effective;

3. makes high-fidelity simulations possible for multiscale turbulence within certain flow regions.

The sketch of eIBMl is illustrated in Fig.3.1. Note that the velocity is represented by vectors not points for the IBM in Frame (a), Fig.2.4. To understand this distributing process, the forces obtained from Eq.3.3 and 3.7 can be regarded as a "force density $\boldsymbol{F}_d$" defined in Peskin's [119] theory. As a consequence, the blade can enforce the flow through the Dirac function δ as,

$$\boldsymbol{f}(\boldsymbol{x}, t) = \int \boldsymbol{F}_d \delta \left(\boldsymbol{x} - \boldsymbol{X}(\boldsymbol{x}_0, t)\right) \mathrm{d}\boldsymbol{x}_0, \tag{3.8}$$

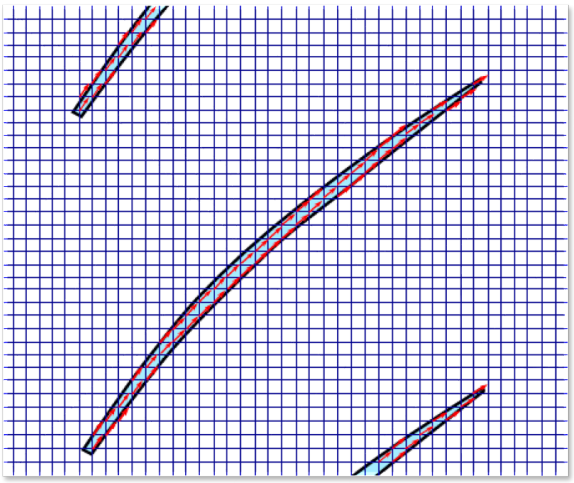

Fig. 3.1 Euler IBM with local force

where $\boldsymbol{X}(\boldsymbol{x}_0, t)$ is the configuration of the blade immersed in the flow. The Dirac function is defined as

$$\delta\left(\boldsymbol{x} - \boldsymbol{X}(\boldsymbol{x}_0, t)\right) = \begin{cases} \infty, & \boldsymbol{x} = \boldsymbol{X}(\boldsymbol{x}_0, t). \\ 0, & \boldsymbol{x} \neq \boldsymbol{X}(\boldsymbol{x}_0, t). \end{cases} \tag{3.9}$$

and

$$\int_V \delta\left(\boldsymbol{x} - \boldsymbol{X}(\boldsymbol{x}_0, t)\right) \mathrm{d}\boldsymbol{x} = 1, \tag{3.10}$$

where 'V' denotes the entire computational region. In practice, a range of analytical distribution functions have been proposed to approximate the Dirac function. Potential solutions include the Gaussian function [57], bilinear interpolation [132], the Boundary Data Immersion Method that considers distance to boundaries [171, 98], etc. The present case has periodic features for fan blades in the circumferential direction. Accordingly, a square wave function is chosen and the blade force can be configured using a distribution function

$$\mathcal{F}(\boldsymbol{x}, t) = H(R_b - r) \sum_{n=0}^{\infty} a_n cos(\theta + \theta_0 + \Omega t), \tag{3.11}$$

where

$$a_n = \frac{2}{n\pi} sin\left(\frac{nN\delta_b}{2r}\right). \tag{3.12}$$

The Heaviside step function $H(R_b - r)$ considers the rotor blade clearance via the definition

$$H(R_b - r) = \begin{cases} 1, & r < R_b. \\ 0, & r \geqslant R_b. \end{cases} \tag{3.13}$$

where r is radial coordinate and R_b is the blade length in spanwise direction.

For numerical simulations, increasing the number of the series a_n may lead to the Gibbs phenomenon [6, 77, 86] on the solid boundaries. Hence, limitations on both the upper ($\max\{\mathcal{F}\} = 1$) and lower bounds ($\min\{\mathcal{F}\} = 0$) are set to avoid this issue. One may argue that the jump of a value on the boundaries may lead to computational instability, but in fact, the normal force f_n only fixes the direction of the blade force, whereas the parallel force f_p or the loss model smooths the blade boundaries. This means that the initial velocity within the blades is not strictly zero or a constant of blade velocity, but gradually dissipates with a dynamic process.

In the triangular series, θ is the circumferential direction in cylindrical coordinates, θ_0 is the circumferential location of blade camber line, N is the number of fan blades, Ω is the rotational speed of fan, and δ_b is the thickness of a blade. It should be noted that θ_0 and δ_b are also functions of space and are determined by the blade location and shape respectively, meaning that the blade profile is included. Thus, the blade forces can be expressed as

$$\boldsymbol{f}_b(\boldsymbol{x}, t) = (f_n \boldsymbol{n_0} + f_p \boldsymbol{p_0}) \mathcal{F}(\boldsymbol{x}, t), \tag{3.14}$$

where $\boldsymbol{n_0}$ and $\boldsymbol{p_0}$ denote the unit vectors in the directions normal and parallel to blade surfaces. Essentially, this form of force is distributed within the blade region but the geometry is actually smeared according to the blade camber line. This means that, on the blade surface, the flow may not follow the curves on either the pressure surface or the suction surface, but the camber line instead. In addition, this approximation may result in some level of deviation for the transition or viscosity-induced separation near the blade trailing edge. This is expected to be improved by adding deviation models at the next stage. Since the aim of this research is to generate suitable boundary conditions for the upstream flows, its disadvantages can be neglected.

3.2 Turbulence Modelling

This section starts from the standard NS equation and then describes the technique details for RANS/URANS with both Spalart-Allmaras and $k-\omega$ and LES with σ model. These models were used in the present simulations.

3.2.1 Navier–Stokes Equations

The RANS/URANS and LES equations are based on the Navier–Stokes Equations. Derived from the conservation laws of mass, momentum and energy, the equations are

$$\begin{aligned} \frac{\partial \rho}{\partial t} + \frac{\partial \rho u_i}{\partial x_i} &= 0, \\ \frac{\partial \rho u_i}{\partial t} + \frac{\partial \rho u_i u_j}{\partial x_j} &= -\frac{\partial p}{\partial x_i} + \frac{\partial \sigma_{ij}}{\partial x_j}, \\ \frac{\partial \rho e}{\partial t} + \frac{\partial (\rho e + p) u_j}{\partial x_j} &= -\frac{\partial q_j}{\partial x_i} + \frac{\partial u_i \sigma_{ij}}{\partial x_j}. \end{aligned} \tag{3.15}$$

In the momentum equation, the shear stress tensor is given by

$$\sigma_{ij} = 2\mu S_{ij}, \tag{3.16}$$

where μ is dynamic viscosity computed using the Sutherland's Law

$$\frac{\mu}{\mu_{ref}} = \left(\frac{T}{T_{ref}}\right)^{1.5} \frac{T_{ref} + S}{T + S}, \tag{3.17}$$

where μ_{ref}, T_{ref} and S are the reference viscosity, reference temperature and Sutherland coefficient respectively. Their values can be found in Ref.[145]. The strain tensor S_{ij} is defined as

$$S_{ij} = \frac{1}{2}\left(\frac{\partial u_i}{\partial x_j} + \frac{\partial u_j}{\partial x_i}\right) - \frac{1}{3}\frac{\partial u_k}{\partial x_k}\delta_{ij}, \tag{3.18}$$

where δ_{ij} is the Kronecker delta ($\delta_{ij} = 0$, if $i \neq j$, and 1, if $i = j$). The internal energy e can be expressed as

$$e = \frac{1}{\gamma - 1}\frac{p}{\rho} + \frac{1}{2}u_i u_i. \tag{3.19}$$

The equation is finally closed with the heat flux q_j estimated by the Fourier's law,

$$q_j \equiv -\lambda \frac{\partial T}{\partial x_i}. \tag{3.20}$$

3.2.2 RANS

Governing Equations

At the bottom of the hierarchical turbulence modelling (Fig.1.5), RANS has demonstrated to be the fastest and widely used for industry application. It applies a time-averaged decomposition to flow variables and a range of turbulence models to approximate fluctuation terms. The decomposition of the instantaneous terms is

$$\begin{aligned} \phi(x,t) &\equiv \bar{\phi}(x) + \phi'(x,t), \\ \bar{\phi}(x) &\equiv \frac{1}{T}\int_T \phi(x,t)\mathrm{d}t, \end{aligned} \tag{3.21}$$

where the bar denotes the Reynolds averaging. Theoretically, it should be noted that Favre averaging [15] can be more accurate for compressible flows and this averaging process applies the decomposition

$$\begin{aligned} \phi(x,t) &\equiv \tilde{\phi}(x,t) + \phi''(x,t), \\ \tilde{\phi}(x) &\equiv \frac{\overline{\rho\phi}}{\bar{\rho}} = \frac{\int_T \rho(t)\phi(t)\mathrm{d}t}{\int_T \rho(t)\mathrm{d}t}, \end{aligned} \tag{3.22}$$

where ϕ'' is the fluctuation using a density weighted average. However, turbulence usually does not cause significant fluctuations in density, except for highly compressible or hypersonic flows. Hence, in practice, considering most cases here are subsonic or transonic, Reynolds averaging can still be used. When substituted the Reynolds decomposition into the NS equation, it yields

$$\begin{aligned} \frac{\partial \bar{\rho}\bar{u}_i}{\partial x} &= 0, \\ \frac{\partial \bar{\rho}\bar{u}_i\bar{u}_j}{\partial x_j} &= \frac{\partial}{\partial x_j}\left(-\bar{p}\delta_{ij} + \bar{\sigma}_{ij} + \tau_{ij}^R\right), \\ \frac{\partial(\bar{\rho}\bar{e} + \bar{p})\bar{u}_j}{\partial x_j} &= \frac{\partial}{\partial x_j}\Big[\left(\bar{\sigma}_{ij} + \tau_{ij}^R\right)\bar{u}_i + \overline{\sigma_{ij}u_i'} - \frac{1}{2}\overline{\rho u_i' u_i' u_j'} \\ &\quad -\bar{q}_j + c_p\overline{\rho u_j' T'}\Big], \end{aligned} \tag{3.23}$$

where the specific heat capacity at constant pressure and time-averaged heat flux are

$$\begin{aligned} c_p &= \frac{\gamma}{\gamma - 1}, \\ \bar{q}_j &= -\lambda\overline{\frac{\partial T}{\partial x_j}} \approx -\frac{c_p\mu}{Pr}\frac{\partial \bar{T}}{\partial x_j}, \end{aligned} \tag{3.24}$$

and Pr is the Prandtl number (around 0.72 for air). In the momentum equation, the viscous stress tensor $\bar{\sigma}_{ij}$ is

$$\bar{\sigma}_{ij} \approx 2\mu \left(\bar{S}_{ij} - \frac{1}{3} \frac{\partial \bar{u}_k}{\partial x_k} \delta_{ij} \right). \tag{3.25}$$

The Reynolds stress term $\tau_{ij}^R \equiv -\overline{\rho u_i' u_j'}$, introduced by time averaging, is approximated by the eddy viscosity model according to the Boussinesq Hypothesis [152]. That is,

$$\tau_{ij}^R = 2\mu_t \left(\bar{S}_{ij} - \frac{1}{3} \frac{\partial \bar{u}_k}{\partial x_k} \delta_{ij} \right) - \frac{2}{3} \rho k \sigma_{ij}, \tag{3.26}$$

where μ_t is the eddy viscosity, $\bar{S}_{ij}$ is the mean rate of strain tensor. The turbulence kinetic energy (TKE) $k = \frac{1}{2}\overline{u_i' u_i'}$ is sometimes ignored for non-supersonic flows, resulting in a similar form to σ_{ij}. Hence, we combine the two stresses and use

$$\bar{\tau}_{ij} = 2(\mu + \mu_t) \left(\bar{S}_{ij} - \frac{1}{3} \frac{\partial \bar{u}_k}{\partial x_k} \delta_{ij} \right). \tag{3.27}$$

In the energy equation, the rest terms are modelled as follows.

$$\overline{\sigma_{ij} u_i'} - \frac{1}{2} \overline{\rho u_i' u_i' u_j'} \approx \left(\mu + \frac{\mu_t}{\sigma_k} \right) \frac{\partial k}{\partial x_j}, \tag{3.28}$$

where σ_k is a coefficient associated with the modelling equation for k. This term, however, is sometimes neglected. The term associated with the temperature fluctuation is modelled by a Reynolds analogy,

$$\overline{\rho u_j' T'} \approx -\frac{\mu_t}{Pr_t} \frac{\partial \bar{T}}{\partial x_j}. \tag{3.29}$$

This is called turbulent heat flux, and Pr_t is a turbulent Prandtl number taken to be constant (around 0.9 for air).

The only unknown quantity left is the eddy viscosity μ_t. There are many models to explicitly approximate it, including the Baldwin-Lomax [7], the Spalart-Allmaras [142], various two equation models [75, 174], non-linear approaches [54] and the Reynolds stress model [30]. The complexity of these model, however, as Batten [12] noted, as well as numerical brittleness and resource requirements, grows in the listed order, and increasingly restricts to specific applications. Hence, the industry usually adopts one or two equation models considering their efficiency.

Spalart-Allmaras model

In the present research the Spalart-Allmaras (SA) model [142] and Menter $k-\omega$ Shear Stress Transport (SST) model [105] are applied and compared against LES. The basic idea of the SA model is to solve a PDE regarding a viscosity like variable $\tilde{\nu}$ (the kinematic viscosity $\nu_t = \tilde{\nu} f_{v1}$, modified by coefficients f_{v1}), which is

$$\frac{\partial \tilde{\nu}}{\partial t} + \bar{u}_j \frac{\partial \tilde{\nu}}{\partial x_j} = \mathcal{P}(\tilde{\nu}) + \mathcal{D}i(\tilde{\nu}) - \mathcal{D}e(\tilde{\nu}) + \mathcal{T}, \tag{3.30}$$

where $\mathcal{P}(\tilde{\nu}), \mathcal{D}i(\tilde{\nu}), \mathcal{D}e(\tilde{\nu}), \mathcal{T}(\tilde{\nu})$ are production, diffusion, destruction, and trip contribution terms. Their definitions are

$$\begin{aligned} \mathcal{P}(\tilde{\nu}) &= c_{b1}\tilde{S}\tilde{\nu}, \\ \mathcal{D}i(\tilde{\nu}) &= \frac{1}{\sigma}\{\nabla \cdot [(\nu + \tilde{\nu})\nabla\tilde{\nu}] + c_{b2}(\nabla\tilde{\nu})^2\}, \\ \mathcal{D}e(\tilde{\nu}) &= \left(c_{w1} f_w - \frac{c_{b1}}{\kappa^2 f_{t2}}\right)\left(\frac{\tilde{\nu}}{d}\right)^2, \\ \mathcal{T} &= f_{t1}(\Delta u)^2. \end{aligned} \tag{3.31}$$

The trip term $\mathcal{T}$ is to trigger transition at a specified location. However, it is usually set to zero in keeping with many implementations. The auxiliary variables in these terms are

$$\begin{aligned} & f_{v1} = \frac{\chi^3}{\chi^3 + c_{v1}^3}, \chi = \frac{\tilde{\nu}}{\nu}, f_{v2} = 1 - \frac{\chi}{1 + \chi f_{v1}}, \\ & f_w = g\left(\frac{1 + C_{w3}^6}{g^6 + C_{w3}^6}\right)^{1/6}, g = r + C_{w2}(r^6 - r), r = \frac{\tilde{\nu}}{\tilde{S}\kappa^2 d^2}, \\ & \tilde{S} = S + \frac{\tilde{\nu}}{\kappa^2 d^2} f_{v2}, S = \sqrt{2\Omega_{ij}\Omega_{ij}}, \Omega_{ij} = \frac{1}{2}\left(\frac{\partial u_i}{\partial x_j} - \frac{\partial u_j}{\partial x_i}\right), \end{aligned} \tag{3.32}$$

where ν is molecular kinetic viscosity and d is the distance to the nearest wall. The constants can be found in Ref.[142]. After solving the equation 3.30, the eddy viscosity can be obtained by

$$\mu_t = \rho\tilde{\nu} f_{v1}. \tag{3.33}$$

Menter k-omega SST model

The Menter $k-\omega$ SST model is based on the standard $k-\omega$ model [173], which applies two PDEs to calculate the turbulence kinetic energy k and specific rate of dissipation

ω. The latter is defined by

$$\omega = \frac{\epsilon}{k\beta^*}, \epsilon = \omega k \tag{3.34}$$

where ϵ is the turbulence dissipation, β^* is a model constant set to 0.09, and the eddy viscosity is computed by

$$\mu_t = \frac{\rho k}{\omega}, \tag{3.35}$$

The equation for k and ω are the same, governed by the law of conservation:

$$\frac{\partial(\rho\phi)}{\partial t} + \frac{\partial(\rho u_j \phi)}{\partial x_j} = \underbrace{\tau_{ij}\frac{\partial u_i}{\partial x_j}}_{\text{Production}} - \underbrace{\beta^*\rho\omega\phi}_{\text{Dissipation}} + \underbrace{\frac{\partial}{\partial x_j}\left[(\mu + \sigma^*\mu_t)\frac{\partial \phi}{\partial x_j}\right]}_{\text{Re-distribution}}, \tag{3.36}$$

By replacing ϕ with k (or ω) and making corresponding changes to the production term, we can obtain the two equations for $k-\omega$ model. Details of the coefficients can be found in Wilcox's paper [173].

One of the defects of standard $k-\omega$ model is the sensitivity to freestream turbulence, which can be improved by $k-\epsilon$ model. It has a similar form to Eq.3.36 with ω replaced by the dissipation ϵ. The $k-\epsilon$ model is less sensitive to initial conditions and freestream but can be inaccurate for wall effects. Hence, Menter [105] developed a SST model that blends both models and uses the wall distance as a switch. It retains the accuracy for near wall region whilst keeping the computation robust. The new model was created by using a linear combination,

$$\phi = F\phi_1 + (1-F)\phi_2, \tag{3.37}$$

where ϕ_1 represents the terms in the equations of $k-\omega$ model and ϕ_2 represents that of transformed $k-\epsilon$ model where the dissipation ϵ was substituted by the specific rate of dissipation ω for consistence. The turbulent eddy viscosity is computed by

$$\mu_t = \frac{\rho a_1 k}{\max(a_1\omega, \Omega F)}. \tag{3.38}$$

where the vorticity magnitude

$$\Omega = \sqrt{2W_{ij}W_{ij}}, W_{ij} = \frac{1}{2}\left(\frac{\partial u_i}{\partial x_j} - \frac{\partial u_j}{\partial x_i}\right). \tag{3.39}$$

The constants a_1 and blending function F can be referred to Menter's paper [105].

It should be noted that although the costs for running RANS are relatively low, the time averaging process can completely destroy unsteady effects. Even for obtaining a time-averaged flow solution only, results can be strongly dependent on the characteristics of turbulence models. This means that one needs to choose specific models for relevant flow phenomena (e.g. $k-\epsilon$ model for planar shear layers and recirculating flows, $k-\omega$ model for wall effects), and there is no universal model that works for all flows. Studies [150, 81] have demonstrated the poor performance of RANS models when simulating shear layers. It was shown that RANS may not be suitable for calculating unsteady distortion induced by shear layer in fan-intake interaction. This defect of RANS will be further investigated in Chapter 8.

3.2.3 URANS

Unlike RANS which smears all unsteady main flow features, the URANS maintains large scale unsteadiness and coherent structures by using an ensemble averaging decomposition,

$$\phi(\boldsymbol{x},t) \equiv \langle \phi(\overline{\boldsymbol{x}},t)\rangle + \phi'(\boldsymbol{x},t). \tag{3.40}$$

Similarly, the fluctuation or turbulence part is still approximated by RANS models, but the large scale unsteadiness is resolved directly. By using this decomposition, the original NS equation becomes,

$$\begin{aligned}
\frac{\partial \bar{\rho}}{\partial t} + \frac{\partial \bar{\rho}\bar{u}_i}{\partial x_j} &= 0, \\
\frac{\partial \bar{\rho}\bar{u}_i}{\partial t} + \frac{\partial \bar{\rho}\bar{u}_i\bar{u}_j}{\partial x_j} &= \frac{\partial}{\partial x_j}\left(-\bar{p}\delta_{ij} + \bar{\sigma}_{ij} + \tau_{ij}^R\right), \\
\frac{\partial \bar{\rho}\bar{e}}{\partial t} + \frac{\partial \bar{\rho}(\bar{e}+\bar{p})\bar{u}_j}{\partial x_j} &= \frac{\partial}{\partial x_j}\Big[\left(\bar{\sigma}_{ij} + \tau_{ij}^R\right)\bar{u}_i + \overline{\sigma_{ij}u_i'} - \frac{1}{2}\overline{\rho u_i' u_i' u_j'} \\
&\quad -\bar{q}_j + c_p\overline{\rho u_j' T'}\Big].
\end{aligned} \tag{3.41}$$

Note that the only differences are the additional unsteady terms $\frac{\partial \bar{\rho}}{\partial t}, \frac{\partial \bar{\rho}\bar{u}_i}{\partial t}, \frac{\partial \bar{\rho}\bar{e}}{\partial t}$ compared to RANS.

3.2.4 LES

As discussed in Chapter 2, (U)RANS may not accurately predict the unsteady behaviour for the flow without spectral gaps. The LES, shown in the middle of the hierarchical turbulence modelling (Fig.1.5), can be a possible way to tackle this problem. For

example, in separated flows induced by a bluff body, unsteady structures are highly and intrinsically determined by the body geometry. As a result, the turbulence length scale can be as large as the separation bubble size. This means that (U)RANS resolves the large scale turbulence but also estimates it using specific models, hence double accounting the effects of large turbulent eddies. To avoid the inaccuracy of these models, LES only directly resolves those large scale turbulence structures and simulates its development with higher time accuracy. In such a way, the large eddies can be thoroughly independent from the relevant body geometry, and less rely on turbulence models.

Governing Equations

The essential difference from (U)RANS is that the LES uses a filtering kernel to decompose the NS equation and hence resolves the large scale eddies. This is achieved by the spatial decomposition

$$\phi(\boldsymbol{x}, t) \equiv \hat{\phi}(\boldsymbol{x}, t) + \phi'(\boldsymbol{x}, t). \tag{3.42}$$

By substituting the spatial decomposition, we obtain the NS equation for the compressible LES, which is

$$\begin{aligned} \frac{\partial \hat{\rho}}{\partial t} + \frac{\partial \hat{\rho}\hat{u}_i}{\partial t} &= 0, \\ \frac{\partial \hat{\rho}\hat{u}_i}{\partial t} + \frac{\partial \hat{\rho}\hat{u}_i\hat{u}_j}{\partial t} &= \frac{\partial}{\partial x_j}\left(-\hat{p}\delta_{ij} + \hat{\sigma}_{ij} + \tau_{ij}^{SGS}\right), \\ \frac{\partial \hat{\rho}\hat{e}}{\partial t} + \frac{\partial \hat{\rho}(\hat{e}+\hat{p})\hat{u}_j}{\partial x_j} &= \frac{\partial}{\partial x_j}(\hat{\sigma}_{ij}\hat{u}_i - \hat{q}_j + \beta). \end{aligned} \tag{3.43}$$

Note that the stress term is split into the viscous tensor $\hat{\sigma}_{ij}$ and the subgrid-scale (SGS) stress τ_{ij}^{SGS}. The former viscous stress term can be computed using viscosity μ. The latter comes from the difference between the two filtering orders,

$$\tau_{ij}^{SGS} = -(\widehat{\rho u_i u_j} - \hat{\rho}\hat{u}_i\hat{u}_j). \tag{3.44}$$

This resembles the Reynolds stress in (U)RANS, but instead of time averaging, it is created by spatial filtering and only applies for flow structures smaller than the filtering kernel. Similar to Eq.3.27, based on the eddy viscosity analogy, the combined stress

can be expressed as

$$\hat{\tau}_{ij} = 2(\mu + \mu_{SGS}) \left(\bar{S}_{ij} - \frac{1}{3} \frac{\partial \bar{u}_k}{\partial x_k} \delta_{ij} \right). \tag{3.45}$$

The subgrid-scale viscosity is to be calculated using σ model in the following section.

In the energy equation, the heat flux q_j is estimated by Fourier's law 3.20. The term β contains the following terms,

$$\beta = \widehat{\rho u_i T} - \hat{\rho}\hat{u}_i\hat{T} + \frac{1}{2}\widehat{\rho u_i u_i u_j} - \frac{1}{2}\hat{\rho}\hat{u}_i\hat{u}_i\hat{u}_j. \tag{3.46}$$

The first two terms are modelled by Moin et al. [110]:

$$\widehat{\rho u_i T} - \hat{\rho}\hat{u}_i\hat{T} = -\frac{\mu_t}{Pr_t}\frac{\partial T}{\partial x_i}. \tag{3.47}$$

Assuming the convection of the kinetic energy of subgrid turbulence is small, the rest term $1/2(\widehat{\rho u_i u_i u_j} - \hat{\rho}\hat{u}_i\hat{u}_i\hat{u}_j)$ is ignored.

At the beginning of this section, we noted that LES applies a spatial decomposition to "select" large eddies. This is done by using a filtering kernel $G(\phi)$ and a convolution of an unfiltered solution. This works as

$$\hat{\phi} = G(\phi) \star \phi \tag{3.48}$$

In practice, instead of using an explicit filtering kernel due to its substantial computational costs, the filtering process is achieved by the grid. This also decouples filtering and modelling of the numerical method so that the numerical dissipation can be controlled. In this way, the phrases "filtered" and corresponding "residual" terms are not used. Instead, it is common to say that the large scale turbulence is "resolved" and the "subgrid" turbulence is modelled.

Sigma Model

The research applies the σ model [113] for the SGS turbulence. This is because the model can reduce the defects of SGS viscosity with a switch for filtering only when needed. By using this model, the SGS term can vanish automatically when turbulence become two-component hence the prediction becomes less model dependent.

Classical subgrid-scale viscosity models are modelled in the form,

$$\mu_{SGS} = \rho(C_S\Delta)^2\mathcal{D}, \tag{3.49}$$

where C_S is the model constant, Δ is the subgrid characteristic length scale (usually the grid size) and $\mathcal{D}$ is a differential operator determined by specific models. For example, the Smagorinsky model applies $C_S \approx 0.18, \mathcal{D} = \sqrt{2S_{ij}S_{ij}}$. However, the operator does not vanish in near-wall regions. This problem can be tackled by using WALE (Wall Adapting Local Eddy viscosity) [112] or Vreman's model [162]. However, these models do not vanish for pure rotation flows. Nicoud et al. [113] concludes the properties that an ideal model should have

1. a positive value involving local velocity gradients,
2. cubic behaviour near solid boundaries,
3. zero for 2-component or 2D flows,
4. zero for axisymmetric or isotropic expansion/contraction.

Base on these facts, they proposed the σ model by using the invariants $\mathcal{I}_i$ of the matrix formed by velocity gradients. In the model, $C_S = 1.35$ calibrated by Nicoud and the operator is constructed by,

$$\mathcal{D}_\sigma = \frac{\sigma_3(\sigma_1 - \sigma_2)(\sigma_2 - \sigma_3)}{\sigma_1}, \tag{3.50}$$

where $\sigma_{1/2/3}$ are the singular values of the velocity gradients calculated in the following way. First use the velocity gradient tensor to create the matrix G_{ij} and obtain its invariants,

$$\begin{aligned} G_{ij} &= \frac{\partial u_i}{\partial x_k}\frac{\partial u_k}{\partial x_j}, \\ \mathcal{I}_1 &= \mathrm{tr}(G_{ij}), \\ \mathcal{I}_2 &= \frac{1}{2}(\mathrm{tr}(G_{ij})^2 - \mathrm{tr}(G_{ij}^2)), \\ \mathcal{I}_3 &= \det(G_{ij}). \end{aligned} \tag{3.51}$$

Then the eigenvalues of G_{ij} can be calculated from the equation

$$x^3 - \mathcal{I}_1 x^2 + \mathcal{I}_2 x - \mathcal{I}_3 = 0. \tag{3.52}$$

Hence, the singular values of the velocity gradient tensor are $\sqrt{x_i}$. Alternatively, instead of solving the equation, the roots can be also solved using a self-contained method [66],

which does not require an external library, e.g. LAPACK. First, compute the values

$$\begin{aligned}\alpha_1 &= \frac{\mathcal{I}_1^2}{9} - \frac{\mathcal{I}_2}{3},\\ \alpha_2 &= \frac{\mathcal{I}_1^3}{27} - \frac{\mathcal{I}_1\mathcal{I}_2}{6} + \frac{\mathcal{I}_3}{2},\\ \alpha_3 &= \frac{1}{3}\arccos\frac{\alpha_2}{\alpha_1^{3/2}}.\end{aligned} \tag{3.53}$$

Then the singular values are

$$\begin{aligned}\sigma_1 &= \left(\frac{\mathcal{I}_1}{3} + 2\sqrt{\alpha_1}\cos\alpha_3\right)^{1/2},\\ \sigma_2 &= \left(\frac{\mathcal{I}_1}{3} - 2\sqrt{\alpha_1}\cos\left(\frac{\pi}{3} + \alpha_3\right)\right)^{1/2},\\ \sigma_3 &= \left(\frac{\mathcal{I}_1}{3} - 2\sqrt{\alpha_1}\cos\left(\frac{\pi}{3} - \alpha_3\right)\right)^{1/2}.\end{aligned} \tag{3.54}$$

This method is adopted in the code to improve the computational efficiency. Scillitoe [134] has demonstrated that this σ model performed well for flows in compressors and does not require additional filtering or averaging. Hence, it was used for the present LES computation.

3.3 Equation Solving

3.3.1 Governing Equations

Both the geometry and turbulence modelling terms represented by f_i and τ_{ij}^R (or τ_{ij}^{SGS}) are finally implemented into the compressible Navier–Stokes equations. The equation is then solved by using the Finite Volume Method in the strong conservation form,

$$\frac{\partial}{\partial t}\int_V \boldsymbol{q}\,\mathrm{d}V + \oint_V R(\boldsymbol{q})\cdot\mathrm{d}\boldsymbol{A} = \int_V S(\boldsymbol{q})\,\mathrm{d}V, \tag{3.55}$$

where V and A are the volume and surfaces of an infinitesimal element within a computational domain, and $\boldsymbol{q}$ contains the primitive quantities. The vectors are

$$\boldsymbol{q} = \begin{pmatrix} \rho \\ \rho u_1 \\ \rho u_2 \\ \rho u_3 \\ \rho e \end{pmatrix}, R(\boldsymbol{q}) = \begin{pmatrix} \rho u_i \\ \rho u_1 u_i + p\delta_{i1} \\ \rho u_2 u_i + p\delta_{i2} \\ \rho u_3 u_i + p\delta_{i3} \\ (\rho e + p)u_i \end{pmatrix} - \begin{pmatrix} 0 \\ \tau_{i1} \\ \tau_{i2} \\ \tau_{i3} \\ \tau_{ij}u_j + \varphi \end{pmatrix}, S(\boldsymbol{q}) = \begin{pmatrix} 0 \\ f_{b,1} \\ f_{b,2} \\ f_{b,3} \\ f_{b,i}u_i \end{pmatrix}, \quad (3.56)$$

where τ_{ij} contains both the viscous and turbulent stresses. The term φ in the energy equation is given by,

$$\varphi = c_p \left(\frac{\mu}{Pr} + \frac{\mu_t}{Pr_t} \right) \frac{\partial}{\partial x_j} \left(\frac{p}{\rho} \right). \quad (3.57)$$

The term $R(\boldsymbol{q})$ is split into inviscid and viscous terms.

The resolution of this equations is based on HYDRA, which is a cell vertex based, unstructured solver for compressible flows, using Finite Volume Method from Moinier [111]. The spatial and temporal discretisation are discussed in the following sections.

3.3.2 Spatial Discretisation

The fundamental idea of spatial discretisation is illustrated in Figure 3.2, where dual median control volumes (the grey zone) are applied and nodes i and j are connected by the edge e_{ij} . The unknown primitive quantities are stored on the computational nodes.

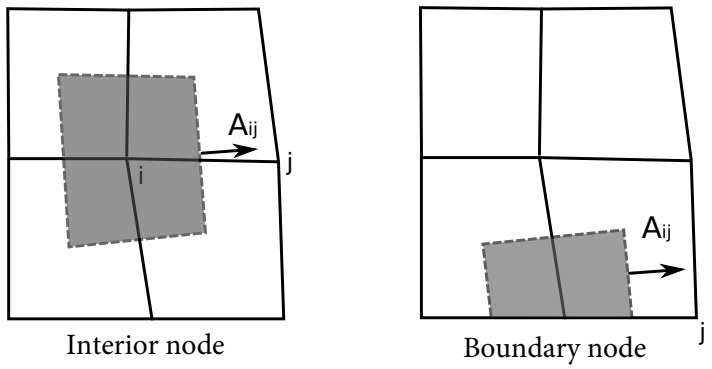

Fig. 3.2 Control volume for interior and boundary nodes

For interior nodes i in Frame (a), the control volumes are constructed surrounding the node and enclosed by the control surfaces. Each control surface A_{ij} can be calculated by the corresponding cell edge. For nodes at boundaries shown in Frame (b), one of

the control surfaces is just the bounding edge. Thus the spatial term can be further discretised as

$$\oint_V R(\boldsymbol{q}) \cdot \mathrm{d}\boldsymbol{A} = \frac{1}{V_i} \sum_{j \in E_i} \mathcal{F}_{ij} A_{ij}. \tag{3.58}$$

The $\mathcal{F}_{ij}$ is the numerical flux through the control surface, A_{ij} is the edge weight, and E_i is the set of all the nodes linked with the node i. Hence, HYDRA loops through all the control columns and computes these summations.

Inviscid Flux

The inviscid flux in Eq.3.55 is calculated by Roe flux-differencing scheme [129],

$$\mathcal{F}_{ij}^I = \underbrace{\frac{1}{2}\left(\mathcal{F}_i^I + \mathcal{F}_j^I\right)}_{\text{Central difference}} - \underbrace{\frac{1}{2}\epsilon_2 |A_{ij}| \left(\mathcal{L}_i(q_i) - \mathcal{L}_j(q_j)\right)}_{\text{Upwind}}, \tag{3.59}$$

where $|A_{ij}|$ denotes the flux Jacobian $\partial F_{ij}^I / \partial q_i$, ϵ_2 is a smoothing constant, and $\mathcal{L}_i$ is a Laplacian operator defined by

$$\begin{aligned} \mathcal{L}_i &= \hat{L}_i - \nabla q_i \hat{L}_i, \\ \hat{L}_i &= \sum_{i \in E_i} \frac{q_i - q_j}{|\boldsymbol{x}_i - \boldsymbol{x}_j|} \Big/ \sum_{i \in E_i} \frac{1}{|\boldsymbol{x}_i - \boldsymbol{x}_j|} \\ \nabla q_i &= \sum_{i \in E_i} \frac{1}{2}(q_i + q_j) n_{ij} A_{ij}. \end{aligned} \tag{3.60}$$

The formula 3.59 means that the Roe scheme is a mixture of both the central difference and upwind schemes, scaled by the smoothing constant ϵ_2. The pure central difference scheme may have dispersive errors, or "wiggles" [134] that can damage flow solutions. Hence, the upwind scheme can prevent such wiggles by adjusting ϵ_2 [129].

The scheme works well for RANS simulations because the numerical dissipation improves convergence. However, when applied to LES, the upwind scheme may lead to excessive numerical dissipation in turbulence. This could be improved by using higher order schemes. Wang et al. [163] explored a range of higher order methods and found that they performed better on 2D flows. However, this is also case specific. The comparison between 2nd and 6th order scheme from Meinke et al. [104] for LES turbulent jet flows shows that the results are still comparable. In addition, the main issue that prevents the industrial application of high order schemes is its computational efficiency. As Wang et al. noted, these schemes requires (1) robust high order mesh generation, (2) massive memory when using implicit time stepping, (3) and

complicated computational parallelisation. By contrast, the present 2nd order scheme provides a substantial advantage for solving large scale problems due to the reduced information transfer among grid points. This renders the parallelisation on processors more efficiently. To reduce the drawbacks of this 2nd order scheme, the following steps were taken to improve its accuracy.

1. Use grid filtering to decouple filtering and modelling from the numerical schemes, as discussed in Section 3.2.4.

2. Use finer grid resolution to reduce discretisation errors, as proposed by Vreman et al. [162]

3. Use a flux limiter to blend a dissipative (e.g. upwind) and central differencing so that the dissipation can be controlled. Also, Roe [129] found that flows with high Mach number could be less dissipative. Since the study for Mach number in the research is around 0.4, the numerical dissipation can be limited. The present thesis set $\epsilon_2 = 0.1$, which has been validated in similar scenarios [164, 165, 41, 134].

Viscous flux

The viscous flux is calculated at the midpoint of the edge. As the point is also on the associated dual median control volume faces, the viscous flux is constructed in the same way as the inviscid flux, and the additional term is computed using the central difference,

$$\nabla q_{ij} = \frac{1}{2}\left(\nabla q_i + \nabla q_i\right). \tag{3.61}$$

However, due to the defect of the central difference scheme, the high frequency modes cannot be damped. This means that in the boundary layer region the viscous terms become dominant, and consequently the dispersion can be significant. This issue can be addressed by modifying the scheme according to Moinier [111].

$$\begin{aligned} \nabla q_{ij} &= \nabla q_{ij} - \left(\nabla q_i \delta s_{ij} - \frac{|q_i - q_j|}{|\boldsymbol{x}_i - \boldsymbol{x}_j|}\delta s_{ij}\right), \\ \delta s_{ij} &= \frac{\boldsymbol{x}_i - \boldsymbol{x}_j}{|\boldsymbol{x}_i - \boldsymbol{x}_j|}. \end{aligned} \tag{3.62}$$

3.3.3 Temporal Discretisation

An investigation of various time-stepping schemes was provided by Larsson [82]. He proposed that when using an explicit scheme, the costs can be significantly less expensive per time-step than a fully implicit one. Scillitoe [136] also noted that the 5-stage Runge-Kutta explicit scheme [101] can save the computing time whilst ensuring accurate prediction of high frequency turbulence. Hence, this type of time scheme is chosen for the present study and done by

$$\boldsymbol{q}^{n+1} = \boldsymbol{q}^{n} - \Delta t \sum_{k=1}^{5} \alpha_k R^k, \tag{3.63}$$

where k is the stage number, and R^k is the residual

$$R^k = \frac{1}{V_i}\left(\sum_{j \in E_i} \mathcal{F}_{ij}^k A_{ij} - S_i^k V_i\right). \tag{3.64}$$

The coefficients α_k are given by

$$\alpha_1 = \frac{1}{4}, \alpha_2 = \frac{1}{6}, \alpha_3 = \frac{3}{8}, \alpha_4 = \frac{1}{2}, \alpha_5 = 1. \tag{3.65}$$

In the residual of each control volume R^k, the convection and dissipation terms are computed at different rates to improve efficiency. This is because the dissipation terms are more expensive to compute. To do this, the residual term are split into

$$\begin{aligned} R^k &= C^k - B^k, k = 1, 2, ..., 5 \\ B^k &= \beta_k D^k + (1 - \beta_k) B^{k-1}. \end{aligned} \tag{3.66}$$

where

$$\begin{aligned} C^k &= \frac{1}{V_i} \sum_{j \in E_i} \mathcal{F}_{ij}^{I,k} A_{ij} \\ D^k &= \frac{1}{V_i}\left(\sum_{j \in E_i} \mathcal{F}_{ij}^{V,k} A_{ij} - S_i^k V_i\right) + \varepsilon_N. \end{aligned} \tag{3.67}$$

$C(q^k)$ is the convective contributions to the residual, D^k contains physical dissipation and numerical dissipation (ε_N). In practice, β is set to zero every other calculation:

$$\beta_1 = 1, \beta_2 = 0, \beta_3 = \frac{14}{25}, \beta_4 = 0, \beta_5 = \frac{11}{25}. \tag{3.68}$$

This means that the intermediate term B^0 and the terms D^2, D^4 are not needed.

The time-step is determined by the Courant-Friedrichs-Lewy (CFL) number at the local cell and for compressible flows, this is defined as

$$\Delta t = \frac{CFL\Delta x}{\max\left(|u_i| + a\right)}, i = 1, 2, 3. \tag{3.69}$$

where Δx is the smallest grid width, u_i are the 3D flow velocities, and a is the speed of sound.

3.3.4 Grid Technique

It should be noted that the global time-step is determined by the smallest one within the computational domain. Therefore, the global time-step could be even smaller for highly non-uniform grids because of a few small cells. This means that the simulation times could be even longer. Hence, structured grids are used for all the present cases. In terms of the meshing technique, a 4-level multi-grid was employed for RANS simulation, which considerably reduces the low frequency errors and thus accelerates the convergence. The fundamental concept of this technique is to use a sequence of coarser grids that can iteratively smooth and eliminate high frequency error modes on the finer grid. This is an essential part of steady flow simulation algorithms. However, it is still not understood that how such multigrid technique will affect the unsteady simulation and force terms in the present research, so only a single level grid is applied for URANS and LES.

Chapter 4

Validation of Mixed-fidelity Method

In this Chapter, the proposed hierarchical modelling methods are validated against data from Wartzek's experiment [168] and Directly Mesh Resolved (DMR) case. The aim is to show that (a) both the standard IBM and the eIBM are able to construct proper boundary conditions for the target region and (b) the IBM is able to provide the same turbulence information as the DMR method. To demonstrate the performance, the IBM and the eIBM with both local and global forces are investigated and compared via the simulation of the Darmstadt Transonic Rotor and NASA Rotor 67 for validating the velocity and pressure distributions in the region of fan-intake interaction; the IBM is tested on a triangular prism for validating turbulence statistics.

The eIBM in the present research has two forms: one with global forces (eIBMg) and the other with local force (eIBMl). Both forms are validated in terms of flow distributions, including static and total pressure, Mach number at a range of axial, radial and circumferential locations. A whole working range of Darmstadt Transonic Rotor is also explored using eIBMg and compared against experiment data. These cases are run by RANS+eIBMg, URANS+eIBMl, URANS+DMR (Mentor $k-\omega$ SST model) and LES+IBM. As for flow features in the region of fan-intake interaction, we concentrate on the local force model since it can present more details. Finally, both local and global models are compared quantitatively in terms of total pressure distribution at a range of locations. Comments are made on their advantages and drawbacks.

Table 4.1 Key parameters of the Darmstadt Transonic Compressor, from Wartzek[168]

max. power	800 kW	
max. torque	350 Nm	
Design speed	20,000 rpm	
Outer diameter	0.38 m	
Hub-to-tip-ratio	0.51	
Rotor/Stator blades	16/29	
Rotational Speed	Massflow rate	Outlet static pressure
100%	16kg/s	135000 Pa
65%	10.6kg/s	120000 Pa

4.1 Darmstadt Transonic Rotor

4.1.1 Case Framework

The first test case on the Darmstadt Transonic Rotor is motivated by experimental studies in Ref.[87, 114, 156, 16, 168], where distortion generators were designed to reproduce flow conditions in a real engine within a laboratory. Measurements by Lieser [87] and Bitter [16] showed that the compressor performance is the most sensitive to distortions encountered at the blade tip. Hence, in order to reproduce the distortion encountered over the intake lip at a high angle of attack, a distortion generator is placed upstream of the fan tip. The key parameters of the Darmstadt Rotor are listed in Table 4.1 and a sketch of the flow domain is shown in Fig.4.1. The numerical

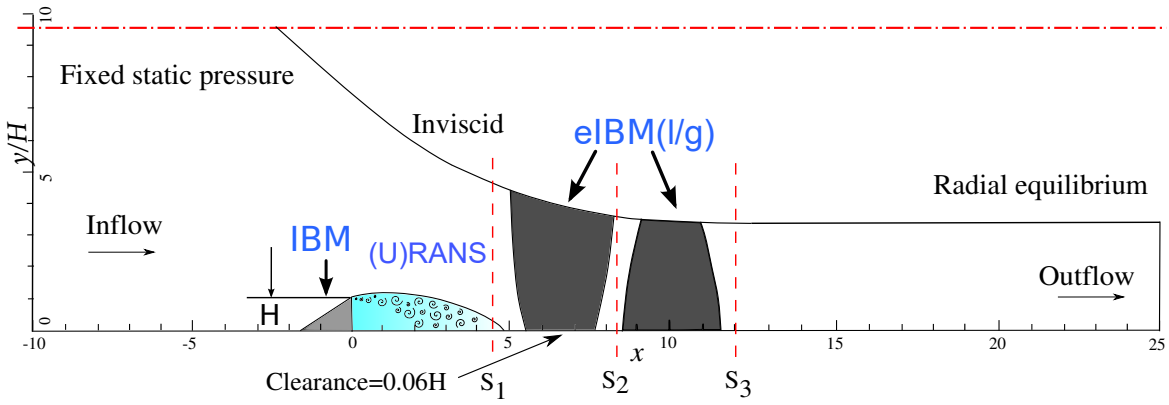

Fig. 4.1 Full-annulus case: boundary conditions and monitored planes

simulation includes an IBM-modelled distortion generator, which covers 120° in the circumferential direction and an eIBMg modelled rotor and stator. The rest of the domain is computed using RANS and URANS, with $k-\omega$ model. International Standard Metric Conditions ($p_0 = 101325$ Pa and $T_0 = 288.15$ K) are applied at the inlet flow and the target mass flow rate is 16.0 kg/s for 100% and 10.6 kg/s for 65%, corresponding to peak efficiency points. The outlet has fixed static pressures with radial equilibrium conditions. The maximum Mach number at blade tip is 1.16 for 100% rotational speed and 0.75 for 75%. The tip clearance is 1.5% (clearance/span). The eIBM with both local and global force are tested on a full-annulus rotor to explore the main flow features. The distortion generator is the same as the one in Wartzek's [168] test. It is modelled using PI feedback forcing (Eq.3.1), whereas both the rotor and stator are modelled using indirect forcing with distribution functions (Eq.3.11). The coefficient k in parallel forcing (Eq.3.7) is calibrated by the steady performance data p_t and $\dot{m}$ from Wartzek's experiment [168]. In this case, $k = 2.0$ and is kept the same for all the operating points. The data from an eIBM case, a DMR (distortion generator, rotor, and stator) case, and the experiment [168] are also compared.

Both the eIBMl and eIBMg case use the same mesh with 12.4M nodes, compared to the DMR case with 61.4 M nodes. A sketch of the meshes used in these two cases is depicted in Fig.4.2, where Frame (a) and (b) shows the actual two types of mesh and Frame (c) and (d) shows the coarsened versions to reveal the blade locations. The data are compared and validated at three cross-sections, $S1 = 3.5$, $S2 = 8.5$ and $S3 = 12$ (Fig.4.1). Figure 4.2e depicts the magnitude of the force contours near the casing (90% of the blade height) for the beam, rotor, and stator blades in the $x-\theta$ plane. The values of forces for the rotor and stator are different due to their status of motion. It shows that the blade angle and its camber line are well reproduced.

4.1.2 Performace Map

The performance map from the eIBMg case is compared with Wartzek's experiment [168] in Fig.4.3. The simulations were run at both 100% (Frame (a)) and 65% (Frame (b)) rotational speed. The IBM beam and eIBMg fan can characterise the general trend in the performance. For the case with 100%RS in Frame (a), the stall point given by the experiment (for both smooth casing and the one with distortion) is around 1.37kg/s. However, for the RANS+eIBMg, the massflow rate fluctuates and finally diverges at 1.42kg/s, 3.6% higher than the actual stall point. This is perhaps because when the compressor runs close to the stall point, the direction of relative flow velocity significantly deviates from rotor blade angle. As a result, the forcing

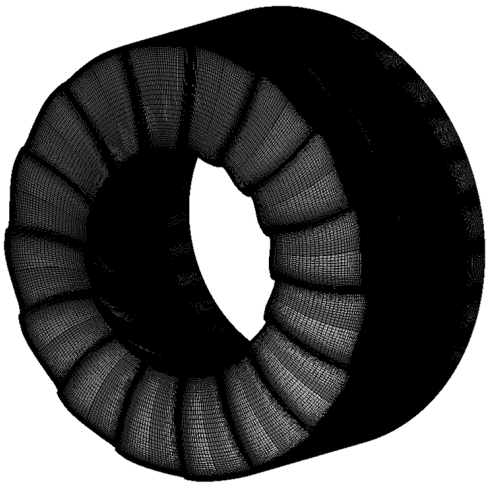

(a) Body-fitted mesh, 61.4M nodes

(b) Cartesian mesh, 12.4M nodes

(c) Sketch of DMR blades (blade surface only for viewing)

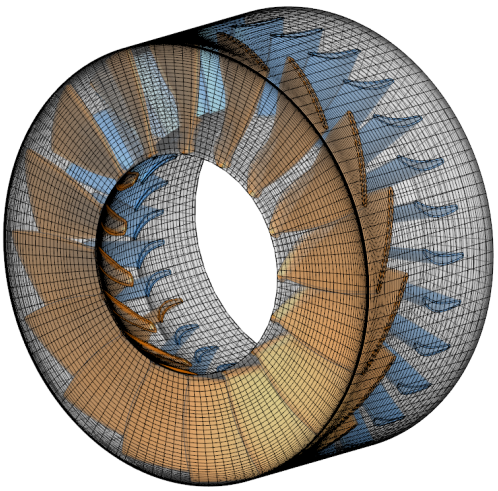

(d) Sketch of eIBMl blades (coarsened for the view)

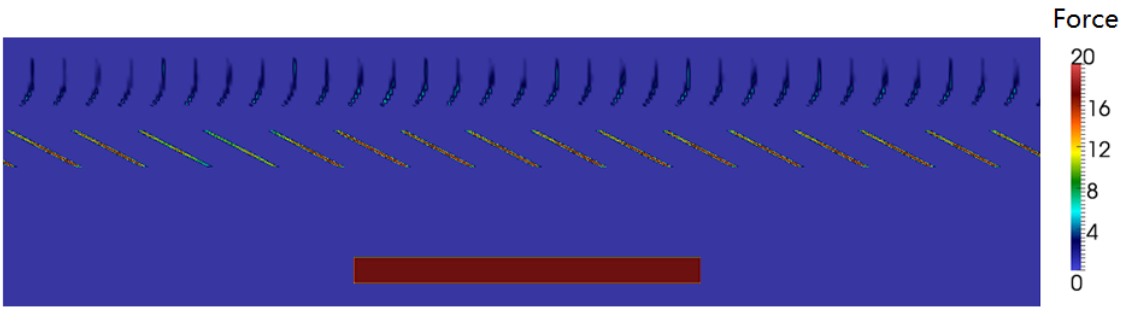

(e) Force region of IBM and eIBMl (Non-dimensionalised by $\rho_0 U_0^2/H$)

Fig. 4.2 Test cases with (a) Body-fitted mesh, (b) eIBMl/eIBMg mesh, (c) Coarsened Body-fitted mesh (d) Coarsened eIBMl/eIBMg mesh (e) Force Region

model may start with some small fluctuations and finally fail to drive the flow towards the designed direction. Since the blade is replaced by "dynamics" forces (created by velocity difference) instead of rigid boundaries, the divergence can start earlier than the actual situations. There are the similar discrepancies for the case with 65% RS shown in Frame (b). It should also be noted that the choking mass flow rate of 16.4 kg/s cannot be approached by the eIBMg in Frame (a). This could be resulted from the strong blockage introduced by the assumption of an infinite numer of blades. Within the original blade passages, the loss effect from the parallel force model behaves as a blockage and hence reduces the maximum massflow rate.

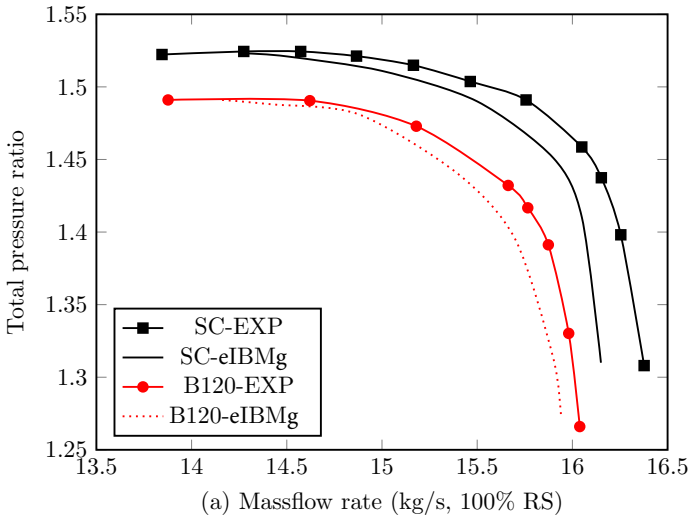

(a) Massflow rate (kg/s, 100% RS)

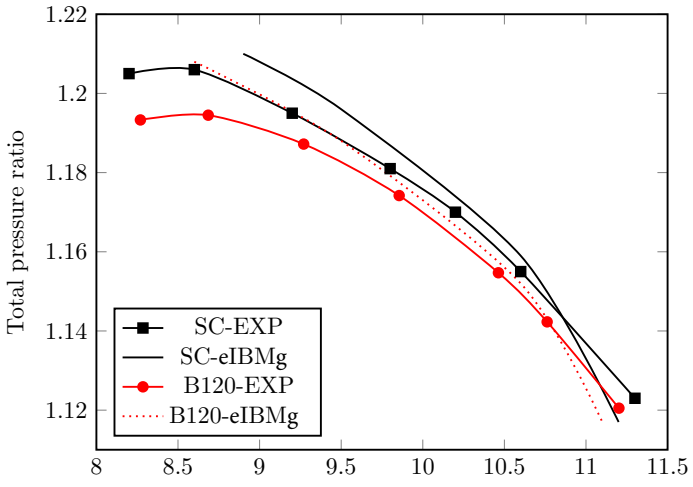

(b) Massflow rate (kg/s, 65% RS)

Fig. 4.3 Performance map of the Darmstadt Rotor at (a) 100% speed and (b) 65% speed. SC represents Smooth Casing and B120 for a 120° beam.

4.1.3 Flow Features

To validate how the combination of IBM beam and eIBM fan characterise the separation behaviour, the data from both DMR and eIBMg cases are compared in this section. These were run at (a) 100% RS and 16.0kg/s massflow rate and (b) with 65% RS and 10.6kg/s massflow rate. This section discusses the flow features in three regions: (a) fan-intake, (b) tip clearance and (c) blade region.

Fan-intake interaction

First, the eIBMg fan is compared with the DMR fan in terms of the mass flux distribution shown in Fig. 4.4. The data is extracted at the plain S_1 labelled in Fig.4.1. The y axis originates from the casing to the hub, referenced by the height of the beam. In this figure, the radial location is the relative blade height; the mass flux is referenced to the area average. The data were extracted at a distance of 10% of the blade chord upstream of the rotor entrance. It is obvious that the momentum deficit occurs between $R = 0$ and $1.5H$, where the beam is installed. These results demonstrate that, although

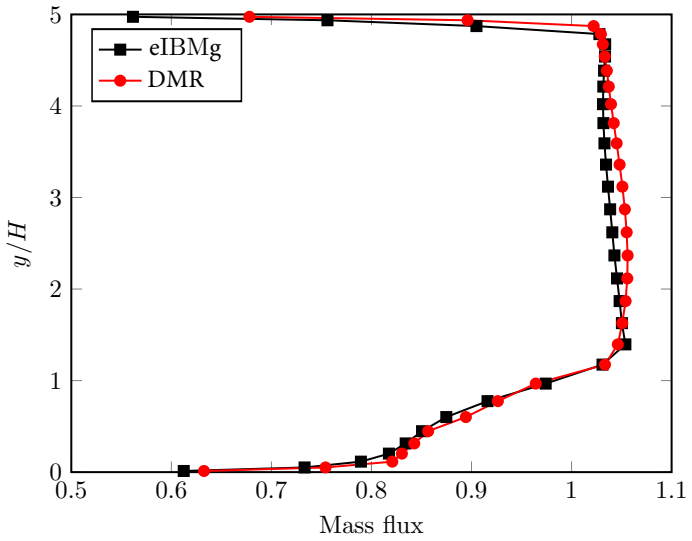

Fig. 4.4 Radial distribution of mass flux from eIBMg modelling and Resolved cases, 100%RS and 16.0kg/s

the separation affects the total pressure distributions across the rotor and stator, the eIBMg rotor can still accurately capture the main flow features upstream the rotor compared to the experiment and resolved case. This means that separated flows do not have an obvious impact on the application of the eIBMg method. This is because the force in eIBMg includes three aspects: normal force, parallel force and blade solidity

(i.e. blockage ratio). The normal force reduces the normal velocity difference to zero, whereas the resistance from the parallel force has been calibrated by the experiment data. These two factors are not substantially changed by the separated flows. For the solidity, Plourde and Stenning [121] also demonstrated that the cascade solidity has no influence on the attenuation. Hence, even if the solidity may affected by separation, it still does not change the suppression of distortion.

Then the following content in this section mainly focuses on the eIBMl. Compare to the eIBMg, this method is able to reflect more flow details and blade configuration, shown in Fig. 4.5. It depicts the iso-surface of the Q-criterion at 5×10^6 for the full-annulus case at 100% speed. The Q-criterion can be calculated by

$$Q = \frac{1}{2}\left[\mathrm{tr}\left(\frac{\partial u_i}{\partial u_j}\right)^2 - \mathrm{tr}\left(\frac{\partial u_i}{\partial u_j}^2\right)\right] = \frac{1}{2}\left(\frac{\partial u_i}{\partial u_i}\frac{\partial u_j}{\partial u_j} - \frac{\partial u_i}{\partial u_j}\frac{\partial u_j}{\partial u_i}\right). \tag{4.1}$$

The view is taken from the inlet, and evidently the distortion generator creates substantial separated flows in front of the rotor. The rotor with 16 blades can be clearly represented using the eIBMl. Both the blade configuration and its thickness are well modelled. The total pressure distribution upstream of the rotor and downstream of the stator from instantaneous flow solutions are depicted in Fig.4.6. In Frame (a), the distortion area is well represented. The pressure wave induced by the downstream blades propagates to the fan face, resulting in the intermittency of total pressure peaks in the circumferential distribution. The distribution downsteam the stator in Frame (b) also clearly shows the intermittency caused by stator blades. Note that the total pressure is higher in the distortion region because the blade work is higher for the reduced massflow rate. These show that the effects of the modelled distortion generator, the rotor, and the stator can be represented and the general flow features can be captured.

The case with 65%RS and 10.6kg/s was also compared. Figure 4.7 shows the contours extracted near the casing within the blade clearance. Frame (a) depicts the static pressure distribution with a distortion generator placed at the centre in the upstream. The pressure rise across the rotor blade and its intermittent pressure wave towards the upstream are well captured. The pressure drop ($p < 1.0$, depicted in blue) around the blade leading edge is also correctly represented. Evidently, the separated flows from the distortion generator can impact the region around the fan leading edge. The distribution of the Ma number shown in Frame (b) (in the absolute frame) reveals the impact of the separation on the blade tip. The flow within the distortion region is strongly accelerated in both cases. This is because, when the separation enters the

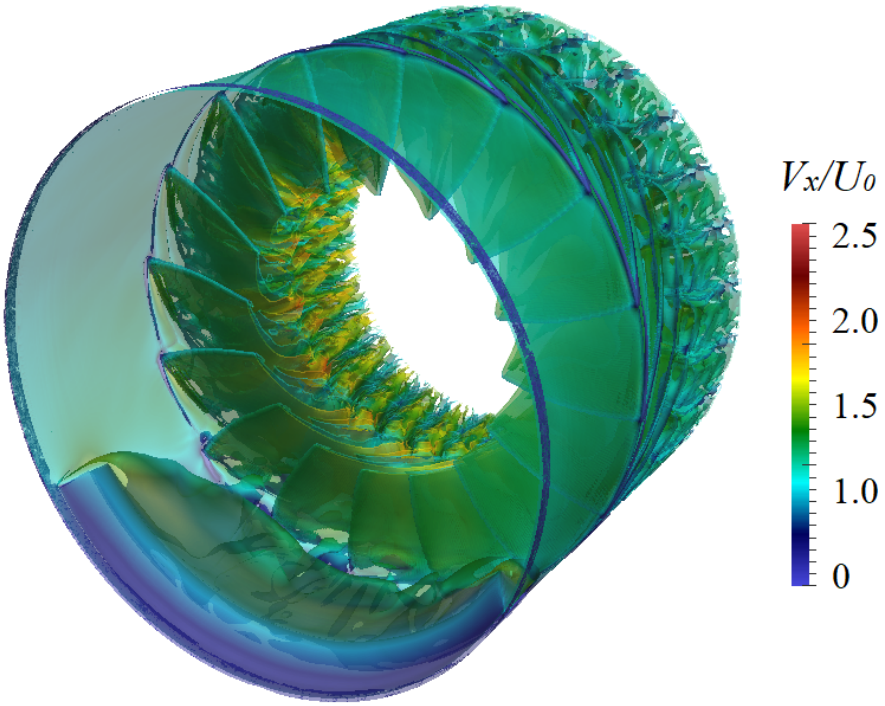

Fig. 4.5 Iso-surface of Q-criterion 5×10^6, coloured by axial velocity, 100%RS and 16.0kg/s

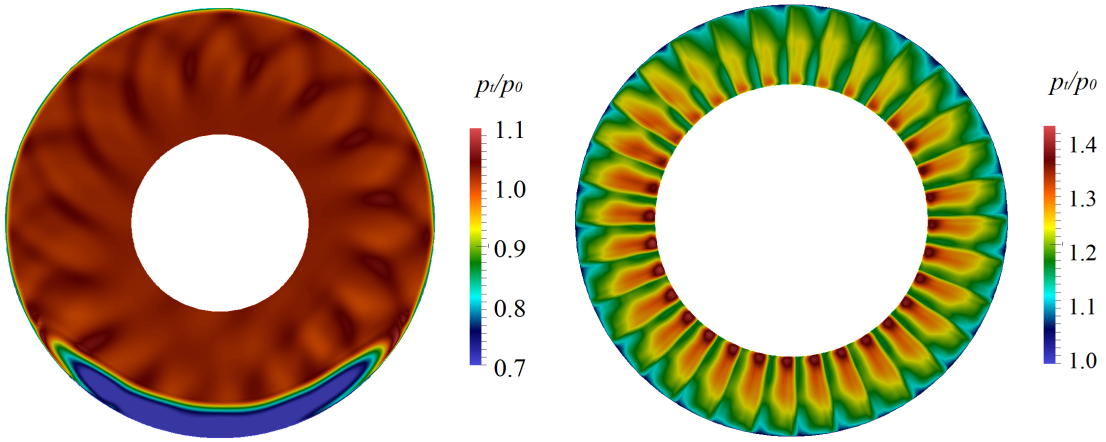

(a) Rotor inlet (b) Stator outlet

Fig. 4.6 Distribution of total pressure at (a) Rotor upstream, (b) Stator downstream, 100%RS and 16.0kg/s

blade passage, it reduces the static pressure on the pressure surface and hence increases the pressure difference across a blade. Consequently, this difference accelerates the flow within the tip clearance and thus the magnitude of the Ma number increases.

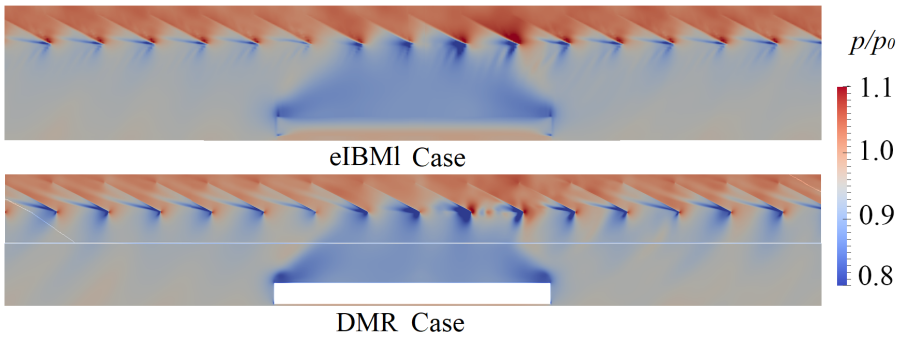

(a) Static pressure (referenced by $p_0 = 101325Pa$)

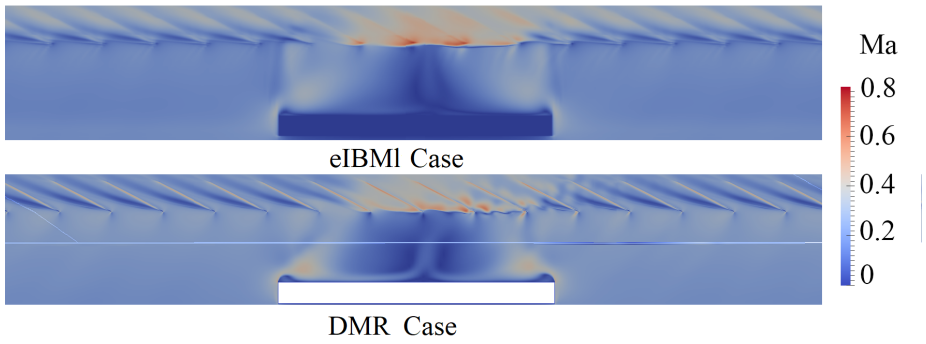

(b) Mach number

Fig. 4.7 Distribution of (a) static pressure and (b) absolute Mach number near casing (within tip clearance), 65%RS and 10.6kg/s

The scale of the separation bubble can also be revealed using the time-averaged flow solution shown in Fig.4.8. The separation region at the casing is contoured by the boundary of $v_x = 0$. Evidently, this eIBMl case is able to characterise the development of the separation and the bubbles on each side. The flow separates at the two side edges of the beam but reattaches and avoids further interaction. Hence, in the centre, the flow turn towards the positive x direction and there is almost no reverse flow.

At the entrance to the intake ($x = -10H$ in Fig.4.1)), the static pressure distribution in the middle of the radial location ($r = 0.5R$) is extracted and transformed by using a fast spatial Fourier transform, as shown in Fig.4.9. The first-order harmonic wave number $k = 1/16$ is captured by both methods, which corresponds to the number of rotor blades $N = 16$; the second-order wave number $k = 1/32$ is also detected. This means that the eIBMl can generate proper pressure wave to the upstream, which is

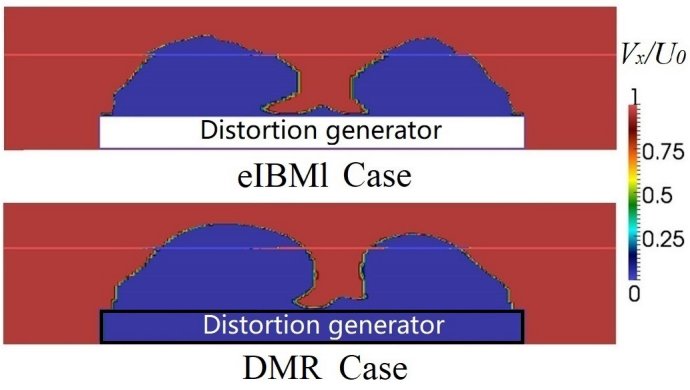

Fig. 4.8 Separation bubbles predicted by eIBMl and DMR, 65%RS and 10.6kg/s

a substantial improvement to eIBMg. Note that the magnitude for DMR is slightly higher than the one for eIBMl. The discrepancy may come from the stagnation at the blade leading edge, where the velocity is decelerated close to, but not zero by the parallel force in eIBMl. Further investigations of wave propagation using the eIBMl can be referred to Appendix A.

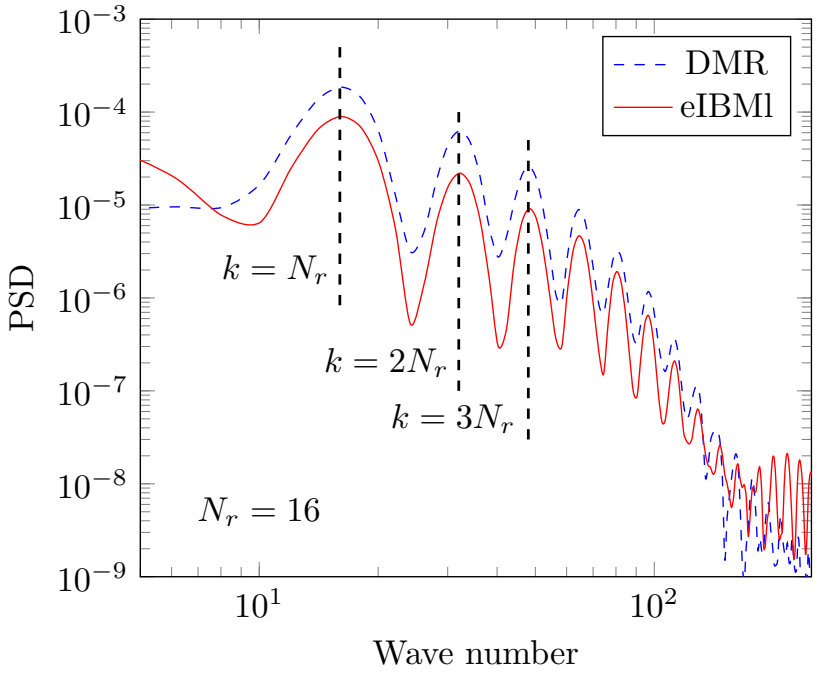

Fig. 4.9 Spectrum of the spatial frequencies

Tip clearance

In the blade tip clearance, the space near the casing is controlled by the Heaviside function (Eq.3.13). Flows within the tip clearance are illustrated in Fig. 4.10 by the axial vorticity ω_x near/within the rotor region. The data are from the eIBMl and DMR cases with 65%RS and 10.6kg/s. From Frames (a) to (c), tip leakage vortices grow and expand near the casing. Frame (c) evidently shows that the differences between the pressure surfaces and the suction surfaces are significant at the tip, indicating the direction in which the vortices grow. Hence, the method can generally reflect the influence of tip clearance.

Within Blade Region

Within the rotor blade region, the eIBMl case also demonstrates a good result in terms of the static pressure at both the blade pressure surface and the suction surface. Firstly, to compare the static pressure on the blade surfaces, the static pressure coefficient is defined by

$$C_p = \frac{p_{t0} - p}{p_{t0} - p_1}, \tag{4.2}$$

where p_1 is the average static pressure at station 1. Figure 4.11 depicts this distribution at midspan from the case with 65%RS and 10.6kg/s massflow rate. It is shown that the distributions on both surfaces predicted by eIBMl agrees with the data from DMR. Notably, at the blade leading edge on the suction side, the value from eIBMl case is much lower. This is probably because the force model does not totally stagnate the flow. Hence, the pressure peak cannot be captured by this model. This may influence the intensity of pressure wave towards the upstream and needs to be improved in the future work.

Figures 4.12 to 4.14 depict the distribution in three different radial locations extracted near the rotor blade leading edge from the case with 65% rotational speed. The pressure rises induced by the blade are generally well captured at all of the blade passages. [1] However, in Frame (a), near the casing and within the separation region, the discrepancies become greater and the eIBMl case shows a much smoother distribution. This is perhaps because, around the blade tip, the boundary layers are more sensitive to the higher Ma number. Since they are not well resolved, the velocity profiles and the static pressure may deviate further compared to the DMR case.

[1] These data are from interpolation of the pressure distribution. Hence, the pressure change between the pressure and suction surfaces across the blades should be ignored in Frame (b).

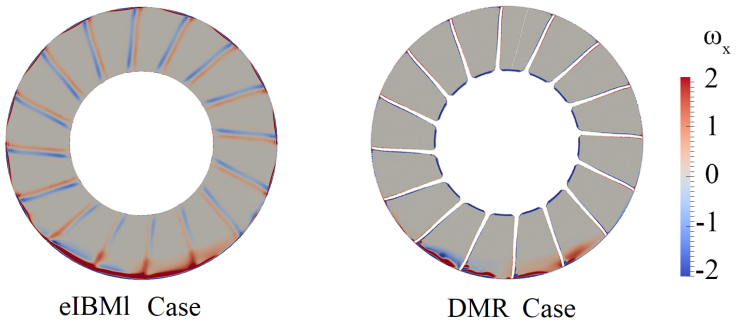

(a) Blade leading edge

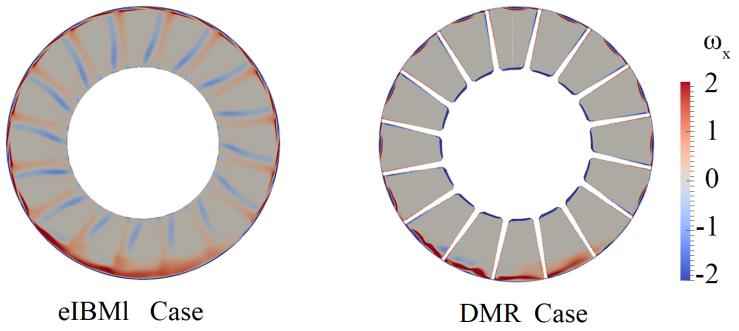

(b) Blade mid-chord

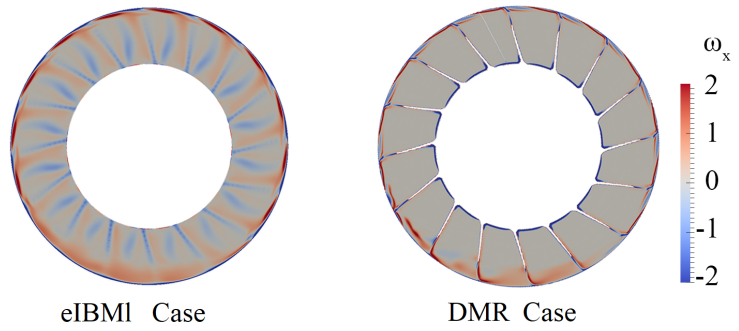

(c) Blade trailing edge

Fig. 4.10 Distribution of x-vorticity induced by blade tip clearance, non-dimensionalised by U_0/H, 65%RS and 10.6kg/s

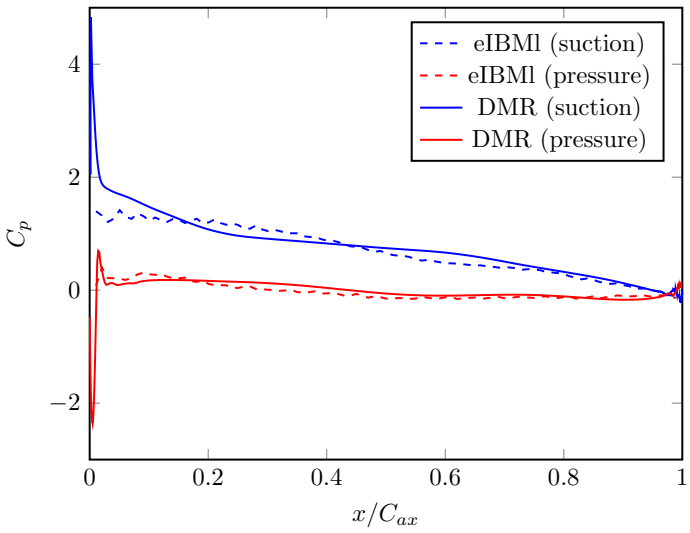

Fig. 4.11 Static pressure coefficient on blade surfaces at midspan

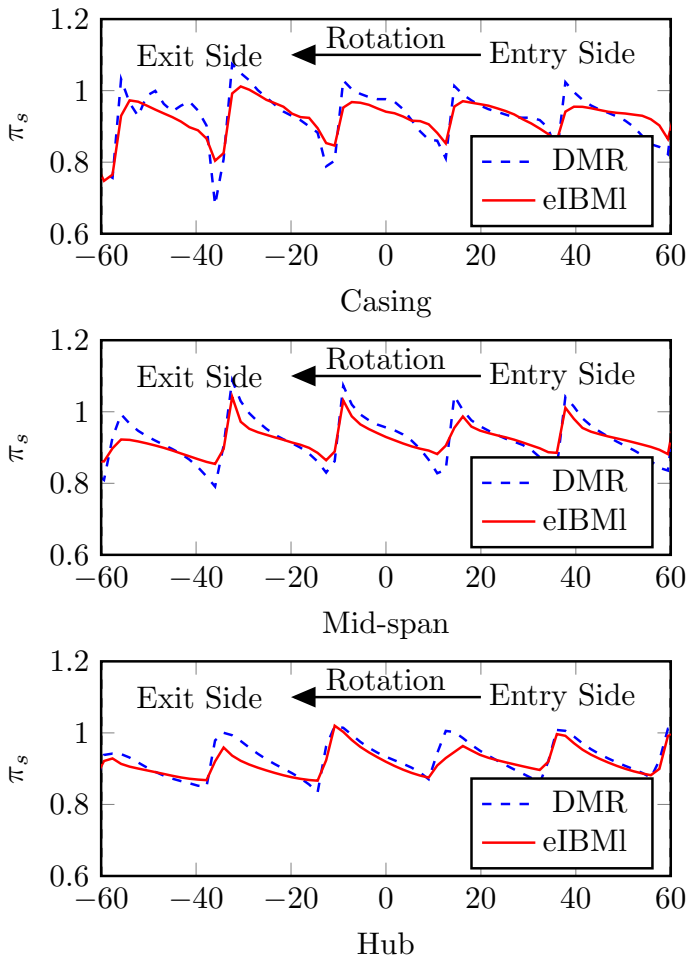

Fig. 4.12 Static pressure distribution at the blade leading edge

Similar trends can also be found at the blade mid-chord, where the discrepancies become higher towards the casing as the velocity increases. Apart from this, at the casing within the separation region, the pressure rise area is much thicker than that in the DMR case, indicating that the development of the boundary layer is underestimated. This can be improved by either advancing the loss model or refining the mesh around the blade tip, depending on the requirement in terms of flow details. At the blade

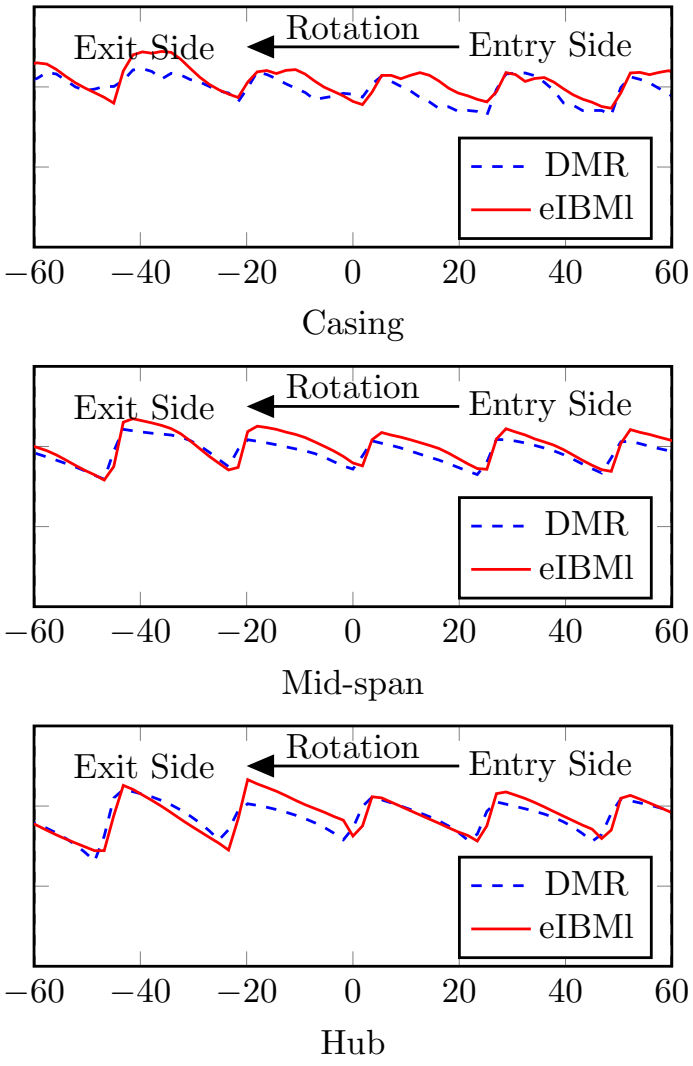

Fig. 4.13 Static pressure distribution at the blade mid-chord

trailing edge, the distributions of static pressure from both cases generally match with each other. However, it should be noted that, near the casing the intermittency is almost smeared. This is perhaps the grid are relatively coarse compared to the very

thin blade in this region. It may fail to capture the blade geometry at some points. This can be further improved by refining the mesh.

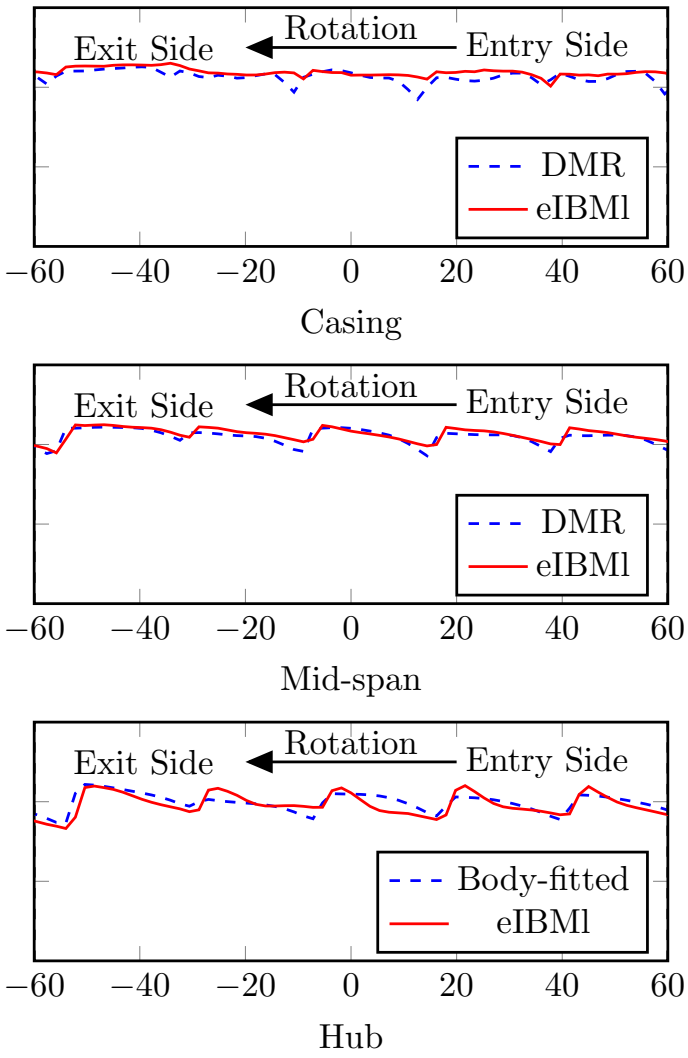

Fig. 4.14 Static pressure distribution at the blade trailing edge

Hence, we may conclude that this eIBMl can provide a proper pressure intermittency for most parts of the blade. However, special treatment may be needed to improve its performance near the tip clearance. This may include refining the mesh in this area or implementing wall models.

The flow distribution across blade passages is also compared between the DMR and eIBMl case. Predictions from eIBMg are also overlaid. Blade parallel velocity, static and total pressure are extracted from the line at three radial locations: near hub (10% blade span), midspan (50% blade span), near casing (80% blade span) at the

mid-chord shown in Fig. 4.15. The data illustrates how these quantities vary across the blade. The coordinate is rotated and H is the axis perpendicular to the blade surface, normalized by the width of blade passage d_p. Figure4.16 shows these distributions (referenced by the linear velocity V_{ref} and inlet total pressure p_{t0}). The blade region is labelled and enclosed by the black dashed line.

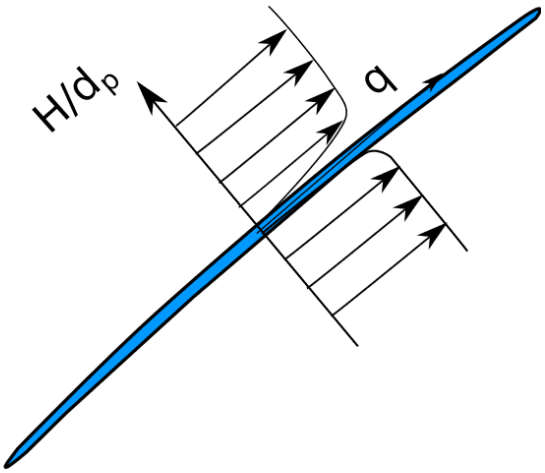

Fig. 4.15 Coordinates for profiles across blade passages

Frame (a)-(c) show these distributions at the three radial locations. It can be found that the eIBMl does not force the velocity to zero within blade region. Instead, it decelerates the flow via the parallel force to a certain value. By relaxing this strict requirement of standard IBM approach, the computational stability can be enhanced and demanding mesh requirement can be avoided. However, this leads to a penetrable blade and allows some flow deviation the flow. Hence, outside the blade region on the suction surface side ($x \geqslant 0$), the 'boundary layer' using the eIBMl model is thicker. By contrast, interestingly the static pressure distribution at all the locations agrees very well with the DMR case. It significantly improves the smeared distributions from eIBMg (green lines). The latter, however, fails to reflect flow features on the pressure and suction surfaces. The corresponding total pressure ratio in Frame (d) also shows the consistency outside the blade region, indicating a good prediction of blade work and loss. To conclude, despite the deviation of flow velocity within the blade boundary layer, the eIBMl is able to provide an accurate pressure distribution at lower computational cost and enhanced stability. This is essential for the investigation of acoustics.

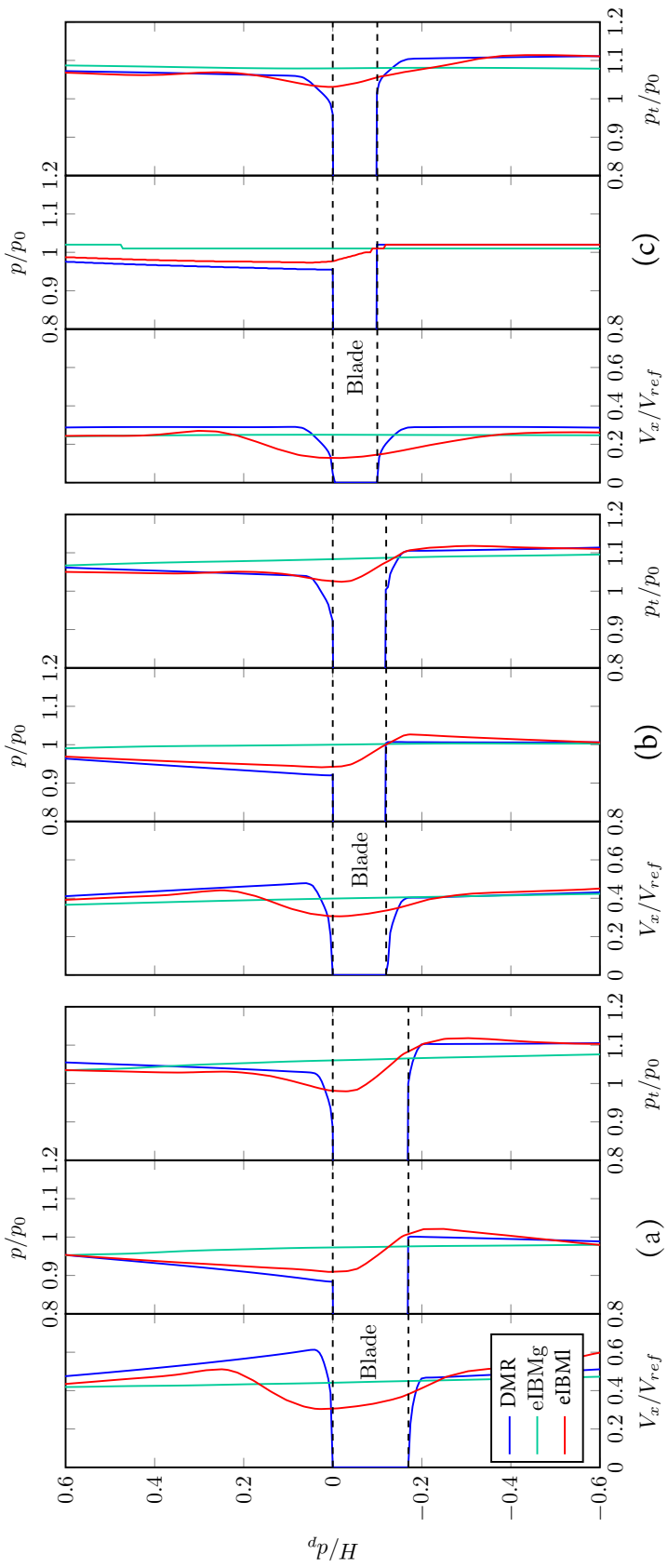

Fig. 4.16 Profiles across blade passages: (a) 10% blade span, (b) 50% blade span (c) 80% blade span, in terms of parallel velocity, static and total pressure

4.1.4 Quantitative Comparisons

The difference between the global (eIBMg) and local (eIBMl) methods obviously exists in the blade region. We choose the total pressure distributions near blade leading and trailing edges to quantitatively compare both methods against the passage data from Wartzek's experiment [168] and the DMR case, at design points with 100% and 65% rotational speed. Their circumferential distributions are extracted at three axial locations ($S_1 - S_3$ shown in Fig. 4.1 in Chapter 4), representing the rotor entry, rotor exit and stator exit respectively. The data at these three locations can provide a detailed view of the influence of the distortion on each individual component. The influence is characterised by the total pressure ratio (for radial locations) and its relative value (for axial locations). They are defined as the ratio of local total pressure to the inflow pressure,

$$\pi_{t,rel} = \frac{\pi_t}{\overline{\pi_t}}, \pi_t = \frac{p_t}{p_{t,inlet}}. \tag{4.3}$$

This offers a general view of the total pressure variation in the circumferential direction at the rotor entry and exit, as well as the stator exit.

Axial locations

Figure 4.17 illustrates the region for fan-intake interaction near the casing, where the stagnation area is formed due to the distortion generator in the upstream. Vortices are also generated by the two edges. This section analyses how the distortion or stagnation influences the downstream distributions in the rotor and stator. In Fig.4.18, the beam installation region is specified by the vertical dashed lines, marking the entry side and exit side of the rotor. In between, the rotor rotates from the right to the left. The effect of the distortion generator is evident. The total pressure ratio is lower within the region $-60° \leqslant \theta \leqslant 60°$ where the distortion generator is installed in the upstream. The loss for the case with a 100% speed is higher, indicating stronger separation. The general trends among the three numerical simulations are very similar and also match the data obtained from Wartzek's experiment[168]. The separation detected in all the cases (approximately 100°) is smaller than the 'entry-exit' labelled beam region (120°) because the low pressure downstream narrows the separation. It should be noted that the numerical predictions (all with SA model) are slightly larger than the experiment. Similar trend was also found by Liu et al. [90] in which the Spalart-Allmaras model predicts much larger separation bubbles in compressors. Hence, an innovative modification method was proposed based on helicity in order to consider turbulence energy backscatter (turbulence energy transferred from small vortices to big

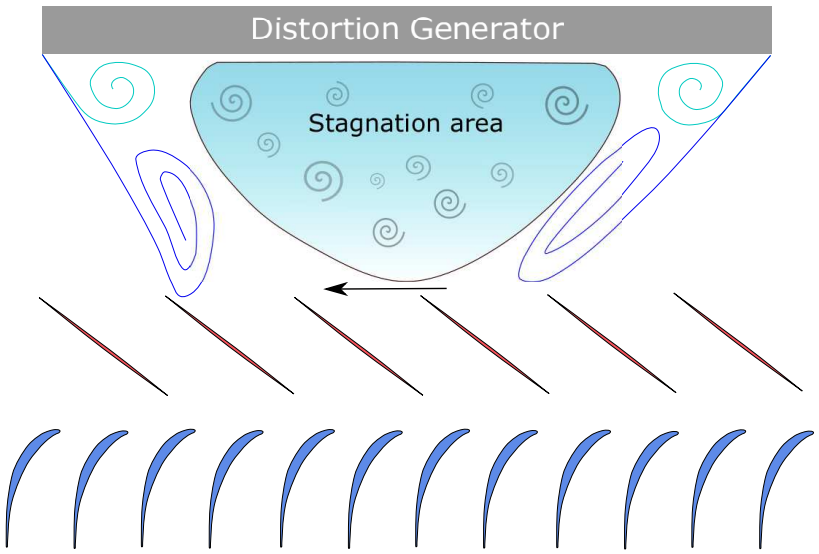

Fig. 4.17 Separation region downstream the beam

vortices), which can be substantial in the region of corner separation in compressors [90, 146]. This problem could be tackled by either this model or LES in the future. In addition, interestingly, the experiment shows a W-shape in the centre that seems to be due to the corner vortices and the separation line shear layer on the two sides of the beam [167] (Figure 4.17). These vortices increase the total pressure loss at the edges of the separation region, but in the centre, the loss remains at the original level. However, this is not obvious in all of the present numerical simulations for both cases. This is perhaps due to the fact that eddy viscosity models are not able to model such strong separation [90, 146].

Figure 4.19 shows the distribution at the rotor outlet. Compared to the experiment and the DMR case, the cases with modelled blades (both eIBMl and eIBMg) can successfully capture the distortion transport and its displacement towards the entry side. The asymmetry of the total pressure distribution, the value at the exit side is higher than that at the entry side, is also well predicted. Hence, it can be concluded that both geometry modelling methods can accurately represent distortion transport. However, it should be noted that the eIBMg case shows some discrepancy at 100% speed within the distortion region. This may be due to the assumption of an infinite number of blades in the circumferential direction, which overestimates the pressure loss especially when the mass flow rate or flow velocity is high.

At the stator outlet (Fig.4.20), both the eIBMg and eIBMl cases can accurately reflect the transport of the distortion across the stator. However, as expected, the eIBMg case completely smears the wakes generated by the blades, whereas the eIBMl

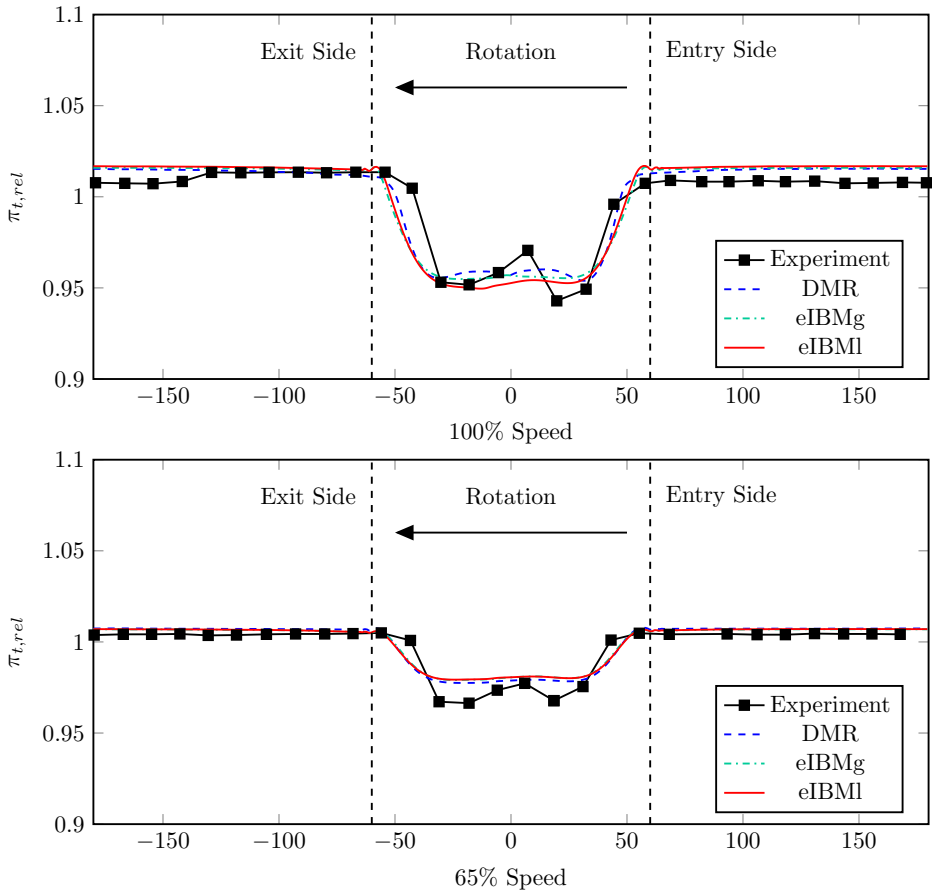

Fig. 4.18 Total pressure distribution at the rotor inlet

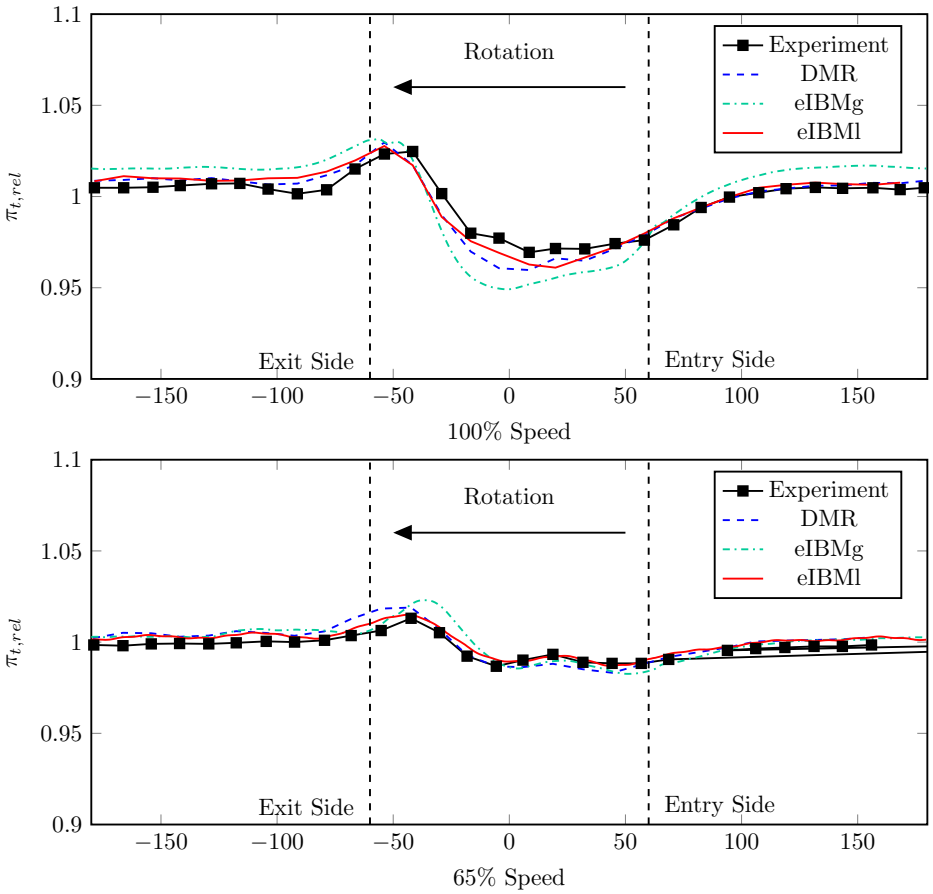

Fig. 4.19 Total pressure distribution at the rotor outlet

case is able to capture this feature. Compared to the DMR case, the eIBMl case still suffers from slight deviations in its magnitude, but this could be further resolved by refining the loss model.

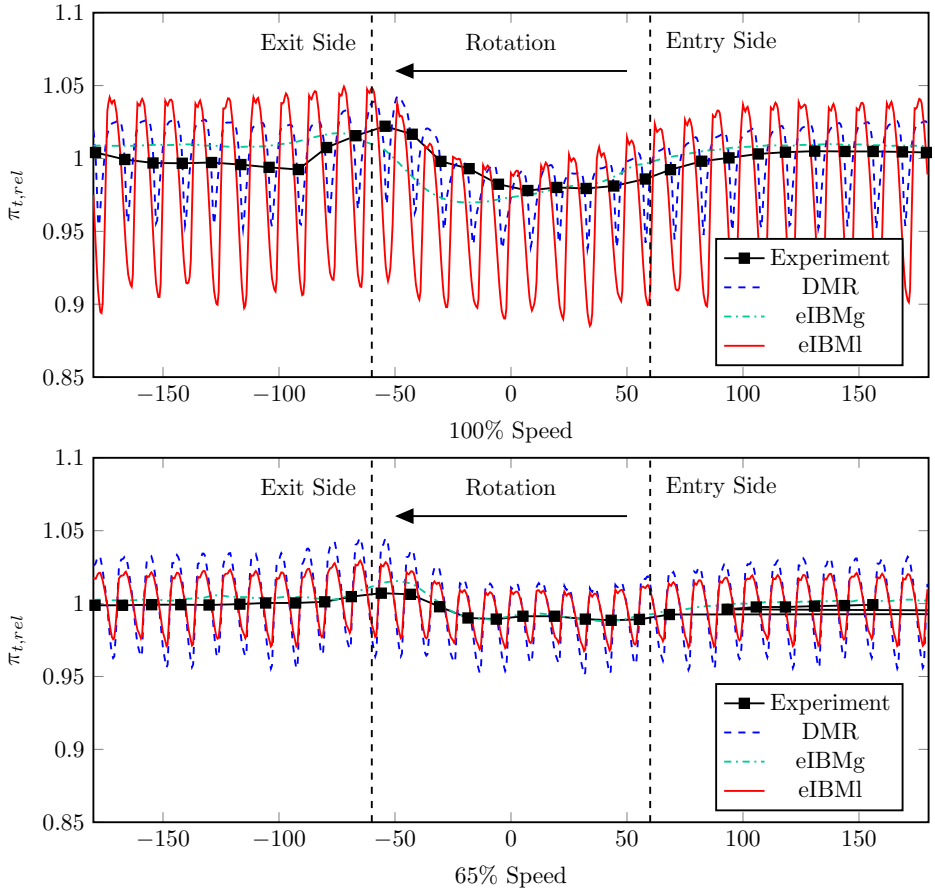

Fig. 4.20 Total pressure distribution at the stator outlet

Radial locations

In the radial direction, the data are obtained at 10%, 50%, and 90% of the stator exit, corresponding to the hub, midspan, and shroud locations, shown in Figs.4.21-4.23 respectively. At the hub (Fig.4.21), the eIBMl case shows a reasonable distribution in terms of the magnitude and phase for both speeds. Both the distortion transport and blade wakes are well captured, despite a small reduction in the magnitude within the separation region. It should be noted that the experiment generally captures the maximum at all of the circumferential locations; in contrast, the eIBMg seemingly averages the data within and outside of the blade wakes.

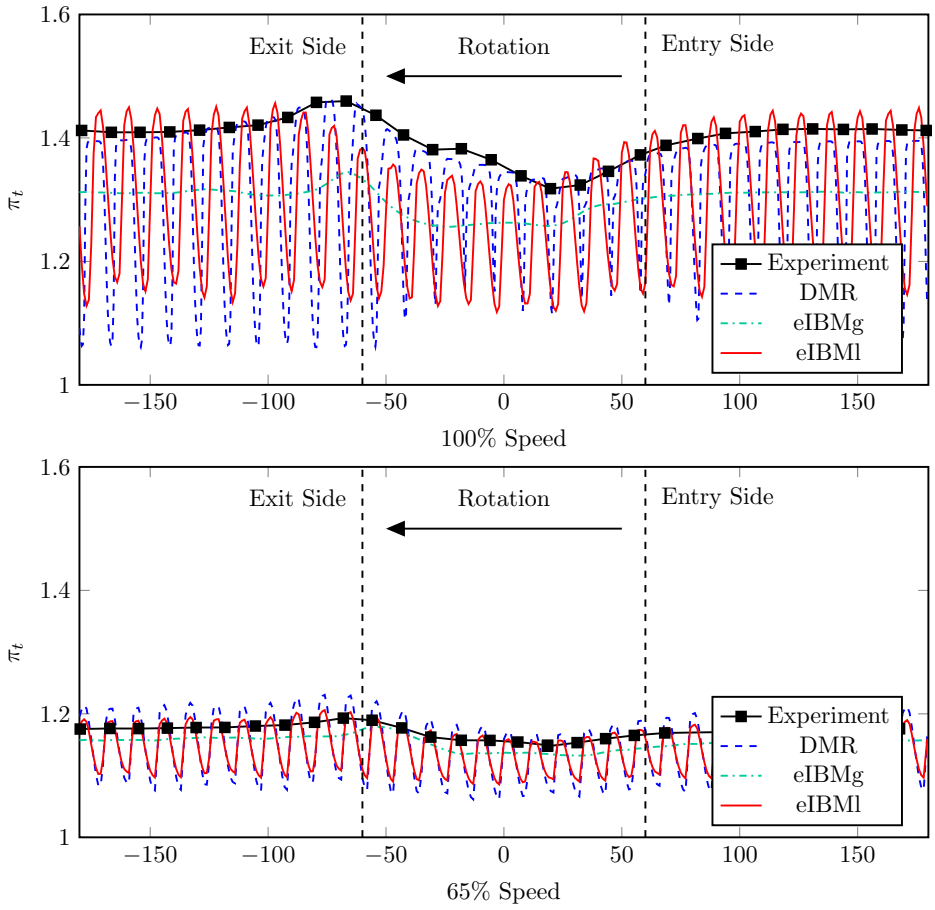

Fig. 4.21 Total pressure distribution at the hub of the stator outlet

At the midspan, the predictions from both eIBMg and eIBMl are much better and the wake loss is lower. The results are almost identical for the 65% speed case. This implies that the main flow features, including the distortion and wake loss, could be well captured by all the methods. Near the casing (Fig. 4.23) because the blade is the

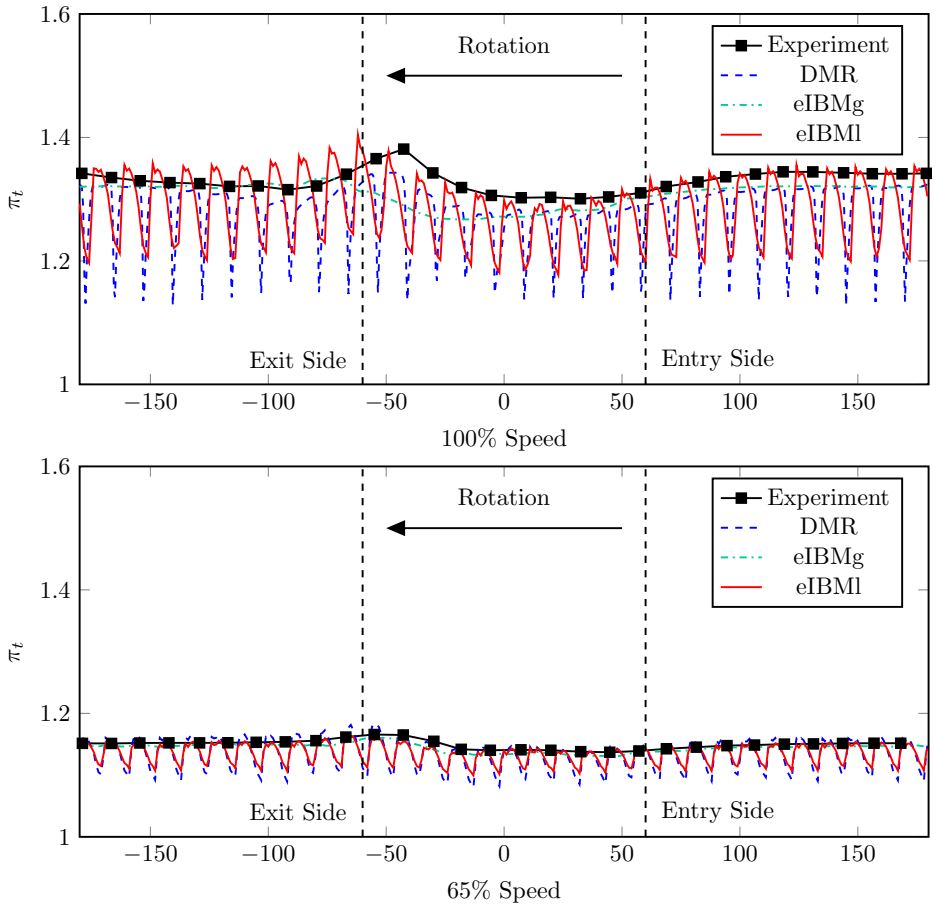

Fig. 4.22 Total pressure distribution at the midspan of the stator outlet

thinnest there, the blockage from the blades is at its minimum and the flow estimated by eIBMg is closest to the cases with finite blades. These comparisons demonstrate that the eIBMl case can accurately predict both the distortion transport and blade wakes, whereas the eIBMg can roughly reflect the distribution of the distortion but smears the wakes.

Further applications of eIBMl in modelling pressure waves and detecting noise can be referred to the Appendix 1. This could be a substantial improvement compared to eIBMg.

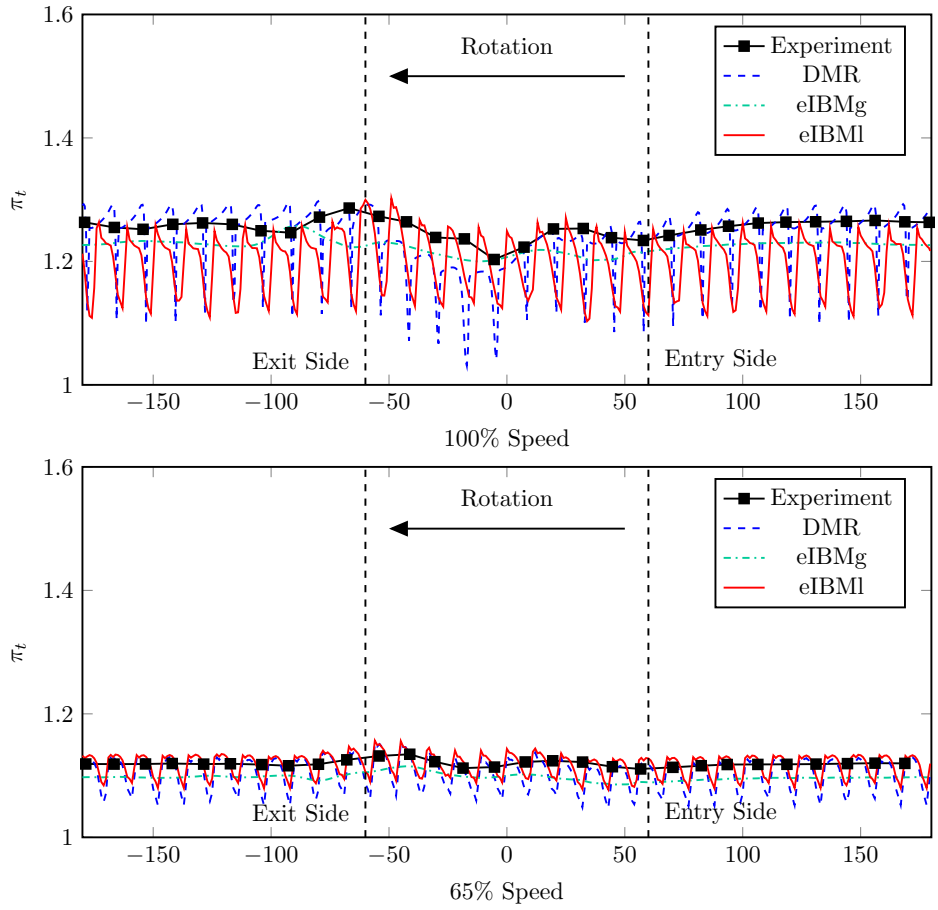

Fig. 4.23 Total pressure distribution at the shroud of the stator outlet

Rotational speed	16043 rpm
Diameter	0.51m
Pressure ratio	1.63
Efficiency	92 %
Mass flow rate	33.25kg/s
Mach number at rotor tip	1.4
Rotor blades	22
Stator blades	34

Table 4.2 Main design characteristic parameters of NASA Rotor 67

4.2 NASA Rotor 67

4.2.1 Case Framework

The second test case is on the NASA Rotor 67. It is a transonic fan stage consists of a rotor with 22 blades and a stator with 34 blades. More technical details can be found in Table 4.2. In this validation, the rotor is run at 90% speed with a 120° low-total pressure (89% standard pressure p_{t0}) distortion region at the inlet. The corresponding mass flow rate is 32kg/s and the total pressure ratio is 1.46. The mesh size is 12.9M and uses the orthogonal grid. In contrast, Fidalgo [47] conducted the same simulation but with a body-fitted mesh of 42.5M grid points. The numerical simulation is conducted by using URANS with the SA model with eIBMl blades. As the aim of this research is to validate the effectiveness of eIBMl for providing a boundary condition for the upstream/downstream, boundary layers around blade are not properly resolved.

Figure 4.24 shows the sketch of the computational domain and the boundary conditions. Both rotor and stator are modelled by eIBMl. The inlet applies total pressure p_{t0} and outlet uses the static pressure with a radial equilibrium condition. These settings are similar to the one used for the Darmstadt Rotor. The case is run from an initial solution obtained by a steady RANS solution with eIBMg. It uses a 240 CPUs cluster for two weeks, corresponding to around 20 rotor revolutions.

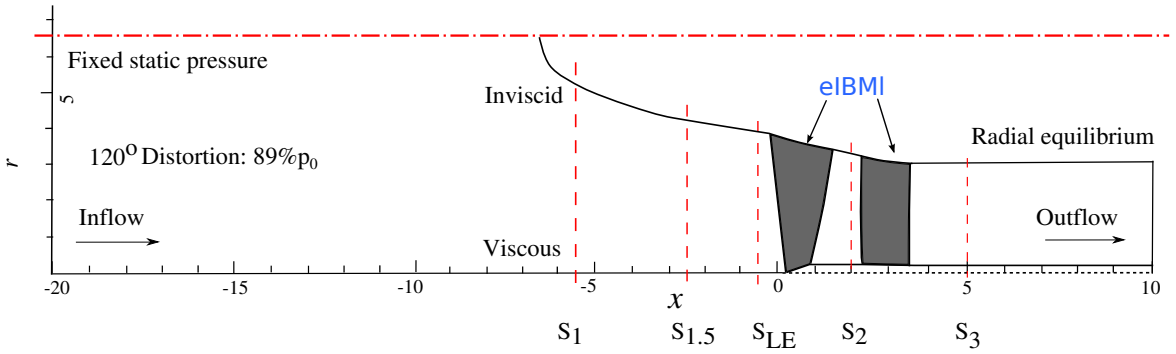

Fig. 4.24 Sketch of the numerical framework for NASA Rotor 67

4.2.2 Flow Features

This section discusses the results obtained from the case of NASA Rotor 67 using eIBMl. Figure 4.25 depicts the contour of total pressure ratio in an expanded $x-\theta$ plain at mid-span. The black solid lines identify the extent of the distortion region at inlet. This figure indicates how the distortion is convected downstream and in the fan rotational direction, where a slight shift is shown. Figure 4.26 compares the data from

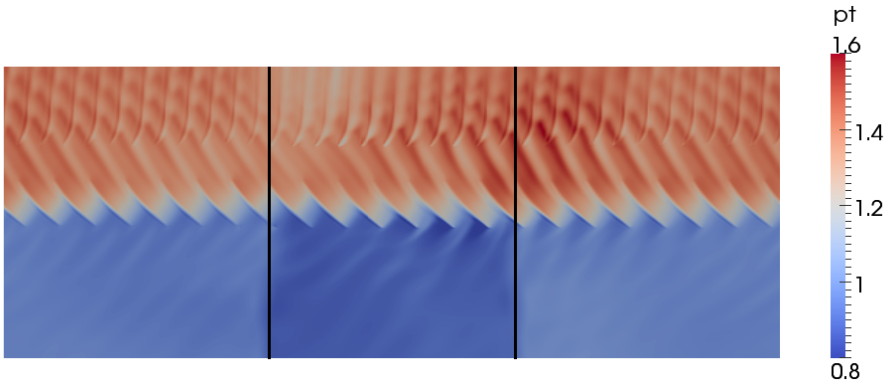

Fig. 4.25 Distribution of total pressure ratio at the mid-span plane, snapshot

the time average solution of the present case with the one from Fidalgo's [47] research. They are the static pressure distribution and mass flux in the upstream of the rotor at three axial locations: $x/C_{ax} = -0.5, -2.5, -5.5$ (C_{ax} is the blade axial chord). These locations are Plane $S_1/S_{1.5}/S_{LE}$ shown in Fig. 4.24 respectively. In general, the results given by the eIBMl rotor agree well with Fidalgo's data from a body-fitted mesh. It captures the distortion patterns in the circumferential direction and also reflects the trend of its transfer. When the distortion approaches the fan face, it accelerates the flow and hence the mass flux increases. As the total pressure does not increase in this region, the static pressure drops.

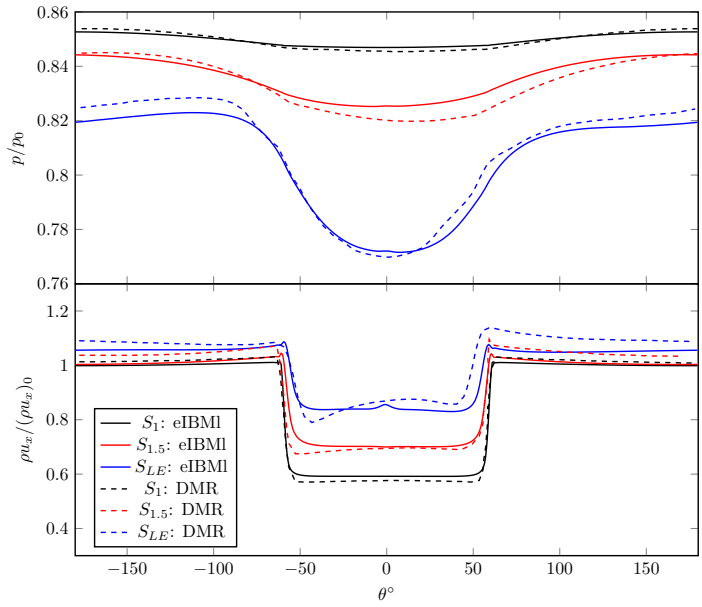

Fig. 4.26 Time-averaged, circumferential distributions of (a) static pressure (b) mass flux at three axial locations upstream of the rotor

The behaviour of the modelled rotor can be further revealed in the distortion patterns at Plain S_{LE} and S_2, shown in Fig. 4.27. In Frame (a) the contour of mass flux shows the distortion region and this leads to the co-swirl zone at the rotor exit side (coloured in orange) and counter-swirl zone at the entry side (in blue) in the contour of whirl angle. There are two factors that influence the blade work: mass flow rate and incidence (whirl angle). As the low mass flow rate within the distortion leads to a higher total pressure ratio for a single blade, the total temperature in this region is higher than the rest part shown in the right figure of Frame (b). On the other hand, the counter-swirl also creates a larger incidence at the entry side compared to the exit side. Hence, the total pressure ratio and total temperature are also higher at the entry shown in Frame (b). Consequently, both effects make the total temperature at the entry side the highest. This indicates that the eIBMl rotor is able to capture the main features of distortion transfer.

At the rotor outlet S_2 and stator outlet S_3, the total pressure and temperature ratios π_t and τ_t are extracted and quantitatively compared in Fig. 4.28. The data are area-weighted averages at midspan from a time-averaged solution. The results from eIBMl case are very close to the DMR case from Fidalgo's simulation, except for some deviations at rotor entry side $\theta = 60°$. In Frame (a), the distributions for total temperature ratio are almost identical, marginal deviations are observed in the total pressure ratio. This deviation is attributed to the loss model, which has a linear

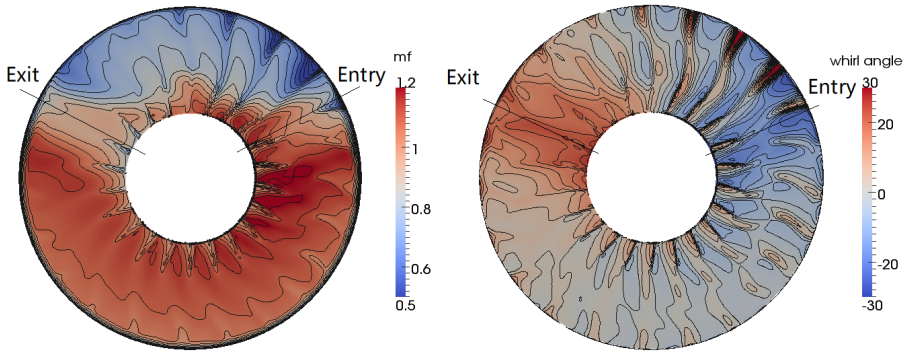

(a) Rotor inlet: Plane S_{LE}. Left: mass flux, right: whirl angle

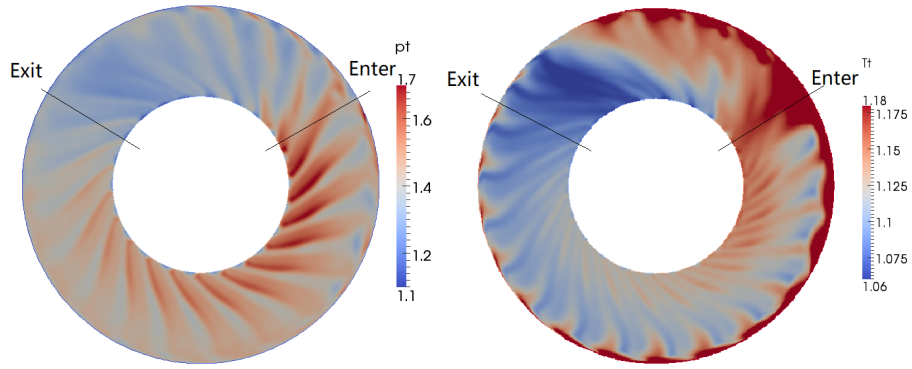

(b) Rotor outlet: Plane S_2. Left: total pressure ratio, right: total temperature ratio

Fig. 4.27 Distributions of quantities at (a) rotor outlet and (b) stator outlet

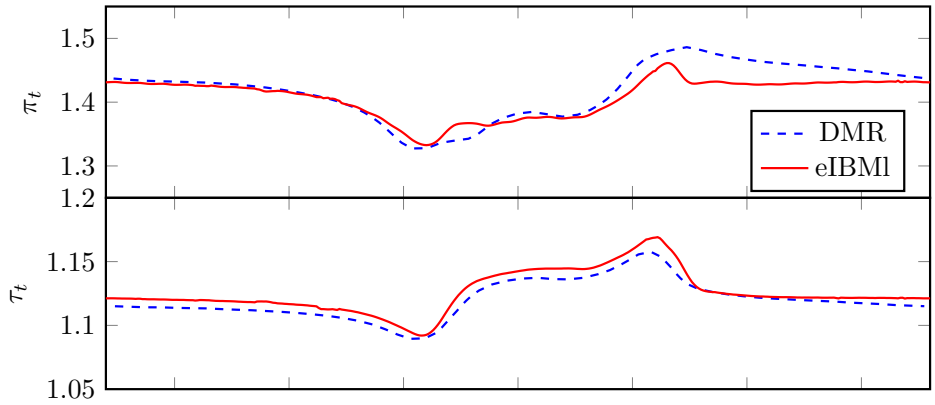

(a) Rotor outlet

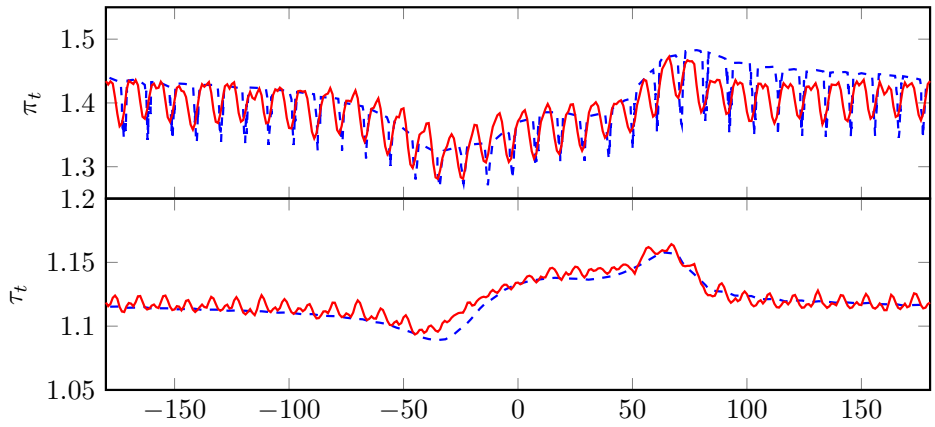

(a) Stator outlet

Fig. 4.28 Circumferential distributions of total pressure ratio π_t and total temperature ratio τ_t at (a) rotor outlet (b) stator outlet

relation with velocity square. When the velocity is deviated due to the distortion, the loss can be thus inaccurate. In Frame (b), the intermittency induced by blade wakes can be seen. As stated in the previous section, this is a substantial improvement compared to eIBMg. For the total temperature distribution, the intermittency is more intensive in the modelled case because the blade wakes from the modelled blades are thicker. This defect could be addressed by incorporating much more accurate wake models in the future.

Hence, these results, as well as the data from the previous Darmstadt rotor, can demonstrate that the model is able to predict the internal flows under a range of circumstances: different rotational speed (65%/100%), axial and radial locations, compressor configurations (NASA/Darmstadt rotor).

4.3 Triangular Prism

The IBM for a range of studies of 2D flows around rigid or elastic bodies [11, 23, 57] has been tested and showed a good agreement in main flow variables with analytical solutions and experiments. Applications for turbulent flows at high Reynolds numbers were also validated by Iaccarino et al. [72]. However, the validation using IBM with eddy resolving methods is still rare. In this section, high-fidelity turbulence modelling with the IBM is tested on the flow around a triangular prism with an apex angle of 60° shown in Fig.4.29. This flow has been studied by Agrwal [4], who used Particle Image Velocimetry (PIV), hotwire anemometry and flow visualisation techniques to measure the velocity field. Likewise, we conducted a numerical study for the same test but used the Large Eddy Simulation (LES) method with an IBM to model the triangular prism.

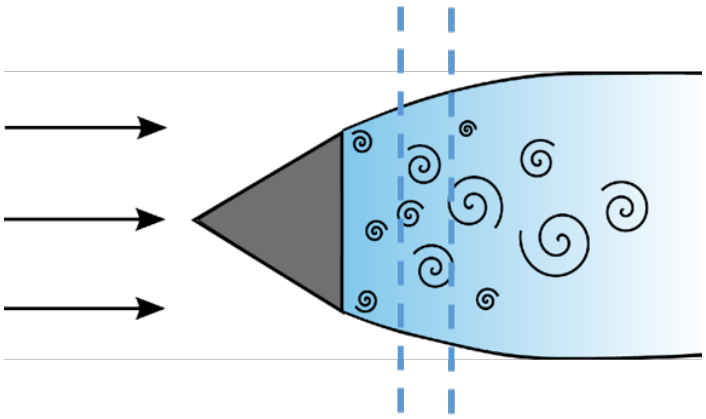

Fig. 4.29 Sketch of flows around a triangular prism

4.3.1 Case Framework

The prism for the experiment has an equilateral triangular cross-section, with sides of length D=6 mm and a length of $6D$ in the spanwise direction. In the simulation, it is a 3D geometry with periodic boundary conditions imposed on both sides. The inlet velocity is around 1 m/s, and the Reynolds number is set to 520. For the present numerical simulation, as the code is designed for the compressible flow, the flow Mach number should be much higher. Hence, the test case is scaled down by 150:1, adjusted to $Ma = 0.35$, so that the same Reynolds number is guaranteed as the experiment. The computational region is extended to $10D$ in the streamwise and pitchwise directions, with 150 grid points for each. In the spanwise direction, 100 grid points are allocated.

In total, around 2.25 million cells are deployed in the computational domain. Two calculations have been performed, one with an IBM modelled prism and the other with a mesh resolved prism. Implicit LES is used for both cases. Around 20 flow-throughs are used to collect the mean flow and statistics). The distributions of axial velocity, turbulence intensity and TKE production are compared. These quantities are normalised by the inlet velocity U_0, U_0^2 and U_0^3/D respectively.

4.3.2 Flow Features and Turbulence

Figure 4.30 shows the axial velocity profiles extracted at locations $x = 1D$ and $x = 2D$. The experimental results erroneously show a certain degree of asymmetry while the numerical results are much more symmetric. Although these marginal deviations in the regions of high shear are observable, the predictions are largely in line with the experiments. Second-order statistics of turbulence intensity were spanwise averaged and their contours are shown in Fig. 4.31. The contours in Frame (a) are from the experiment and present slight tortuosities presumably due to its sampling frequency. By contrast, both the DMR (Frame (a)) and IBM (Frame (b)) cases show smoother contours but the same locations for the maximum and values at 0.08 and 0.38.

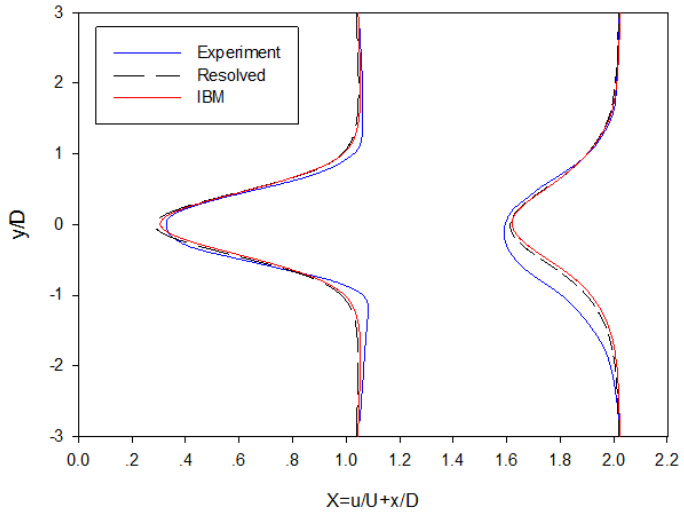

Fig. 4.30 Distribution of axial velocity at $x = 1Dand2D$

Figure 4.32 depicts TKE production, which also indicates the value of velocity gradients. It can be seen that the profiles at $x = 2D, 3D, 4D$ for the IBM case are in favourable agreement with those from the DMR case. These results indicate that this IBM framework can replace the rigid boundaries of the prism for collecting second-order statistics.

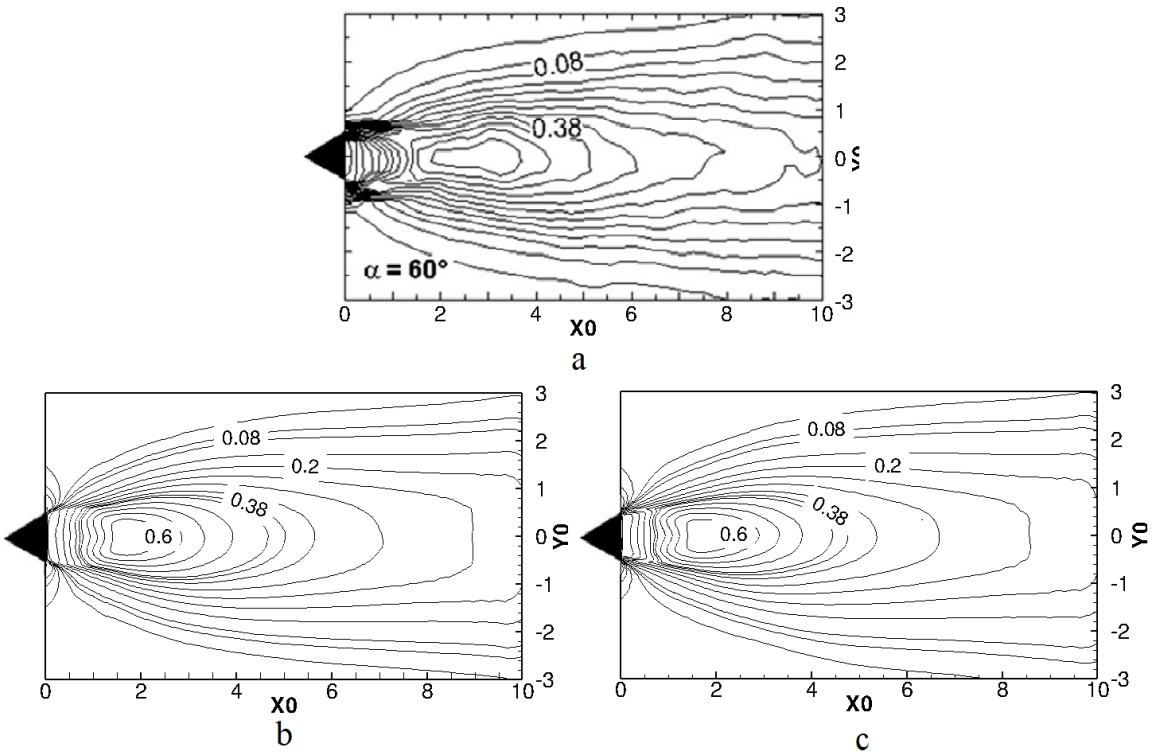

Fig. 4.31 Contours of turbulence intensity: a. experiment[4], b. DMR case, c. IBM case

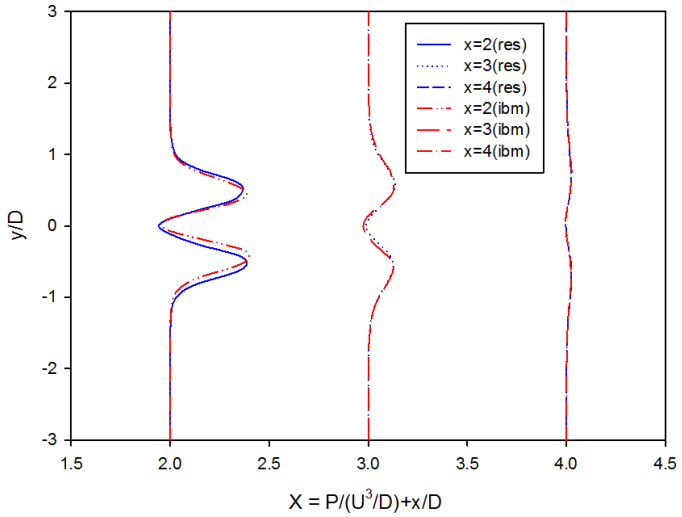

Fig. 4.32 Distribution of TKE Production at x=2D,3D,4D

4.4 Concluding Remarks

This chapter validated RANS+eIBMg, URANS+eIBMl for reproducing boundary conditions for the upstream and downstream potential flows and the LES+IBM for turbulence. Comparisons against the experiment and URANS+DMR case indicate that the the total pressure distributions predicted by eIBM agree well with the experimental data at the rotor inlet, exit and stator exit. Due to the assumption of an infinite number of blades, the eIBMg removes the blade wakes at trailing edge. Despite this, the general trend of the distortion development in the axial direction can be captured and the true total pressure ratio can be approximated. By contrast, the eIBMl is able to include more realistic blade effects for the upstream with relatively lower costs. The mesh size is only 20% of the original one. This method can approximate the main flow features in terms of static/total pressure, Mach number, separation, wave propagation and tip leakage. The validation of the IBM on a triangular prism also show that the IBM with LES is able to model high-order statistics. Hence, this method can be used to replace the resolved distortion generator and to investigate the influence of the fan on the distortion. With the validated methods, further investigations regarding the mechanism of fan-intake interaction and relevant parametric studies are conducted in the following chapters.

Chapter 5

Mechanisms of Fan Influence

To understand how a fan interacts with a separation from the upstream, the eIBM with LES mentioned in the previous chapter is applied to analyse second order statistics and investigate the process of this interaction. We focus on fan influence as a whole in the axial and radial directions, whereas the circumferential flow details in blade passages are neglected. Accordingly, the eIBMg is applied to the fan for reducing costs.

5.1 Case Framework

The simulation was conducted on a 30° sector motivated by experimental studies on the Darmstadt Rotor [87, 114, 156, 16, 168], with and without a fan. In these studies, the distortion generators were designed to approximate the flow conditions in a real engine within the laboratory. Measurements by Lieser [87] and Bitter [16] showed that the compressor performance is highly sensitive to the distortions encountered at the tip. Hence, a periodic distortion generator is placed upstream of the tip of the fan in order to reproduce the distortion encountered over an intake lip at a high angle of attack. Figure 5.1 illustrates the computational domain and boundary conditions.

5.1.1 Computational Settings

The test case employs the original duct and the rotating fan from Bitter's test rig set-up [16, 168], with a periodic beam installed upstream of the fan. To reduce the computation cost, we ignore the circumferential influence and extract a 30° sector duct with a beam height of $H = 0.02$m and length $1.5H$ placed at an axial distance of $12.5H$ from the inlet. The fan is positioned at an axial distance of $5.25H$ from the beam. Note that all of the spatial quantities mentioned in the following sections are

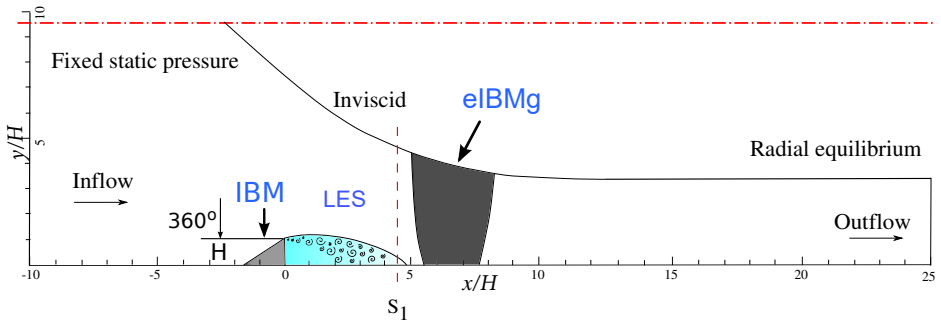

Fig. 5.1 Experiment settings for the 30° sector case

non-dimensionalised by the beam height H. The velocity is normalised by the velocity, u_∞, which corresponds to the outer edge velocity of the separated shear layer measured at the maximum height of the beam (Fig.5.1). The Reynolds number is defined based on H and u_∞, $Re = \rho u_\infty H/\mu$, yielding $Re \approx 1.6 \times 10^5$.

The primary objective of the current study is to capture the distortion generated on the lower wall (casing). Hence, an inviscid boundary condition is imposed on the upper wall, which ensures that the pressure distribution due to the spinner is well represented at a reduced computational cost. International Standard Metric Conditions (P_0=101325 Pa and T_0=288.15 K) at sea level are applied at the inflow. The flow has also been tripped at an axial location of $x = -6H$ in order to ensure that a turbulent boundary layer develops upstream of the distortion generator. The mass flow rate is fixed at 10.6 kg/s for both the case with and without a fan, corresponding to the peak efficiency point at 65% of the rotational speed (1361.31 rad/s). A radial equilibrium boundary condition is imposed at the outflow for the test case in which the effect of fan is considered. In contrast to the full annulus considered in the experimental campaign on the Darmstadt rotor, we consider a 30° sector in the current numerical study. This extent is chosen because it corresponds to $5H$ at the casing, and sufficient to ensure that the structures are decorrelated in the circumferential direction, according to Tucker [152]. Figure 5.3b also demonstrates this decorrelation. Hence, periodicity can be applied and imposed on the two sides.

5.1.2 Geometry simplification

This section demonstrates that the periodic distortion generator in this simplified case would not significantly affect the axial and radial distribution of the separation and hence it has the very similar results to the full-annulus case. This is achieved by setting two cases with a 360° beam and a 120° beam respectively and then running the case

by RANS. In Fig. 5.2, the separation bubble is identified by inflectional points of the

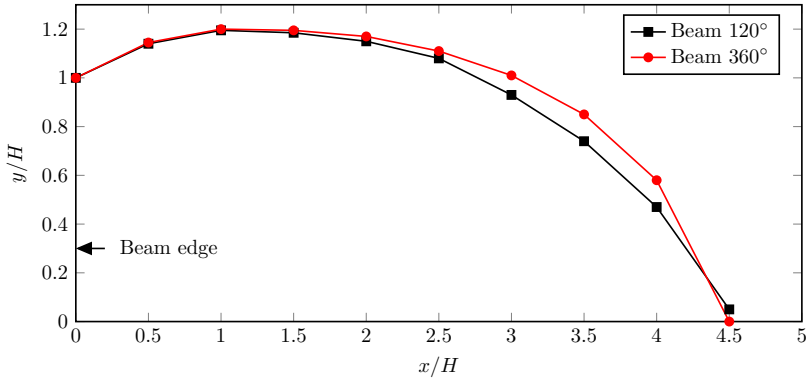

Fig. 5.2 Inflectional points of the separation bubble

velocity. The height in the rear ($2H \leqslant x \leqslant 4.5H$) of the separation bubble for the 360° beam is higher than that for the 120° beam. However, the separation lengths are almost the same. This means that the symmetry only thickens the bubble. According to this feature, we may conclude that a symmetric beam (i.e. a 360° beam) can replace an asymmetric one in a meaningful way. In addition, although the bubble height may be not representable, the variation trend of the bubble height under different circumstances can still be investigated as long as the same original condition is referenced.

5.1.3 Mesh quality

This section examines the effect of mesh on intake distortions. Two types of mesh were tested for grid independence: the coarse one with 8.6 million nodes, and the fine one with 60 million, shown in Table 5.1. Streamwise, pitchwise and spanwise distributions of the nodes in the region of interest (beam, recirculation zone and fan) are also tabulated. For the fine mesh, the grid resolution is within the wall units of $\Delta x^+ = 50 \sim 130$, $\Delta y^+ = 1$ and $\Delta z^+ = 15 \sim 30$, which are the wall spacing requirements recommended by Tucker [149]).

First, we examine the quality of the fine mesh. Following You [181], the grid resolution within the shear layer downstream of the beam is estimated in Kolmogorov units as follows:

$$R = \frac{V^{1/3}}{\eta}, \eta = \left(\frac{\nu^3}{\varepsilon}\right)^{1/4}. \tag{5.1}$$

Here V is the cell volume and η is the Kolmogorov length scale. The dissipation in the above equation is approximated by $\varepsilon = \mathcal{P} - \mathcal{C}$, where $\mathcal{P}$ and $\mathcal{C}$ are the production and convection of turbulent kinetic energy, respectively. Figure 5.3a shows the distribution

Table 5.1 Grid distribution

Grid size	Δx^+	Δy^+	Δz^+	Number of nodes
Fine mesh	75	1	30	59,371,200
Coarse mesh	150	1	100	8,600,100
Region nodes	streamwise	pitchwise	spanwise	Total nodes
Beam	60	100	400	2,400,000
Recirculation	250	150	400	15,000,000
Fan	120	193	400	9,264,200
Total	776	193	400	59,371,200

of the ratio R in the recirculation zone. The values of R are within a value of 50, which meet the resolution requirement proposed by You [181], except for a very small area at the beginning of shear layer, which does not affect the main area of the simulation. Figure 5.3b also shows the auto-correlation of u' at three different points (marked in Fig. 5.3a). The auto-correlation vanishes to zero at 30°, indicating that a spanwise extent of 30° is sufficient to accommodate all of the modes along the span.

In order to estimate the sensitivity of the findings to the grid resolution, studies are also carried out on a coarser mesh which consists of ≈ 9 M ($\times 10^6$) mesh nodes. Figure 5.4 shows the distributions of the mass flow rate and pressure at $x = 4.5H$ for the case with the fan. Consistent results are observed on both the grids, thereby demonstrating that the results presented here are mesh independent.

5.2 Flow Features

5.2.1 Instantaneous Flow Field

We start the analysis from instantaneous flow solution obtained from the fine mesh. Figure 5.5 qualitatively shows the contours of the stagnation pressure. It demonstrates both the distortion generated in the lee of the beam and an increase in the stagnation pressure due the presence of the fan. The iso-surfaces of Q-criterion (Q=40) in different views are illustrated in Fig. 5.6a and 5.6b, coloured with the local axial velocity ($v_x = -150 \sim 200$). The axial location of the fan is also shown by means of a sketch. A coherent two-dimensional detached shear layer forms at the edge of the beam, which rapidly destabilises downstream. A decrease in scale of the recirculation region is

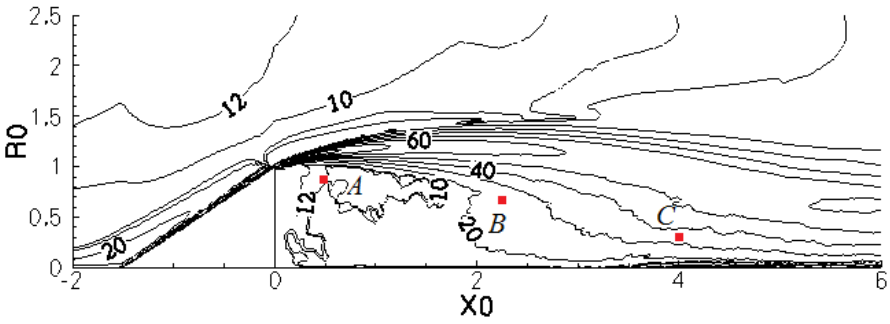

(a) Resolution in Komogorov units (η)

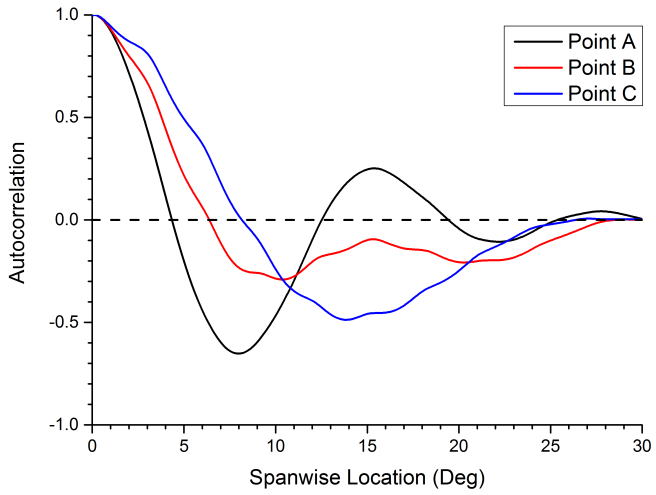

(b) Auto-correlations for Point A/B/C

Fig. 5.3 Mesh quality

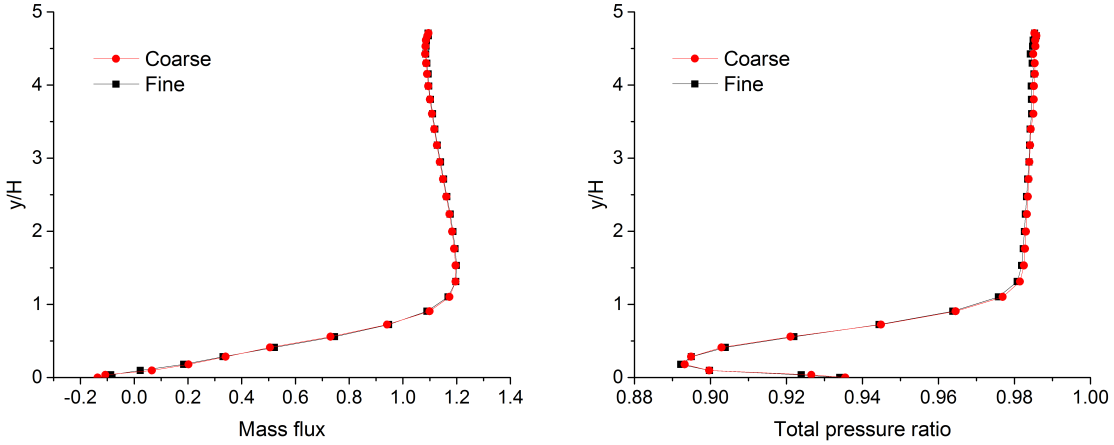

(a) Mass flux distribution (b) Total pressure distribution

Fig. 5.4 Flow distribution of LES cases with different grid size at $x = 4.5H$(time averaged, with fan)

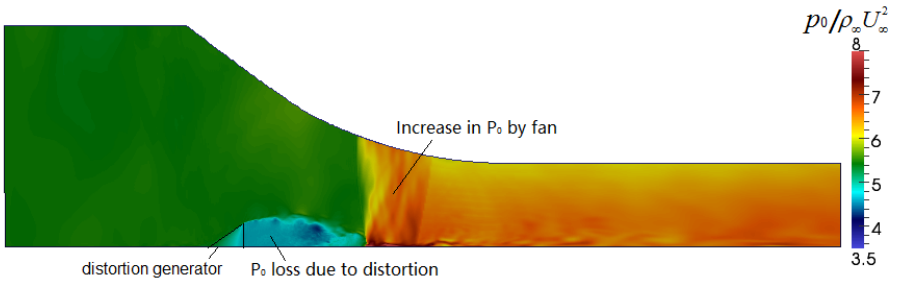

Fig. 5.5 Total pressure distribution of the instantaneous flow

clearly evident in the presence of the fan. Qualitatively, in the subfigure (located in the top-left corner) in Fig. 5.6b, an increase in the length scales of the turbulent structures due to the fan is notable. Quantitative estimates of the change in the lengths scales can be obtained from the two-point correlations. This requires saving long time-series data which is, however, beyond the scope of the current work.

5.2.2 Time-averaged Flow Field

Time integration is carried out using an explicit 5-stage Runge–Kutta time-stepping scheme [101]. After flushing out the initial transient, time averaging (running average) of the primitive variables and high-order statistics (Reynolds stresses) has been carried out for around $150H/U_\infty$ time units. The maximum deviation of $\langle u'u' \rangle$ is less than 1%, when the flow field is further averaged for $50H/U_\infty$ time units, indicating that the convergence is acceptable. Figure 5.7 compares the axial mean velocity profiles at different streamwise locations on a carpet plot. A line joining the locus of inflectional points of the velocity profiles is also overlaid on this plot. As noted from the instantaneous flow, the extent of the recirculation zone has significantly reduced due to the fan. The flow reattaches at an axial location which is more than a beam height upstream of the fan leading edge. This means the fan can suppress the distortion much earlier before it enters the fan blade passages.

5.3 Turbulence Statistics

The previous section showed that the fan substantially changes the streamline curvature and hence suppresses the separation bubble. This section investigates how this effect on the main flow influences the turbulence statistics. This helps understand the mechanism by which the fan reduces the scale of the recirculation region. To analyse this process,

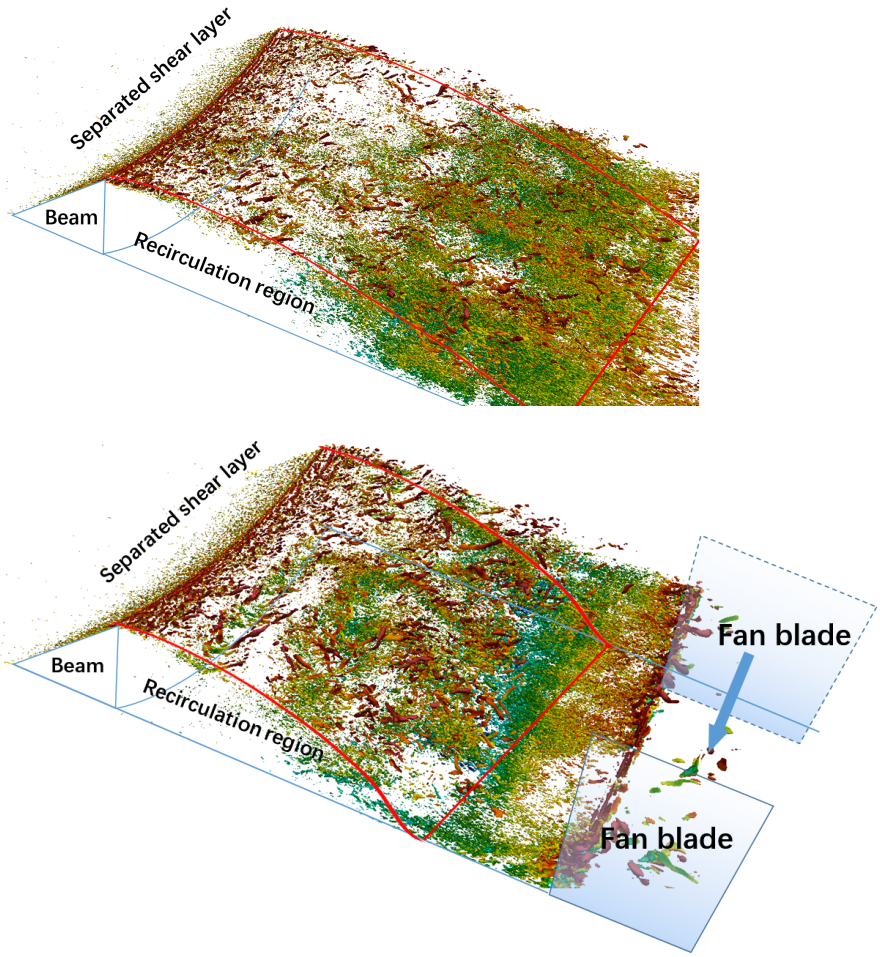

(a) Instantaneous flow for the cases without/with fan

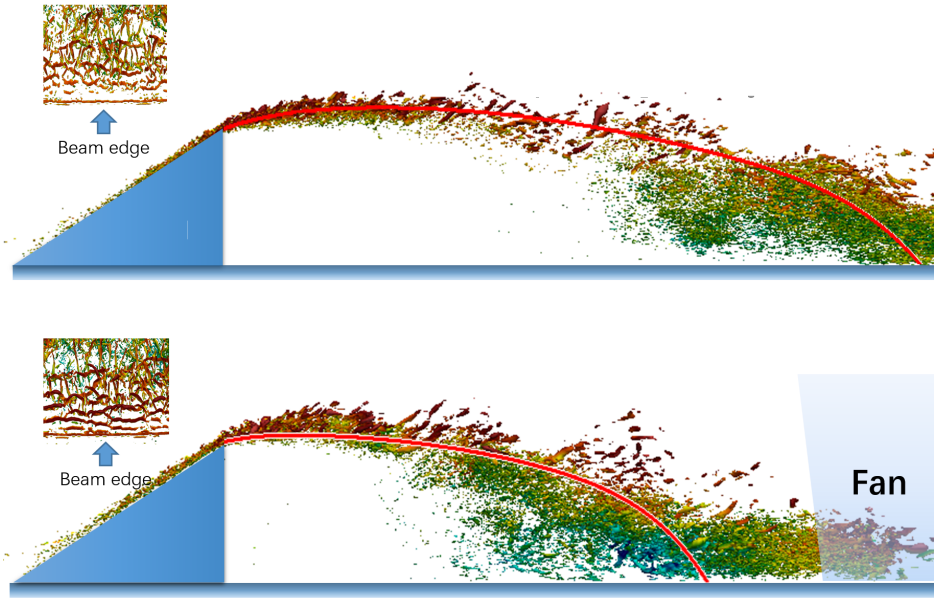

(b) Lateral view of instantaneous flow for the cases without/with fan

Fig. 5.6 Iso-surfaces of Q-criterion in different views

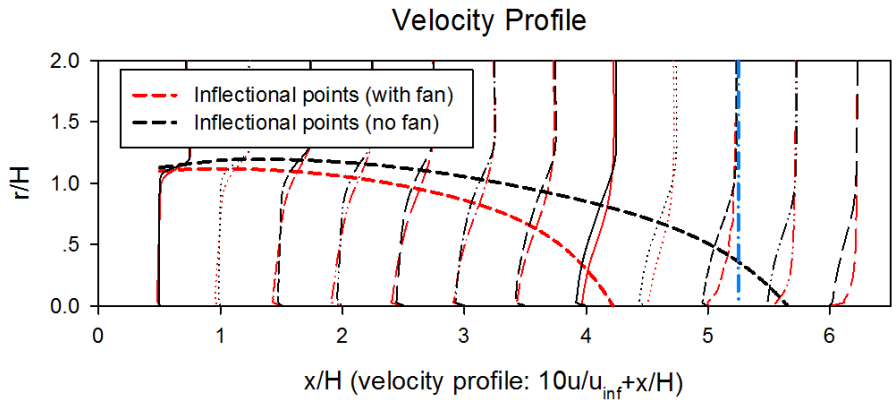

Fig. 5.7 Velocity profile at different streamwise locations (The blue dash-dotted line denotes the leading edge of the fan)

we split this recirculation region into Zone 1 where shear layer dominates, and Zone 2 where the fan influence dominates.

Figure 5.8a depicts the contours of the TKE, where its values in the shear layer, Zone 1 and in the reattaching regime, Zone 2 have increased by around 40% to 70% in the axial direction in the presence of the fan. A local maximum in the TKE at the leading edge of the blade tip is also notable. This local TKE has a minimal effect on the size of the separation bubble when compared to that of the potential field and the mass-flow redistribution. This aspect will be further investigated in Chapter 7.

We further analyse the increases by considering the change in Reynolds stresses. Figures 5.8b and 5.8c show that in Zone 2, both $\langle u'u' \rangle$ and $\langle v'v' \rangle$ increase significantly by approximately 40% and 75%, respectively. The increase in $\langle v'v' \rangle$ is much more pronounced than $\langle u'u' \rangle$, indicating a stronger turbulent transport in the wall-normal direction. This is similar to what is observed in the context of corner separation [179] at the leading edge of blade and is also consistent with the observations of Bradshaw [20]. We consider this increase in the Reynolds stresses to be a "direct effect" of the additional strain rate caused by the curvature change.

To reveal how the TKE is dynamically distributed, the TKE production and convection terms are investigated. Equation 5.2 presents all the relevant terms.

$$\frac{\partial k}{\partial t} = \underbrace{-\overline{u_i'u_j'}\frac{\partial \overline{u_i}}{\partial x_j}}_{\text{Production } \mathcal{P}} \underbrace{-\overline{u_j}\frac{\partial k}{\partial x_j}}_{\text{Convection } \mathcal{C}} - \frac{1}{\rho}\frac{\partial \overline{u_j'p'}}{\partial x_j} - \frac{\partial \overline{u_j'u_i'u_i'}}{\partial x_j} + \nu\frac{\partial^2 k}{\partial x_j^2} - \nu\overline{\left(\frac{\partial u_i'}{\partial x_j}\right)^2}, \tag{5.2}$$

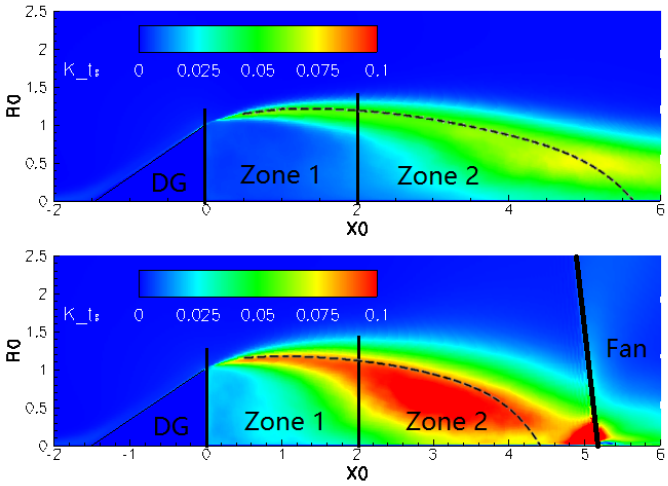

(a) Contours of TKE, up/down: no fan/fan

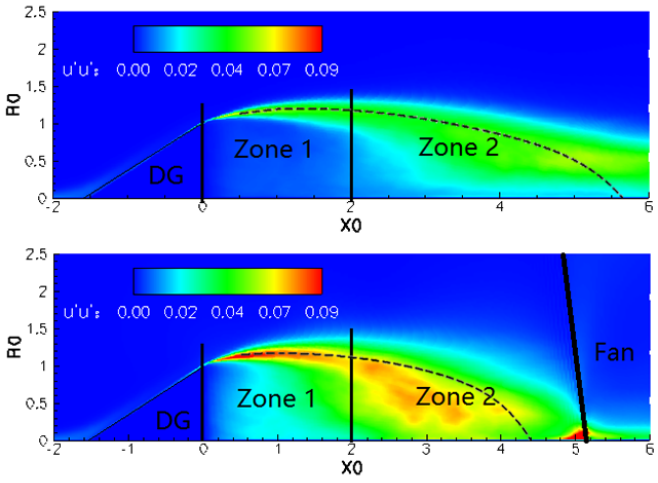

(b) Reynolds stress $\langle u'u' \rangle$, up/down: no fan/fan

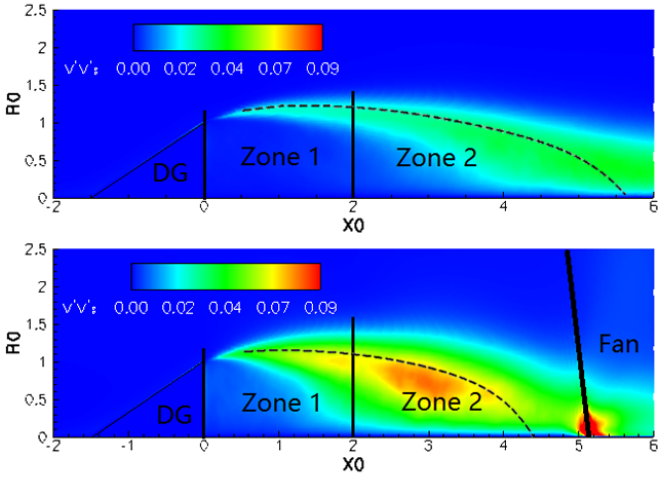

(c) Reynolds stress $\langle v'v' \rangle$, up/down: no fan/fan

Fig. 5.8 Turbulent Kinetic Energy and Reynolds stresses

We start with the convection distribution in Zone 2 because this zone is directly affect by the fan. Figure 5.9a illustrates its distribution, where the blue area indicates negative convection and the red positive convection. By the definition of convection in Eq.5.2, the dominant term is $-\overline{u}\dfrac{\partial k}{\partial x}$ because the axial velocity is much higher than the rest. Since the upper part of Zone 2 is negative and $\overline{u} > 0$, $\dfrac{\partial k}{\partial x}$ is positive, meaning that the TKE increases along the stream. Conversely, in the lower part, the TKE increases towards the negative x-direction. This means that the TKE is convected with the recirculating flow, and transported back to Zone 1. When the fan is installed, this convection process is greatly intensified. Consequently, we may conclude that the turbulence from the vicinity of the fan feeds back into the origin of the shear layer by means of the recirculating flow.

In Zone 1, the enhanced turbulence due to the convection further intensifies the shear layer. This can be seen in Fig.5.9b, a higher production in the shear layer is detected in the case with fan. Both the length and thickness of the strong production region increase in Zone 1 when the fan is installed. In Zone 2, this production increase is also evident: it expands more towards the casing. This could be the main source of the increased turbulent kinetic energy. To figure out whether this increase in production contributed from Reynolds stress or strain tensor, Figure 5.10 compares the velocity gradients $\partial U/\partial y$ to the Reynolds stress $\langle u'v' \rangle$. It is evident that when the fan is installed, the magnitude of Reynolds stress $\langle u'v' \rangle$ increase dramatically whereas the change in the velocity gradients is marginal or even decreases in Zone 1. Hence, the stress $\langle u'v' \rangle$ $(\partial U/\partial y)$ is found to be the major contributor to the TKE production.

Again, the increased TKE in Zone 1 is subsequently convected downstream into Zone 2 through the mainstream flow and results in cyclic feedback between the zones. Hence, although the flow in Zone 1 is not affected directly by the fan, it is still a key source of turbulence due to the feedback from the reverse flow. It supplements the turbulence generated in the vicinity of the fan in Zone 2 and also contributes to the earlier reattachment of the separation bubble. This can be an "indirect effect" of fan suppression. Hence, we may conclude that there are two distinct mechanisms through which the fan affects the separated flow: a shear flow dominant zone (Zone 1) and a streamline curvature dominant zone (Zone 2).

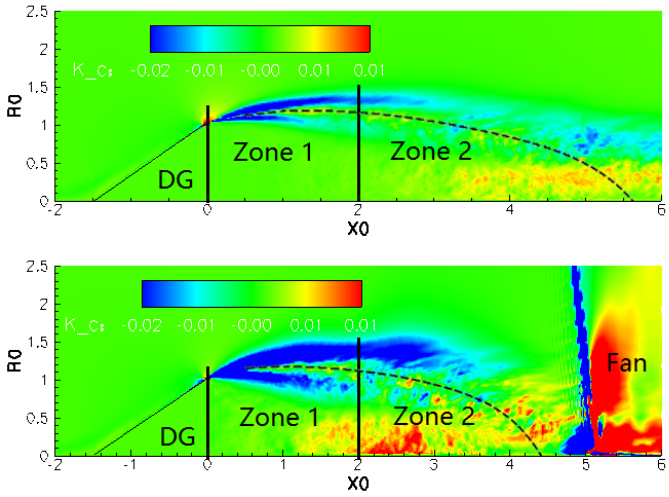

(a) Contours of TKE convection, up/down: no fan/fan

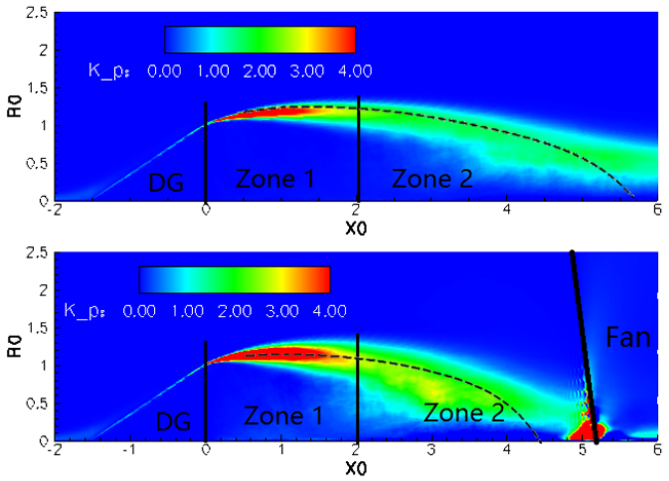

(b) Contours of TKE production, up/down: no fan/fan

Fig. 5.9 TKE convection and production

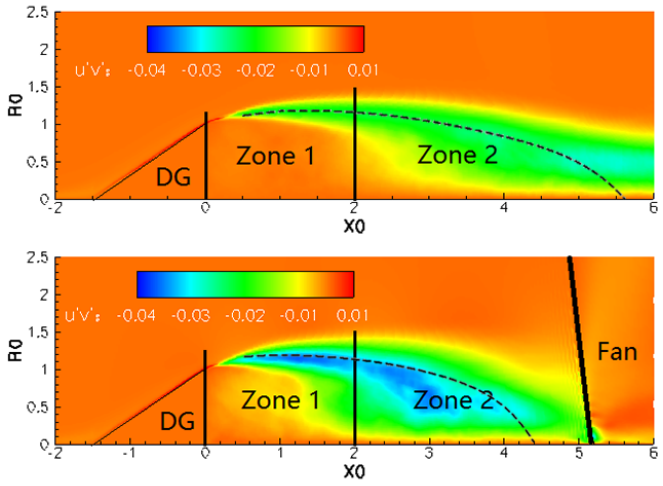

(a) Reynolds stress $\langle u'v' \rangle$

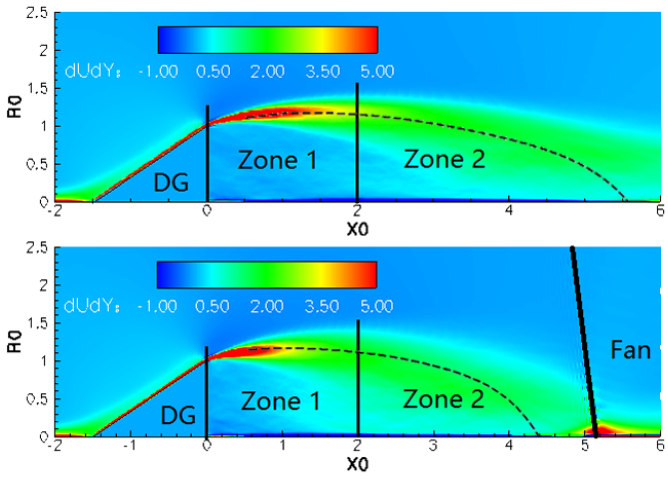

(b) Velocity gradient $\partial U/\partial y$

Fig. 5.10 Terms of TKE Production $\langle u'v' \rangle \, \partial U/\partial y$

5.4 Turbulence Structure

In this section, we further look into the turbulence structure to understand the fan effect. The Barycentric map [8] is used to capture the turbulence anisotropy in the spatial domain. This is quantified by the normalised Reynolds stress anisotropy tensor

$$a_{ij} = \frac{\langle u_j u_j \rangle}{2k} - \frac{\delta_{ij}}{3} \tag{5.3}$$

where $k = \langle u_i u_i \rangle / 2$. The eigenvalues λ_1, λ_2 and λ_3 ($\lambda_1 > \lambda_2 > \lambda_3$) of this asymmetric tensor then form three important coefficients

$$\begin{cases} C_{1c} = \lambda_1 - \lambda_2 \\ C_{2c} = 2(\lambda_2 - \lambda_3) \\ C_{3c} = 3\lambda_3 + 1 \end{cases} \tag{5.4}$$

According to Banerjee et al. [8], these three coefficients capture the 1-component, 2-component and 3-component (or isotropy) states of the turbulence, respectively. Accordingly, Emory et al. [43] proposed that the RGB colouring system can be applied to illustrate this turbulence componentality in the spatial domain. Here the RGB value can be formulated as

$$\begin{bmatrix} R \\ G \\ B \end{bmatrix} = C_{1c} \begin{bmatrix} 1 \\ 0 \\ 0 \end{bmatrix} + C_{2c} \begin{bmatrix} 0 \\ 1 \\ 0 \end{bmatrix} + C_{3c} \begin{bmatrix} 0 \\ 0 \\ 1 \end{bmatrix}. \tag{5.5}$$

Hence, each point within the flow field has a corresponding RGB value which represents the anisotropy associated with the turbulent flow. The anisotropy componentality contours of the separation region for the two cases are depicted in Fig. 5.12.

Frame (a) shows that inside the bubble, the turbulence is of mainly 2 and 3-component form (coloured in green and blue). When the fan is installed (Frame (b)), the flow reattaches earlier and the recirculation region becomes bluer, meaning the turbulence becomes more isotropic. This indicates that the fan can redistribute the anisotropy within the separation bubble. In the vicinity of the fan (Zone 2), it is the direct effect we discussed previously that moves the 1-component turbulence dominant region (coloured in red) towards the beam.

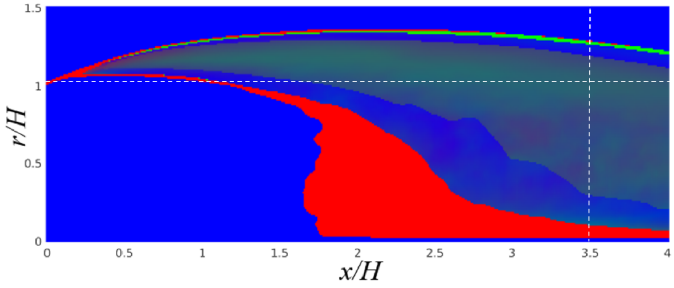

(a) No fan

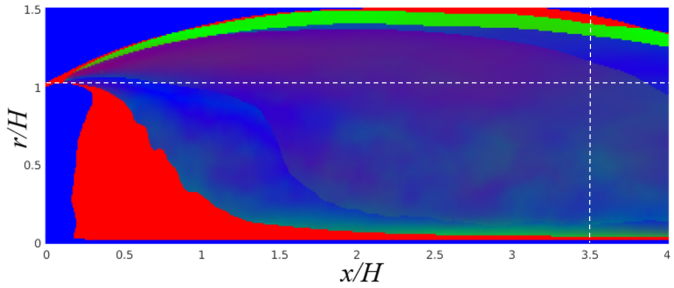

(b) With fan

Fig. 5.11 Anisotropy componentality contours: red: one-component, green: two-components, blue: isotropic

To quantify this trend to isotropy, and show such variation, two variables are defined according to [8]. These are

$$x_B = C_{1c} + \frac{1}{2}C_{3c}, y_B = \frac{\sqrt{3}}{2}C_{3c}. \tag{5.6}$$

Hence, this coordinate system defines a Barycentric map, and three limiting states, 1/2/3 components $X_1 = (1, 0), X_2 = (0, 0), X_3 = (1/2, \sqrt{3}/2)$, can be fixed at the three vertices of the equilateral triangle on the map (Fig. 5.12a). For the present case, two positions are chosen to show the trajectories of the anisotropy variations. They are extracted along the lines marked in Fig. 5.11: $r = H$ (along the shear layer) and $x = 3.5H$ (across the shear layer). Frame 5.12a shows that, along the shear layer, the region defined by $x = H - 4H$ is significantly more isotropic due to the presence of the fan. Similarly, in the radial direction, Frame 5.12b also illustrates that the turbulence tends to be more isotropic within the recirculation region ($r = 0.3H - 1.2H$). This demonstrates that the fan weakens anisotropy specifically during the flow reattachment within in the recovering wake region. This is attributed to the following factors: a) the early reattachment process promoted by the fan (also noted by Alam and Sandham [5] and Vadlamani [159]) and b) the adverse pressure gradient experienced by the flow as it approaches the fan. Both of these factors contribute to the effective redistribution of turbulence, promoting isotropy. However, Figure 5.11 also shows that in the majority of the recirculation region, the turbulence still shows strong anisotropy: near 1-component within the shear layer and mixed components in the rest of the area. This is consistent with the findings of [159] and [13] in the context of separation induced due to adverse pressure gradients and separation from a rounded step respectively. Unlike the eddy-resolving simulations (LES/DNS), the RANS models using isotropic turbulence could hence be inaccurate in predicting such regions to have strong anisotropy.

We may further deduce that the anisotropy redistribution caused by the fan could have three benefits. Since isotropic turbulence is always homogeneous by definition, the gradient of the mean variables of the potential flow is diminished [24]. As a result, the distortion in front of the fan is alleviated. The other two benefits relate to the increased turbulence level. The turbulence can be much more easily diffused in all directions by more isotropic turbulence. Hence, the mixing process between the recirculated flow and the mean flow can be enhanced, leading to an earlier reattachment. In addition, the increased energy generated from the shear layer can be also be quickly dissipated by such fully developed turbulence. Consequently, the energy of the distorted flow will decrease and the distortion will be alleviated.

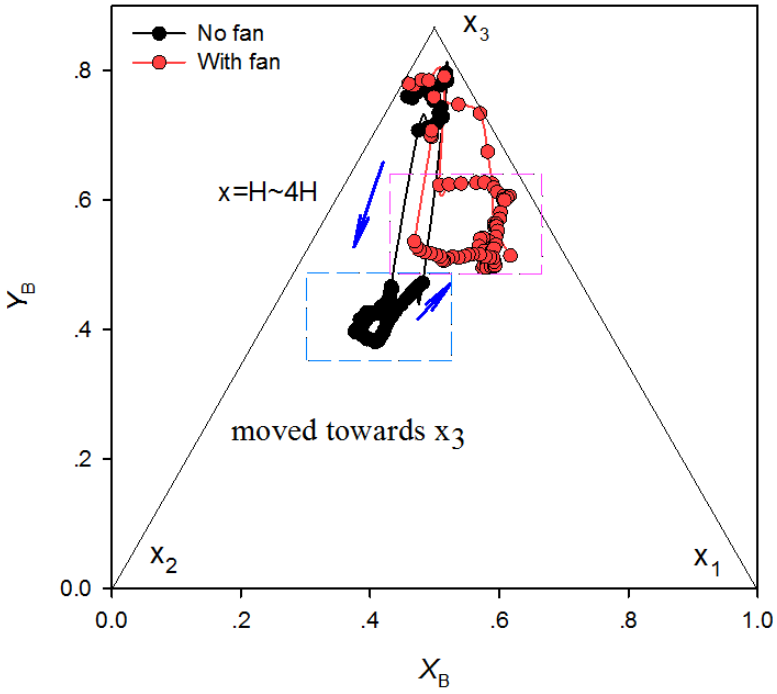

(a) $r = H$

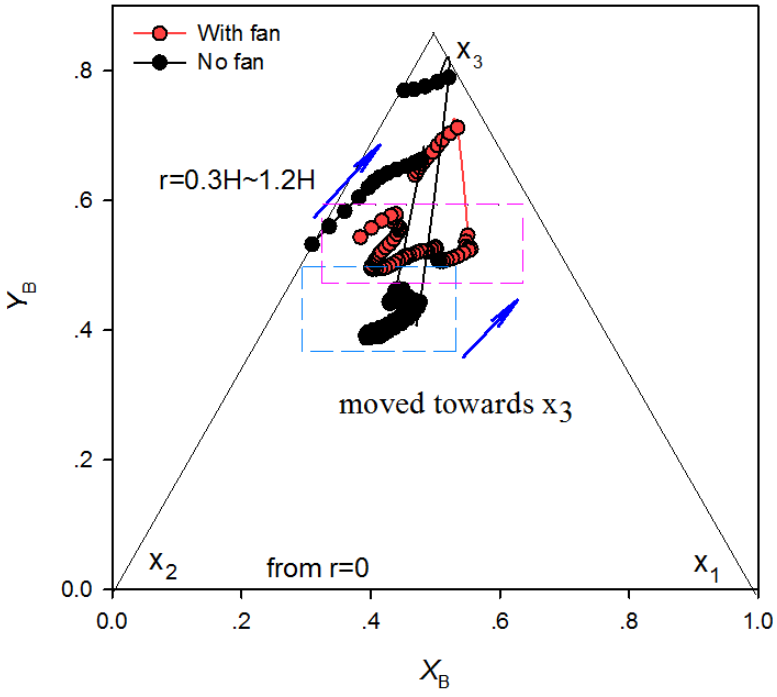

(b) $x = 0.5H$

Fig. 5.12 Barycentric maps

5.5 Concluding Remarks

This chapter applied eIBMg with LES to the investigation of fan-intake interaction and demonstrated that there are two mechanisms through which the fan affects the separated flow: Firstly, the suction effect of the fan (effective up to almost half of the chord length upstream of the fan) accelerates the flow in the intake and changes the streamline curvature. This change closes the recirculation bubble much earlier and alleviates the undesired distortion "directly". In contrast, the adverse pressure gradient caused by the fan also increases the production of turbulence near the fan leading edge. Secondly, within the recirculation region, the strain rate and turbulence transport are intensified. The enhanced turbulence in the vicinity of the fan feeds back into the initial growth of the shear layer by means of the recirculating flow. This "indirect" feedback is found to increase the turbulence production and the spreading rate of the shear layer. Both these direct and indirect effects of the fan significantly suppress the inlet distortion. However, which effect dominate this process is still not clear. This will be investigated in Chapter 7. In the following Chapter, the reader will see how the direct effect suppresses distortion in a range of scenarios. Through corresponding parametric studies, the reader will also see how this effect is significant for fan design.

Chapter 6

Suppression of Intake Distortion

In Chapter 5, the following mechanisms of fan influence on distortion were revealed: (1) it directly accelerates the potential flow, changes the streamline and hence suppresses the separation; (2) it also intensifies the turbulence via recirculation within the separation and thus enhances the mixing process which also contributes to a reduction in separation. In this Chapter, we talk about the first aspect and examine how this direct effect can be utilised for fan design. The direct effect is modified and investigated by exploring three aspects: blade type, fan location and intake distortion size. The second aspect will be discussed in Chapter 7.

6.1 Case Framework

The case in this Chapter is still based on the simplified case in Chapter 5, run at 65% rotational speed (1361.31 rad/s) and 10.6 kg/s mass flow rate. This operating point is keep the same for all the cases in this chapter and Chapter 7. The case with 100% rotational speed is not chosen because there are shock waves in the fan region which may influence the suppression of distortion and complicate the analysis. When investigating the impact of blade types, the original blade (hub-loaded) and a new tip-loaded blade were used. Details for the new designed blade is discussed in the next section. Variations for fan locations and intake distortion are illustrated in Fig. 6.1. They all use the new tip-loaded blade. In the original case, the distortion generator ('beam') of height 'H' and length '$1.5H$' is placed at an axial distance of '$12.5H$' from the inlet. The fan is positioned at a streamwise distance of '$5.2H$' from the beam. In Frame (a.1-3) on the left, the fan is moved downstream to two different locations: 'Loc1', a distance of a half-chord ($x = 6.2H$) and 'Loc2', a full chord distance ($x = 7.2H$). The Frame (b.1-3) on the right illustrates cases with different beams

heights, $1/2H$ and $1/4H$, installed at the same location. The beam is still represented using the standard IBM. The separated flow downstream of the beam is captured using an eddy resolving approach (LES), while the force field of the rotating fan is replicated using the eIBMg approach.

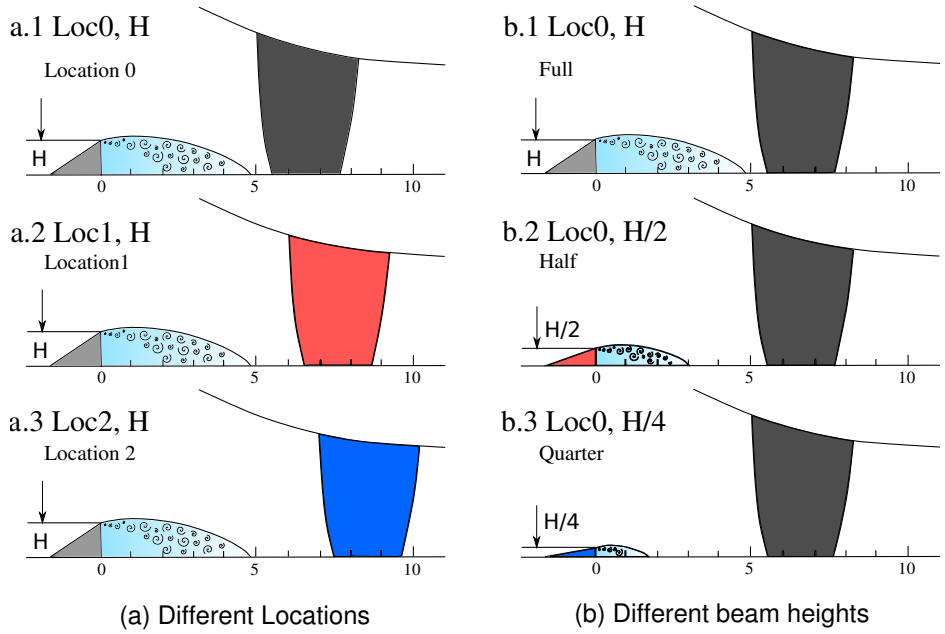

Fig. 6.1 Sketch of the test cases for varying (a) fan-locations and (b) beam heights

Since LES has a very high requirement on the mesh resolution, a mesh independence study is performed before any detailed flow physics analysis takes place. Two mesh resolutions are tested and the number of nodes for the coarse and fine meshes are 8.6 million and 60 million, respectively. The dimensionless spacing constraints for the two meshes in each of the three directions can be found in Table 5.1. Figure 6.2 compares the axial velocity and TKE at the position $x = 4.5H$ predicted on the coarse and fine meshes. It can be seen that neither distribution is visibly influenced by the mesh size, thus indicating that mesh independence has been achieved.

6.2 Blade Type

Different types of fan blade have an impact on intake distortion. This section explores two different types: the original blade (hub-loaded) and a new tip-loaded blade. The new blade was designed by modifying the angle distribution of the trailing edge. It has a more gentle turning angle at the hub and a sharper angle change at the tip (Fig.6.3), but the total work of blades is kept the same. (The work for the original blade is

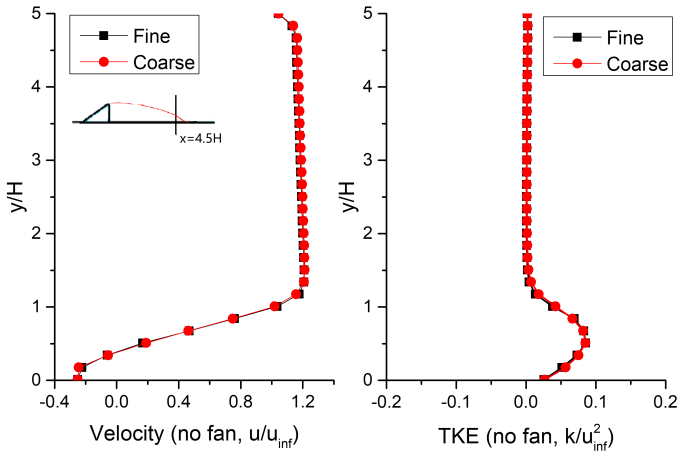

Fig. 6.2 Mesh sensitivity study from LES showing the radial variation of (a) velocity and (b) TKE at x=4.5H, without fan

$1.58 \times 10^4 J$ and that for the new one is $1.66 \times 10^4 J$. The relative different is 4.7%). Figure 6.4 shows the loading distributions of these two types of blades extracted near the blade leading edge. In Frame (a), the turning angle of the new tip-loaded blade is higher at the casing and lower at the hub compared to the original one. Accordingly, the blade of the original blade generates more work around the hub (hub-loaded), whereas the new one does more near the tip (tip-loaded). Correspondingly, the mass flux is much higher around the tip for the new blade shown in Frame (b).

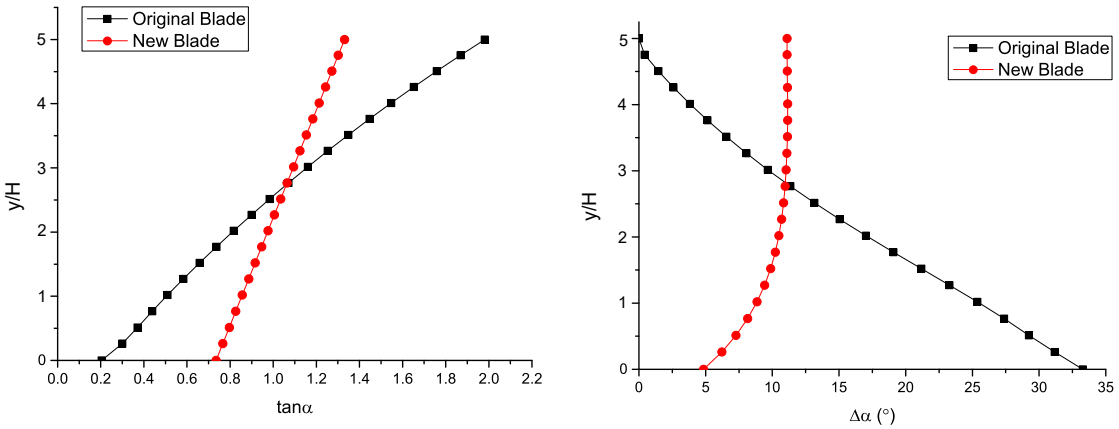

(a) Angle distribution at trailing edge (b) Turning angle distribution

Fig. 6.3 Angle distribution of the original blade and new blade

Figure 6.5 compares how both blades affect the intake distortion quantified by mass flux and total pressure ratio. Evidently the blade can suppress the separation bubble

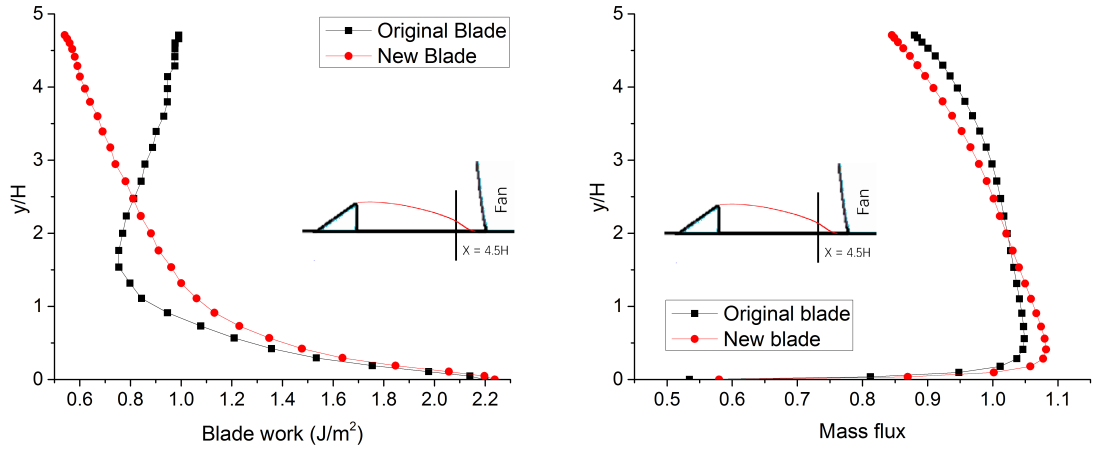

(a) Work distribution (b) Mass flux distribution

Fig. 6.4 Characteristics of original and new blades

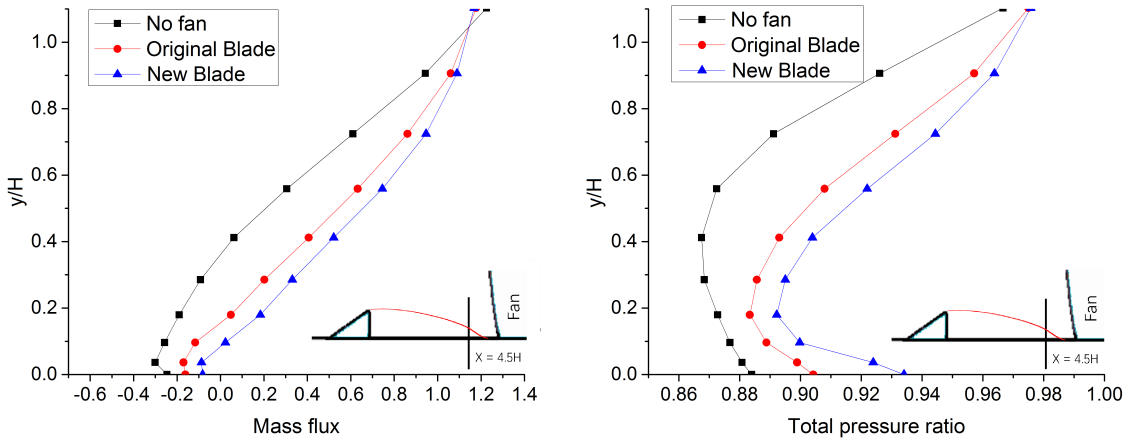

(a) Mass flux distribution (b) Total pressure distribution

Fig. 6.5 Effects of a fan on intake distortion

and improve the total pressure ratio considerably. Between the two blades, the effect of the tip-loaded one is more significant. It can increase the mass flux downstream of the separation by around 30%, and also nearly 3% for total pressure ratio.

6.3 Fan location

The effects of fan location are discussed in this section. To explore how the distance between fan and the distortion generator will affect the distortions, the tip-loaded blade is moved downstream to two different locations: a distance of a half-chord and a full chord, corresponding to $x = 5.2/6.2/7.2H$.

Figure 6.6 illustrates the time-averaged axial velocity contour and Q-isosurface of these three cases. It can be seen that the recirculation region contoured in green and blue is slightly larger when the fan is located further downstream from Frame (a) to (b). A detailed comparison (Figure 6.7) shows that the original location has the highest effect in increasing of the mass flux and total pressure ratio. A blade location which is further away will have less of an influence in suppressing the separation.

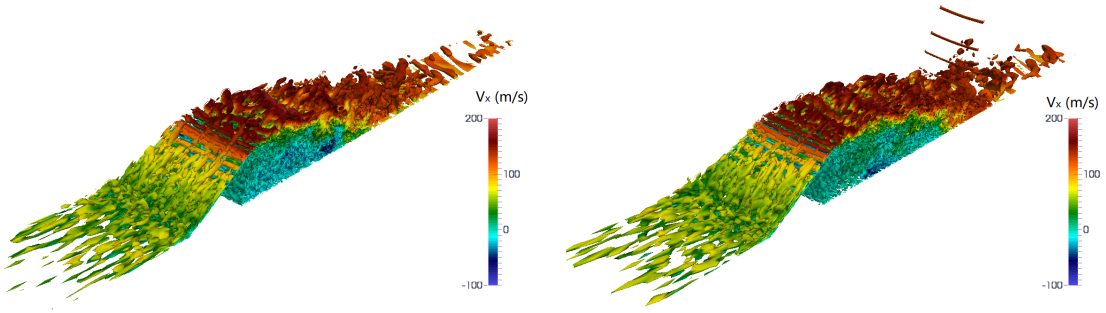

(a) Location 1 $x = 6.2H$ (b) Location 1 $x = 7.2H$

Fig. 6.6 Q-isosurfaces ($Q = 1 \times 10^7$) coloured with axial velocity for different fan-locations (a) $x = 6.2H$ and (b) $x = 7.2H$

To quantify this blade effect, we define a Recovery Factor to describe how well the blade will cope with the intake distortion and improve the flow condition. Firstly, we introduce a mass-weighted total pressure loss $P_{t,loss}$,

$$P_{t,loss} = 1 - \frac{\int p_t d\dot{m}}{p_{t,in}\dot{m}}. \tag{6.1}$$

This reflects the total pressure loss at a designated position, e.g. 10% of the blade chord upstream the leading edge. Then a Recovery Factor is defined as,

$$RF = 1 - \frac{P_{t,loss}}{P_{t,loss,NF}}, \tag{6.2}$$

where NF means 'no fan'. This quantifies the percentage of the total pressure recovery when a fan is installed. These RFs for the fan at different locations are depicted in Fig. 6.8.a, and all of the data are extracted from the same axial location $x = 4.5H$, 10% of the blade chord upstream of the blade leading edge. Hence, it is obvious that the fan nearer to the intake will considerably improve the total pressure ratio. This is reasonable because a nearer fan, i.e. short intake can stop the development of the separation much earlier. It is argued that the short intake, on the other hand, may also stall the fan earlier. Pullan et al. [123] found that high incidence can trigger thick boundary layers and flow separations near the fan leading edge, which consequently develop to a rotating stall. Studies by Perovic et al. [117], however, demonstrated that the corresponding reduction in stability margin is small, only 1% to 2% flow coefficient. As in the present scenarios (take-off or landing), the engine works around the peak efficiency point, the potential instability resulted from a short intake may not be a major problem. That being said, it should be further investigated whether a short intake may significantly reduce the stall margin under other scenarios, such as cross wind.

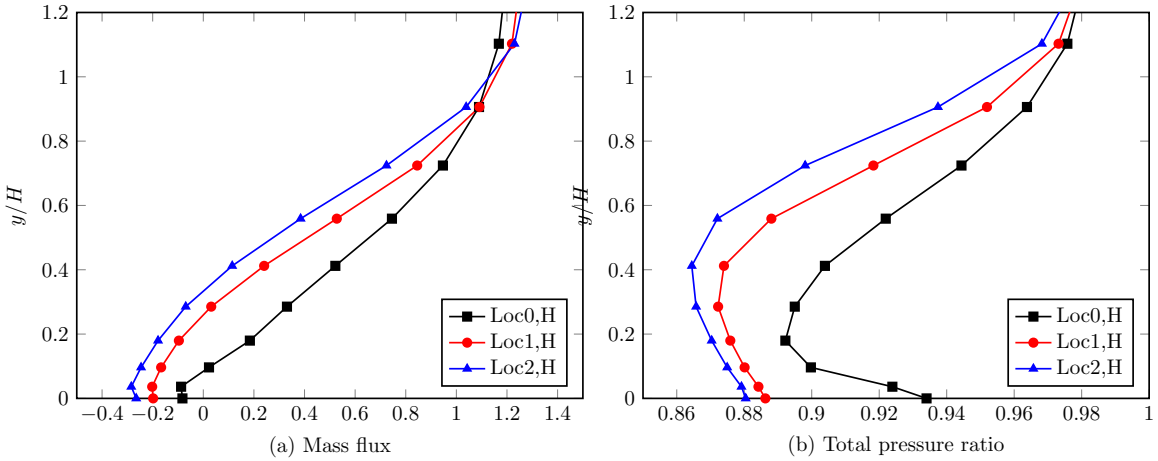

Fig. 6.7 Effects of different blade locations on (a) mass flux and (b) total pressure ratio

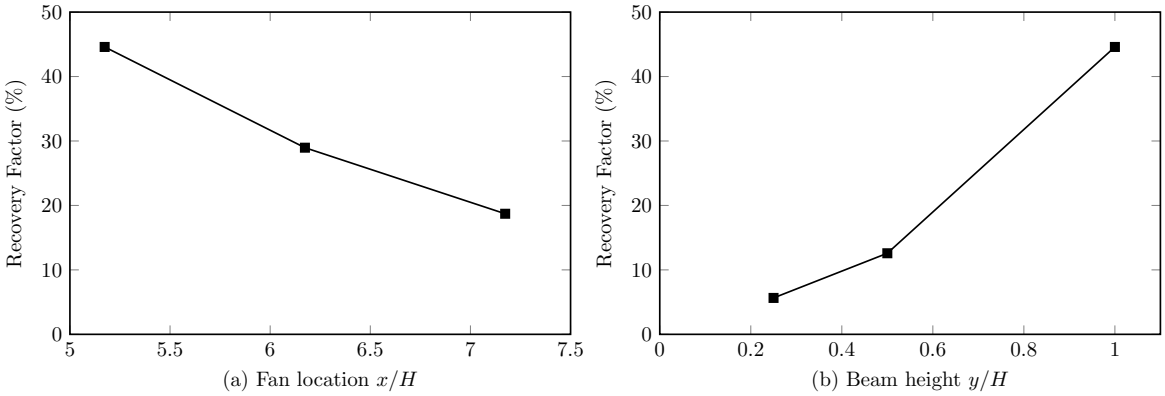

Fig. 6.8 Recovery Factor with varying (a) fan-locations and (b) beam heights

6.4 Inlet Distortion

The effects of the various degrees of distortion are discussed in this section. To simulate these distortions, two types of bevelled beams were installed at the original location with the tip-loaded blade fixed in the downstream. Figure 6.9 illustrates the flow distributions of these cases, where both the influence of fan and that of the beam can be compared.

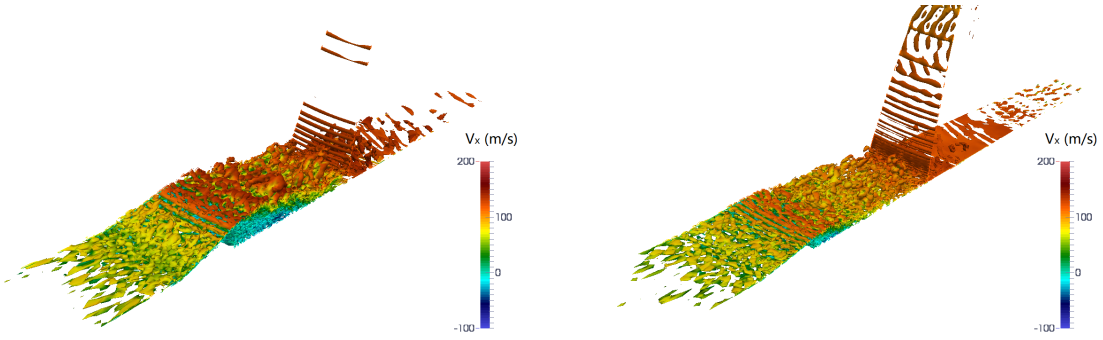

(a) 1/2H, with fan (b) 1/4H, with fan

Fig. 6.9 Q-isosurfaces (Q=1 × 10^7) coloured with axial velocity for different beam heights

To quantify the effect of these distortions, the relative total pressure loss is illustrated in Fig. 6.10. This figure shows that, when the height of the beam is changed linearly, the distortion-induced loss varies significantly. This can be also demonstrated by the case of the flow distribution without a fan in Fig. 6.11.

In this figure, the original distortion (or full-scale beam) has a remarkable influence on the main stream, compared to the other two cases. The mass flux is completely

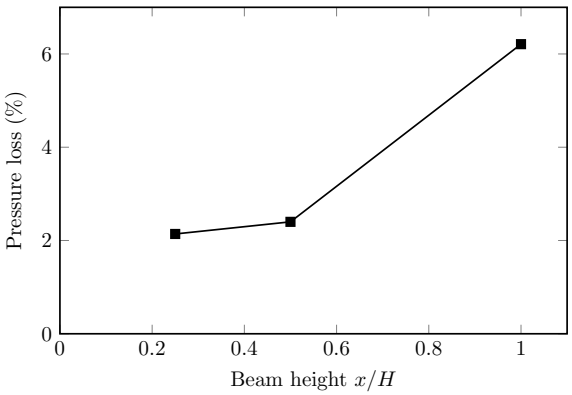

Fig. 6.10 Total pressure loss with increasing beam height

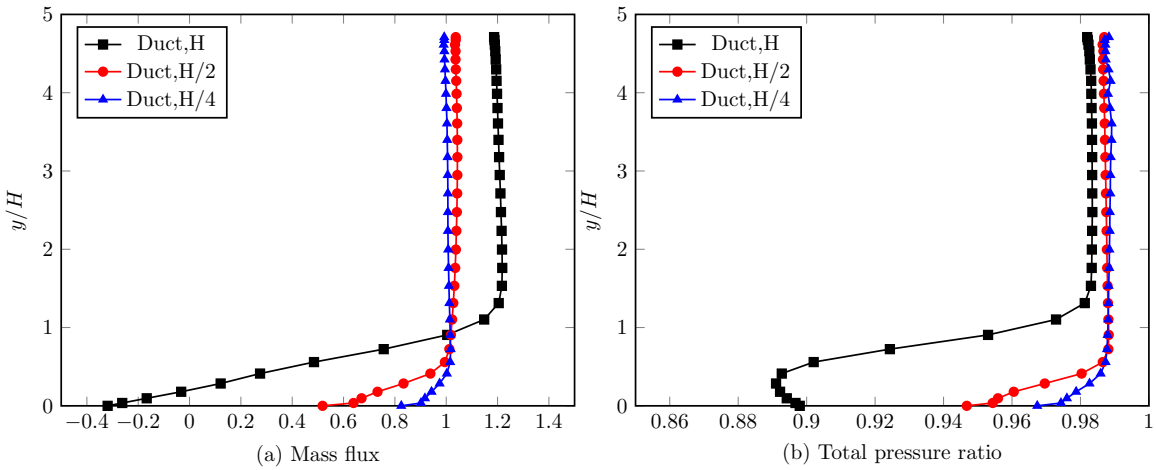

Fig. 6.11 Effects of different degrees of distortion on (a) mass flux and (b) total pressure ratio in the absence of fan

redistributed throughout the channel, and the main flow sees a nearly 20 % change in its magnitude. In contrast, the distortion does not have a big impact on the main flow when using the $1/2H$ and $1/4H$ beams. The total pressure loss is also significant for the full-scale beam, at nearly 11% within the separation region and 2% for the main flow. Figure 6.12 shows how the blade responds to these various distortions.

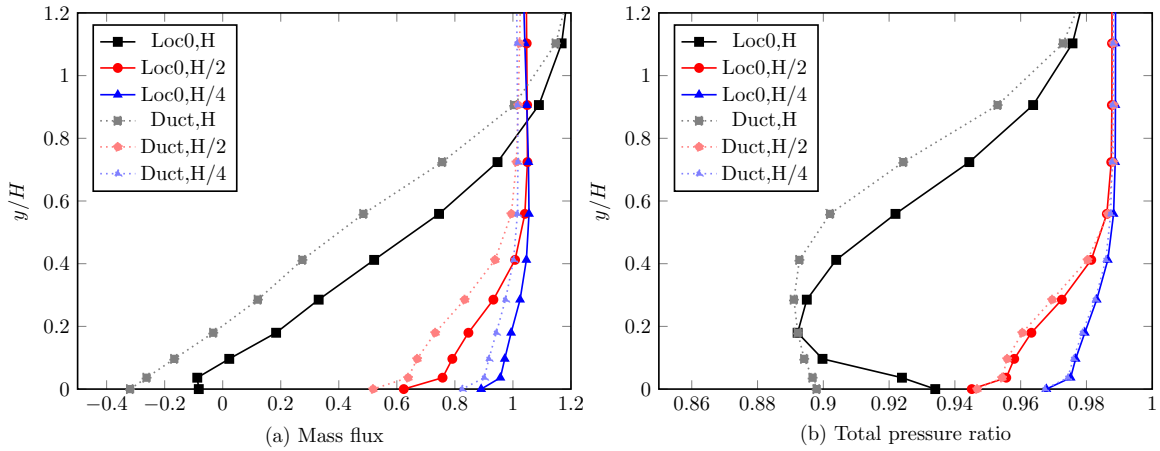

Fig. 6.12 Effects of different degrees of distortion on (a) mass flux and (b) total pressure ratio. 'Loc0' corresponds to the case with fan placed at $x = 5.2H$ and 'Duct' corresponds to the case without fan.

Evidently, the fan is capable of alleviating the distortions. The effect for the original beam is the most significant, showing a 20% increase in mass flux and a 2% increase in total pressure. The effects for the $1/2H$ and $1/4H$ beams are minor. Equation 6.2 is used to quantify this effect and Figure 6.8.b shows the Recovery Factor of the fan when coping with these distortions. Obviously, the improvement due to the fan for the full-scale beam is remarkable, at around 44%. This proves that this tip-loaded blade is capable of reducing the intake distortion, even if the flow condition has been significantly changed by the full-scale beam.

6.5 Concluding Remarks

This Chapter applies the mixed-fidelity method to the investigation of the fan influence on the intake distortion. Results indicate that the loading distribution has a substantial impact on the reduction of the separation bubble. A tip-loaded fan tends to suppress more the separation and hence alleviate distortion better than the original hub-loaded blade. The location of fan also has a significant influence on intake distortion. The nearer the downstream fan, the stronger the influence in terms of suppressing separation.

The fan at the proposed location can recover 45% of the loss. This is because the rotational fan can accelerate the upstream flow at the casing, thereby reducing the separation bubble and alleviating the distortion.

Various sizes of distortion are finally studied. This is achieved by changing the beam height. It is found that the original beam has such a significant influence that the main flow can be even changed by almost 20%. Nevertheless, the proposed blade is still capable of weakening such distortions. The effects of the blade at different beam heights are also quantified with the conclusion that, when the distortion is larger, the fan has a stronger effect. This change is non-linear, and when the beam height is reduced to $H/4$, the Recovery Factor becomes $RF/7$. This means that a well-designed blade could show substantial power when dealing with any possible intake distortion. Hence, the fan could form an essential component for intake distortion control.

Chapter 7

Prediction of Intake Distortion

Chapter 5 discusses the influence fan on distortion from two perspectives, main flow acceleration and turbulence enhancement. However, which factor dominates this process is not clear. This chapter addresses this issue and investigates how both factors affect the prediction of separated flows in the fan-intake interaction.

7.1 Case Framework

To achieve this goal, we use the same cases in Chapter 6, but run both RANS and LES and compare their differences. The RANS simulations were carried out on the LES mesh comprising of 8.6M nodes (mesh independence has been shown in Fig. 6.2). The averaging process starts when a fully developed flow was achieved and lasted for approximately 15 flow-throughs. These comparative studies contain distorted flows (1) without fan, (2) with a fan at different axial locations and (3) with different beam heights while keeping the original location (see Fig.6.1). To investigate how these factors influence the prediction of separated flows, we focus on velocity profiles and TKE, non-dimensionalised by u_∞ and u_∞^2, respectively. The reference velocity u_∞ is measured in the main flow near the beam edge.

To quantify the effect of the fan and the discrepancies between RANS and LES approaches, we use two non-dimensionalised parameters; the acceleration parameter K, and the discrepancy in the angle of the blade incidence, $\Delta\theta$. The former is defined according to Launder [83] as

$$K = \frac{\nu}{u_\infty^2}\frac{\partial U}{\partial x}. \tag{7.1}$$

The discrepancy between the RANS and LES results can be critical in terms of predicting the downstream fan performance, so we associate it to the incidence angle

and define

$$\theta = \tan^{-1}\frac{r\Omega}{U} - \theta_b, \Delta\theta = \theta_{RANS} - \theta_{LES}, \tag{7.2}$$

where θ_b is the blade leading-edge angle.

7.2 Distortion without Fan

Figure 7.1 illustrates the velocity and TKE profiles for distorted flows in the contracting duct without a fan. Evidently, the discrepancies are significant within the separation region for both the $k-\omega$ and SA models in the region near the casing. Frame (b) shows that the TKE predicted by the RANS $(k-\omega)$ model is considerably higher than the one predicted by LES. The overestimated TKE corresponds to stronger turbulence, and thus leads to a stronger mixing process. As a result, the distorted flow has reattached at $x = 5H$ in RANS case, which is much earlier than the LES result. Detailed analysis for the reasons of RANS failure can be referred to Appendix 2. Therefore, for the case without fan, the turbulence model is important and may substantially affect the prediction. Hence, an eddy resolving simulation is required.

7.3 Distortion with Fan Effect

Chapter 5 has demonstrated that a fan is able to accelerate the flow near casing. This acceleration has a significant impact in reducing the bubble. This section discusses the influence of a fan on the characteristics of intake distortion.

7.3.1 Effects of Fan Location

The test cases with different fan locations $x = 5.2H/6.2H/7.2H$ discussed in Chapter 6 are investigated by RANS and LES results respectively. Figure 7.2 shows the change in the velocity profiles when the fan is placed at different locations. It is clear that, when the fan is installed, it significantly accelerates the flow and changes the streamline curvature. When the fan is at the original location, the difference between RANS and LES is almost eliminated. In Frame (a), the velocity profiles almost overlap near the leading edge of the fan (at $x = 5H$). This applies to both the $k-\omega$ model and the SA model. As the fan effect becomes weaker due to the increased distance (Frame (b) and (c)), the difference between the RANS and LES profiles becomes larger. In this situation, a high-fidelity simulation, which resolves turbulence, is more reliable.

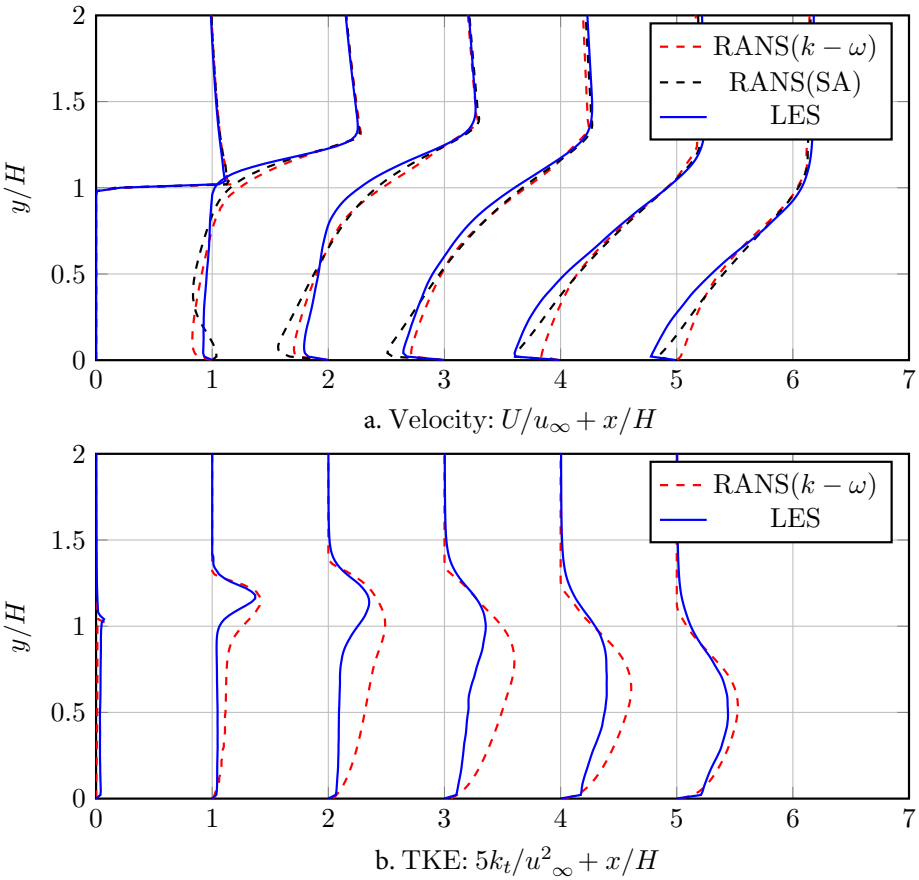

Fig. 7.1 Carpet plots comparing the (a) Velocity profiles and (b) TKE profiles between RANS and LES for the case 'Duct, H'

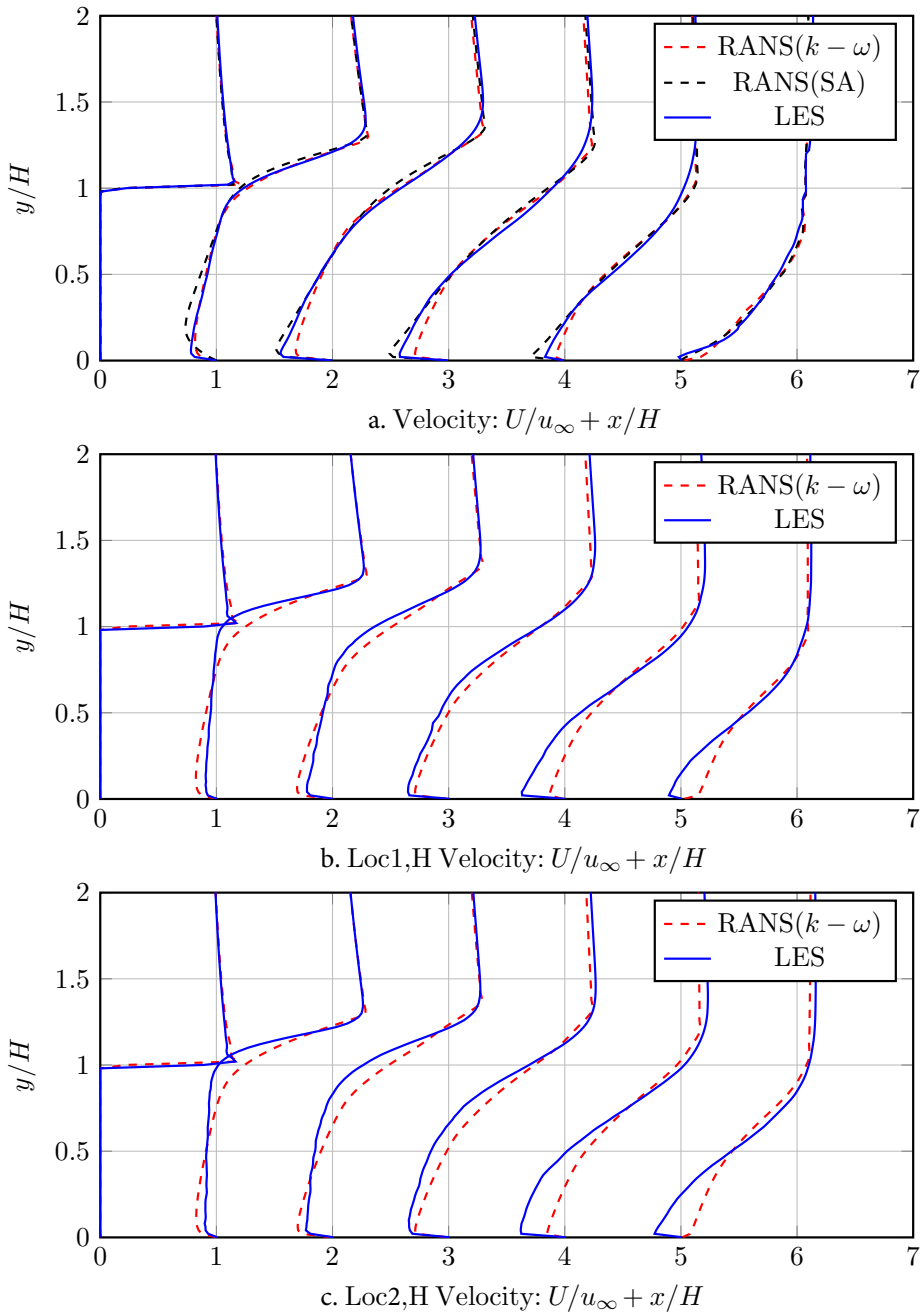

Fig. 7.2 Carpet plots comparing velocity profiles predicted by RANS against LES for a given distortion generator of height, H and varying fan-locations: cases (a) Loc 0 (b) Loc 1 (c) Loc 2

To investigate how the discrepancy in the velocity profiles impacts the flow near the fan face, we extract the total pressure distribution, acceleration parameter and angle of incidence at $x = 4.5H$, as shown in Fig. 7.3. Frame (a) shows that the original location has the highest effect in increasing the total pressure ratio, whereas the fan placed further away (illustrated by the blue curves for $x = 6.2H$ and black curves for $x = 7.2H$) had less influence in suppressing the distortion. There is also an increasing trend in the discrepancy when fan is moved downstream. When the fan is placed at Location 0, both the RANS and LES successfully predict almost the same the total pressure. This means that turbulence resolving may not be necessary and the RANS approach might be sufficient. When the fan is placed at the other locations or removed, however, the rising discrepancies indicate that the RANS results may be unreliable.

Frame (b) compares the acceleration parameter, K, extracted at the same location. The flow for the case 'Loc0' has reattached whereas it remains separated in the other cases. Evidently, the fan at the original location induces the highest acceleration (the line for 'Loc0, H'), followed by the cases in which the fan is at Locations 1 and 2, meaning that the further location of the fan, the weaker acceleration.

Frame (c) shows the angle of incidence at this fan face from the LES results with the 'error bands' compared to RANS. The case without a fan represents the most significant difference. In contrast, the case 'Loc0, H' has the lowest discrepancy due to the downstream fan effect. When the fan is moved downstream to Locations 1 or 2, the discrepancies become greater. This indicates that the prediction of the separated flow under high acceleration depends less on the RANS model.

7.3.2 Effects of Beam Height

The effect of the fan in terms of the different distortions induced is also investigated using two beams with difference heights, $1/2H$ and $1/4H$, installed at the same location. Figure 7.4 plots the velocity profiles from both the RANS and LES results.

It should be noted that the distorted flows reattach at difference axial locations, which are much earlier for the case with a smaller beam. Due to the difference in the separation region, the data cannot be compared at the same actual location. For consistency, we focus on the data outside of the separation region, i.e., in the boundary layer after reattachment $x > 4H$. As expected, although the region of the discrepancy may be reduced further away from the casing, its maximum near the wall increases.

The discrepancies in regard to the velocity near the wall have an influence on the total pressure upstream of the fan, as shown in Frame (a) of Figure 7.5. Near the wall, the difference between the RANS and LES models increases when the beam height

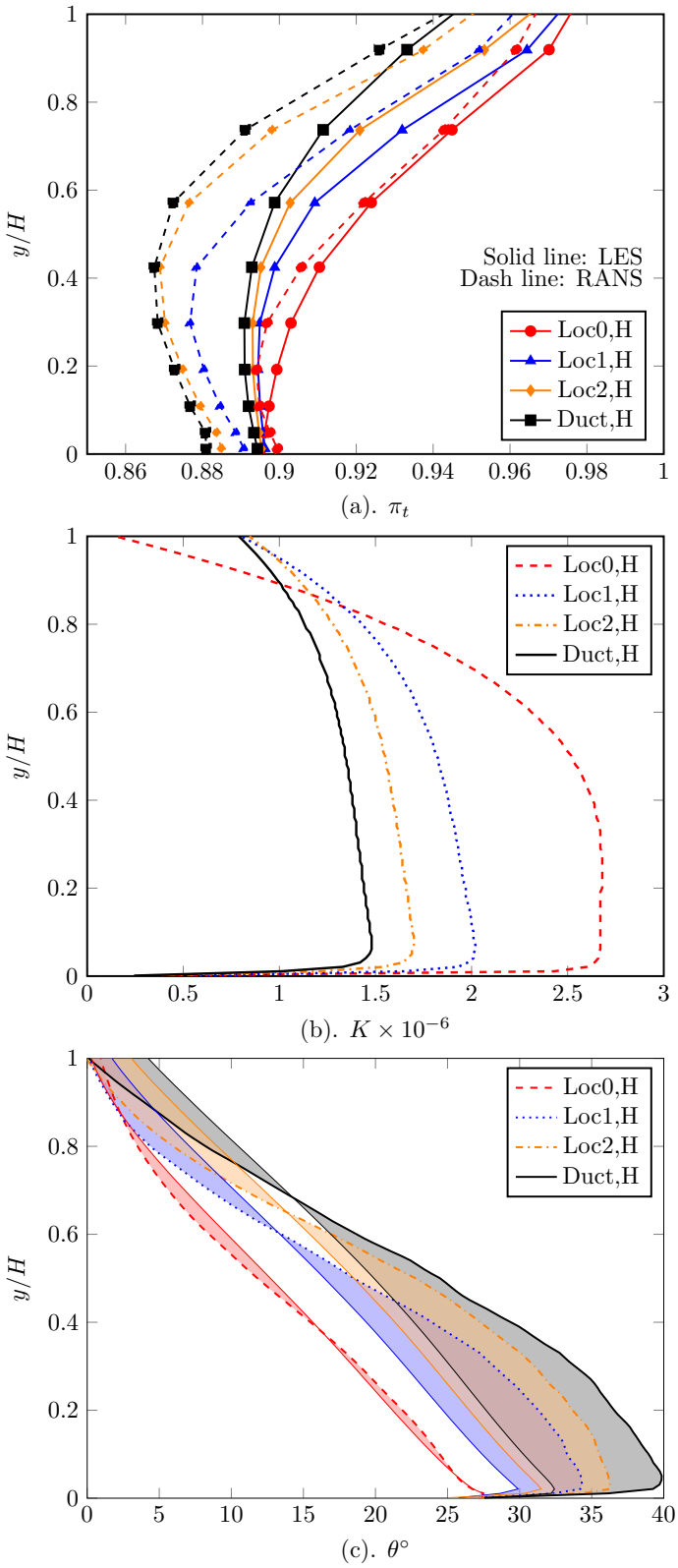

Fig. 7.3 Radial distributions of (a) total pressure ratio (b) acceleration parameter (c) angle of incidence predicted by RANS and LES at x = 4.5H. Cases compared for same beam height, H and varying fan-location: Loc0, Loc1, Loc2. Test case without fan (Duct, H) is also shown.

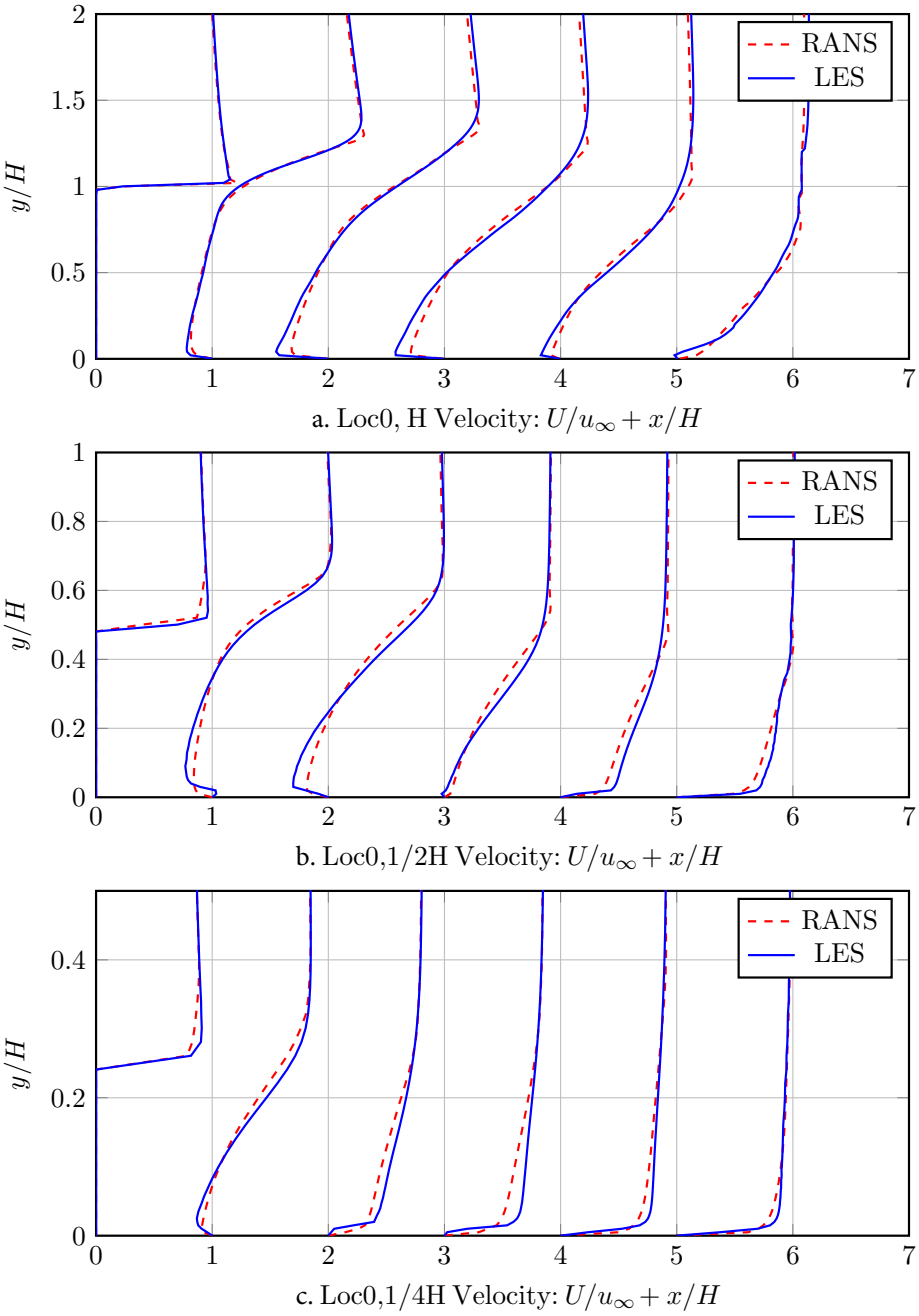

Fig. 7.4 Carpet plots comparing the velocity profiles predicted by RANS and LES for a given fan-location 'Loc0' and varying beam heights (a) H (b) H/2 (c) H/4

is reduced and the acceleration is weakened. Hence, for these cases, turbulence or the wall effect plays a more important role, so an eddy-resolving method is essential. Otherwise, the loss, boundary layer ingestion, potential flow separation, etc. near the intake wall can be wrongly estimated by RANS.

To characterise the fans influence on the different inflow distortions, the acceleration parameter K is plotted in Frame (b), extracted at $x = 4.5H$. The $1/2H$ beam generates a higher acceleration than the $1/4H$ beam with the same fan. This is reasonable because, for a larger obstacle, the streamline curvature is larger, and thus the acceleration is stronger. The corresponding discrepancies in the predicted incidence angles are depicted in Frame (c). Evidently, as the acceleration is reduced, the incidence angle decreases, as does its discrepancy near the wall, $y = 0$. Hence, the wall effect surpasses the main flow as a more significant influence and thus the eddy-resolving method is necessary when predicting boundary layers around blade tips in this scenario.

7.4 Acceleration and Discrepancies

All of the previous cases show a trend such that, if the acceleration parameter is higher, the turbulence is less influential on the predicted results. It should be noted that the maxima of the two parameters K and $\Delta\theta$ are usually around the casing, hence they may severely affect fan performance at the tip and change the tip leakage flows significantly. Figure 7.6 plots the maximum of the discrepancy in $\Delta\theta$ at the casing with increasing acceleration parameter for all the test cases with varying fan-locations and beam-heights.

The black line with square symbols connects the results for the fan installed at different locations. It shows that the flow acceleration can significantly reduce the error associated with the RANS approach. For the case with the original fan location, a strong acceleration is observed. The difference between the RANS and LES is marginal. The extreme case is such that the substantial flow acceleration can lead to the same predictions between the RANS and LES models. Hence, when close to this situation, the RANS model may be sufficient for separation prediction. The red line with circular symbols denotes the difference in the incidence angles on the casing for the cases with different beams. Similarly, the discrepancies decreases when the flow acceleration is stronger.

The reduction of the discrepancies between the RANS and LES models also indicates that, with sufficient acceleration, the main flow determines the predicted results and can significantly affect the turbulence, whereas the turbulence effect is very limited.

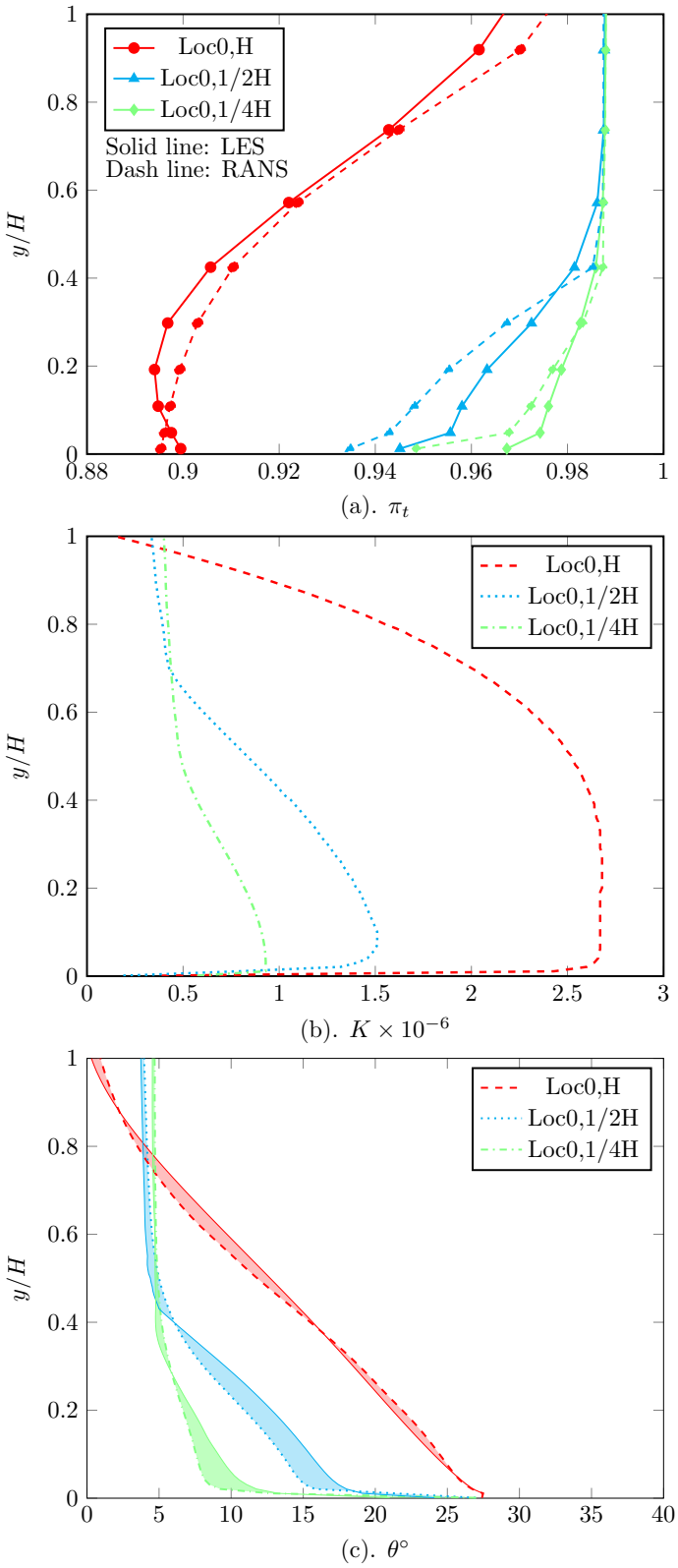

Fig. 7.5 Radial distributions of (a) total pressure ratio (b) acceleration parameter (c) angle of incidence predicted by RANS and LES at x = 4.5H. Cases compared for same fan location, 'Loc0' and varying beam heights: H, H/2, H/4.

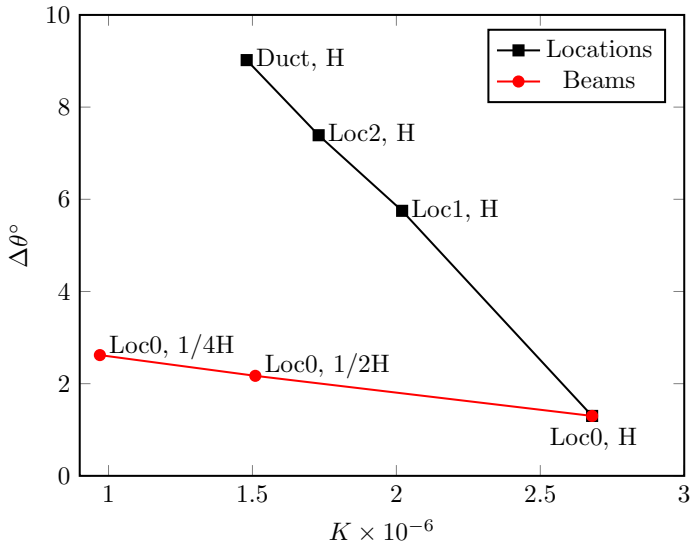

Fig. 7.6 Variation of maximum discrepancy in the incidence angle $\Delta\theta^\circ$ (typically observed at the casing) with acceleration parameter for all the test cases with varying fan-locations and beam heights

Figure 7.7 shows that when the fan is installed at the original location, it dominates the main flow and the TKE profiles are very similar, despite a slight deviation in the distributions.

The effect of turbulence can be further examined by comparing a case with a lower Reynolds number. The flow for the present case is at $Re = 1 \times 10^6$ and the additional case is defined by increasing the viscosity by an order of magnitude, thus $Re = 1 \times 10^5$. Only Figure 7.8 depicts the velocity and TKE profiles for both cases (with higher and lower viscosity). The TKE for the flow with the lower Reynolds number (blue curve) is slightly weaker around the shear layer $y = H$ and near the wall. Although this weakened turbulence changes the velocity profile at $x = H$ and near the wall, it does not affect any other areas. Hence, this explicitly demonstrates that the turbulence does not have a strong impact on the forced separated flow.

7.5 Concluding Remarks

This chapter investigated the discrepancies between RANS and LES in the presence of a downstream fan. The downstream fan can affect the mass flow redistribution and accelerates the flow at the casing relative to the hub. Thus we investigated the consequence of this acceleration on the RANS-LES discrepancies using a mixed fidelity method. This was achieved by applying the mixed-fidelity method to the same case set

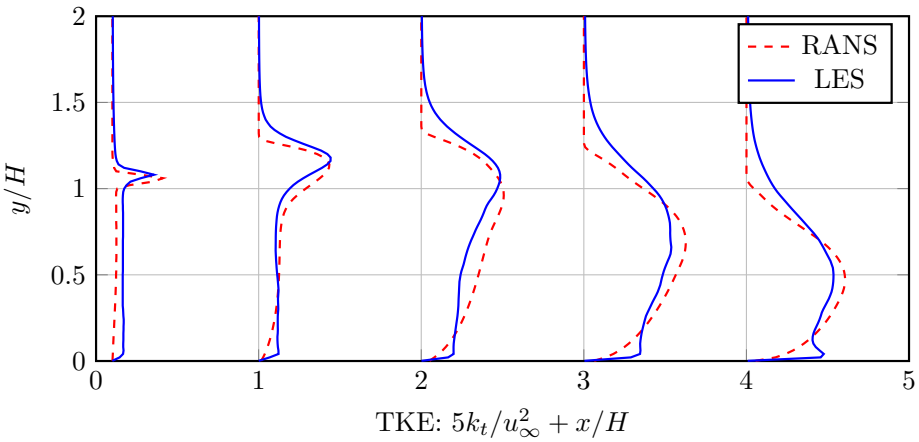

Fig. 7.7 Carpet plot comparing the prediction of TKE from LES against k-omega SST model for case Loc0, H

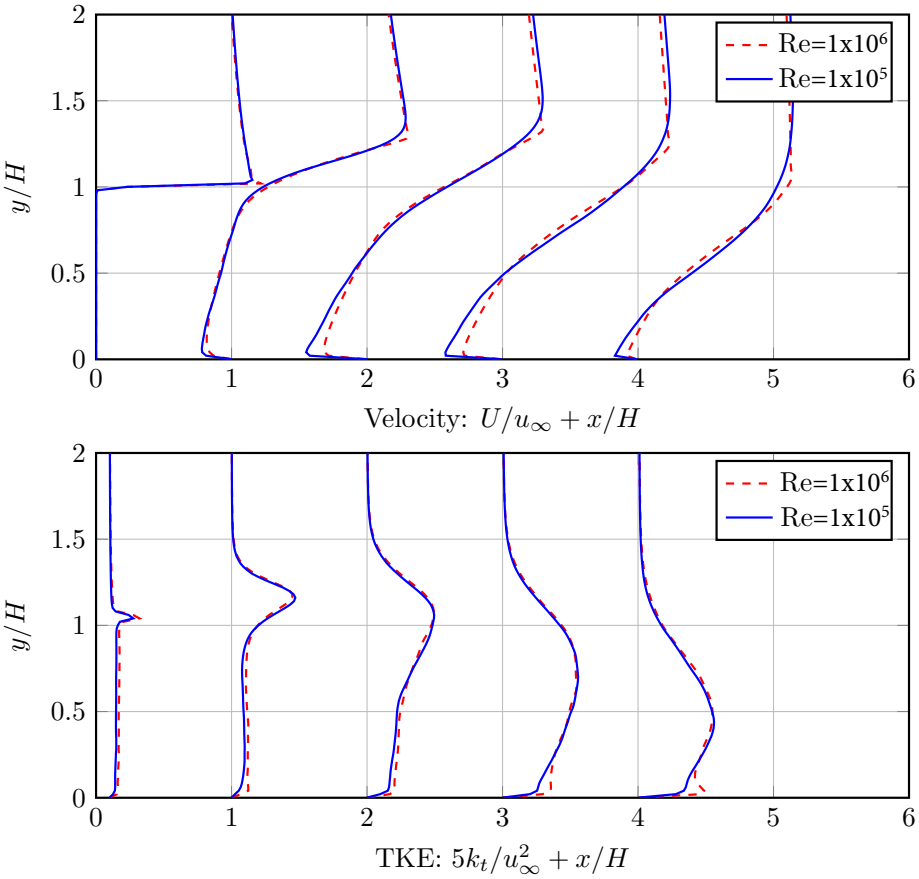

Fig. 7.8 Carpet plot showing LES predictions of (a) velocity profiles and (b) TKE profiles at two different Reynolds numbers for case Loc0, H

in Chapter 6, but running with both RANS and LES. These cases are essentially with various flow accelerations, which were altered by (1) installing a fan in the downstream, (2) varying fan proximity in the downstream of a given distortion generator, and (3) varying heights of the distortion generator with the originally located fan.

In the "absence of fan", the discrepancies between RANS and LES is significant within the separation and reattachment region, due to the well-known limitations of the standard RANS models. Interestingly, the current study showed that "with the fan installed", the deviation between RANS and LES decreases substantially. Specifically, the deviation is minimal when the proximity of the fan is closest to the separation. It implies that with an installed fan, the inaccuracies of turbulence models are mitigated by the strong flow acceleration at the casing due to the fan. More precisely, the mass flow redistribution due to the fan has a dominant effect on the final predictions and the effect of turbulence model becomes secondary, thereby suggesting that high fidelity eddy resolving simulations like LES provide marginal improvement to the accuracy for the short intake case. These results are particularly important for the short intake-fan strategies with fan getting closer to intake lip.

Chapter 8

Conclusions

8.1 Mixed-fidelity Method

This thesis proposed a mixed-fidelity method that combines techniques with different fidelities in the hierarchy of turbulence modelling and geometry modelling. That is, higher fidelity methods for flows with complex turbulence and lower fidelity models for providing surrounding boundary conditions. The method contains a range of combinations catering to various applications among aerodynamics, aeroacoustics, etc. It can be a very promising tool to capture multiscale turbulence in complex flows for industrial high-fidelity simulations. The benefits are no moving boundaries and mixing planes, less efforts for mesh generation and lower computing costs.

Combinations in this mixed-fidelity framework include but are not limited to RANS+IBM, LES+IBM, RANS+eIBM(g/l), LES+eIBM(g/l). In the thesis, they were applied to the investigation of fan-intake interaction. Previous research has demonstrated the application of RANS+IBM in both 2D and 3D flows with a range of Reynolds numbers. Hence, the thesis started with the validation of eIBM with both global force and local force. First, RANS+eIBM was tested on a Darmstadt Transonic Rotor and showed its capability for providing proper boundary conditions for both upstream and downstream region. Both eIBM with local force and global force were examined and compared with the experiment and DMR case. Results showed that the eIBM(g/l) was able to capture flow features of distortion transfer through rotor and stator. At the rotor inlet, exit and stator exit, the total pressure distributions generally agreed well with the experimental data. The trend of the distortion development in the axial direction could be captured and the total pressure ratio approximated. Specifically, the eIBMl was shown to approximate the main flow features and intermittency around finite blades, including static/total pressure, Ma

number and tip leakage. It also reproduced sources of sound and wave propagation, and captured the frequencies of blade passing and vortex shedding. By contrast, the eIBMg smears blade geometry and hence flow variables are circumferentially averaged. Although flow details may be missing within blade passages, the approach indeed can characterise flow between the fan and intake in the axial and radial directions. Considering it has less demanding computational requirements, this method can be used as an efficient tool for fan design when circumferential features are less important and can be ignored, for example, the investigation of axial or radial influences. Then LES+IBM was also validated for flows around a static triangular prism. Results against the experiment and DMR case demonstrated that the method is able to provide similar flow solutions in terms of main flow variables and high-order turbulence statistics.

8.2 Fan-intake Interaction

After validating RANS+eIBMg and URANS+IBM, the method was upgraded to LES+eIBM with global force to study the mechanism of fan influence on intake distortion, focusing on axial and radial impacts. A 30° sector derived from original case was chosen and examined between the cases with fan and without fan. It was found that there are both direct and indirect effects of a fan that can suppress the inlet distortion. (a) The suction effect of the fan accelerates the flow in the intake and changes the streamline curvature. This change closes the recirculation bubble much earlier and alleviates the undesired distortion directly. (b) In addition, within the recirculation region, the strain rate and turbulence transport are intensified. The enhanced turbulence in the vicinity of the fan feeds back into the initial growth of the shear layer by means of the recirculating flow. This indirect feedback is found to increase the turbulence production and the spreading rate of the shear layer.

The direct effect was further investigated via some parametric studies of fan design. It was found that the type and location of fan have a significant influence on intake distortion. A tip-loaded fan tend to suppress more the separation and hence alleviate distortion better than the original hub-loaded blade. Also, the nearer the downstream fan, the stronger the influence in terms of suppressing separation. The fan at the proposed location can recover 45% of the loss. This is because the rotational fan can accelerate the upstream flow at the casing, and hence reduce the separation bubble and alleviate the distortion. Finally, fan influence on various distortions are studied by changing the beam height. Results demonstrate that although the original beam has such a significant influence that even the main flow can be changed by almost 20%,

the fan can still weaken the distortions. When the distortion is greater, the fan has a stronger effect. This change is non-linear, and when the beam height is reduced to $H/4$, the Recovery Factor becomes $RF/7$. This means that a well-designed blade could show substantial power when dealing with a range of possible intake distortion. Hence, the fan could form an essential component for intake distortion control.

The fan influence via turbulence was also examined by comparing to the results from RANS+eIBM. This comparison also help to understand whether direct or indirect effect dominates the process, and hence may determine the choice of turbulence simulations. The investigation were conducted on the same set of cases with different fan locations and beam heights. Velocity profiles were compared between RANS and LES. It was found that in the absence of fan, the discrepancies between RANS and LES is significant within the separation and reattachment region, due to the well-known limitations of the standard RANS models. Interestingly, when the fan is installed downstream, the deviation decreases substantially and is minimal when the proximity of the fan is closest to the separation. This implies that with such fan influence, the inaccuracies of turbulence models are mitigated by the strong flow acceleration. This acceleration comes from the mass flow redistribution due to the fan and has a dominant effect on separation predictions. By contrast, the effect of turbulence model becomes secondary, implying that high fidelity simulations like LES provide a very marginal improvement to the prediction of separation with a strong fan impact. These results are particularly important for the short intake-fan strategies in which fan is much closer to intake lip and hence conventional turbulence models are capable of predicting separated flows.

8.3 Future Work

The present research developed a range of techniques within the mixed-fidelity framework and applied them to the simulation of fan-intake interaction. These techniques showed a good performance in the region between fan and intake. However, as mentioned in Chapter 4, discrepancies in blade wakes still exists in the downstream fan due to the lack of proper resolution of blade boundary layers. Hence, at the next stage the eIBMl will be improved by implementing some models for blade boundary layer. A possible way is to add a term $f(d_w)$ shown in Eq.8.1

$$\mathcal{F}(\boldsymbol{x}, t) = f(d_w)H(R_b - r)\sum_{n=0}^{\infty} a_n cos(\theta + \theta_0 + \Omega t), \tag{8.1}$$

which defines a 'pseudo-layer' (Fig.8.1) where velocities can gradually increase from zero on blade boundaries to main flow velocity. In the blade zone, the velocity will be strictly zero by imposing standard IBM. Hence, the whole dynamic process around blades could be that in the blade zone, the parallel velocity is controlled by

$$f_p^{l+1/2} = -RHS_p^l + \rho \frac{V_p^{l+1} - u_p^l}{\partial t}, \tag{8.2}$$

whereas in both blade zone and pseudo layer zone, the normal velocity is governed by

$$f_n^{l+1/2} = -RHS_n^l + \rho \frac{V_n^{l+1} - u_n^l}{\partial t}. \tag{8.3}$$

Then blade wakes could be calibrated by choosing a proper region or function $f(d_w)$

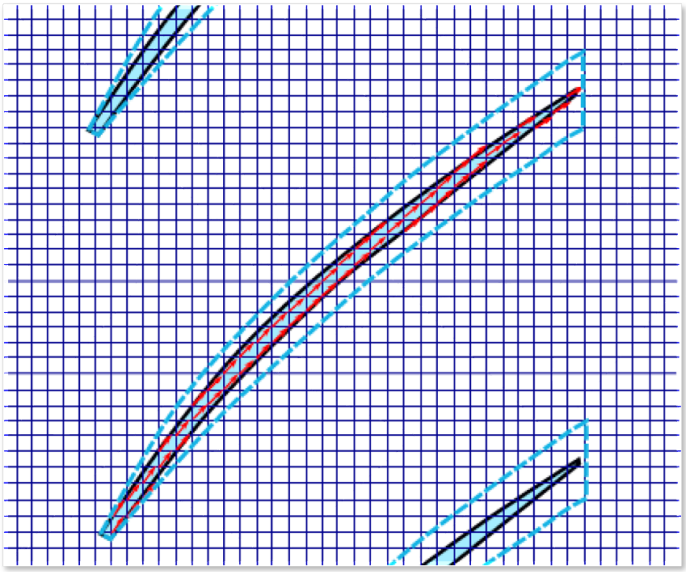

Fig. 8.1 Modelling for a pseudo layer around fan blades

for the 'pseudo-layer'. With this improved model, a promising application could be the prediction of jet noise. Figure 8.2 shows the sketch of this scenario. In the upstream of a nozzle, OGVs, A-frame, Gearbox shaft, etc. will be replaced by IBM or eIBMl, which help reduce mesh size significantly within the blade region and thus make high-fidelity simulation for downstream jet flows possible.

This mixed-fidelity method does not only improve the prediction of complex flows but may also provide some insights for understanding flow physics around complex geometries. Figure 8.3 shows a typical static blade with tip clearance at the bottom. To understand how the angle of attack at blade leading edge affects the corner separation

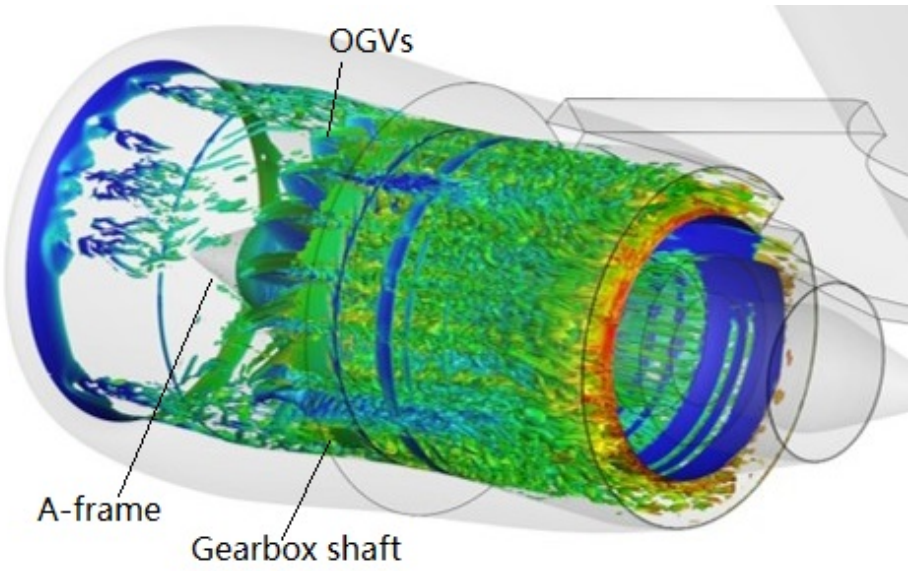

Fig. 8.2 Sketch for the prediction of jet noise, from Tyacke [154]

induced by this tip clearance, a test case with 4° inlet flow angle was set. In this test rig, a typical way to trigger turbulent boundary layer is to install some trips at the casing of inlet and blade leading edge. To save computational costs and make mesh generation easier, these trips can be modelled rather than resolved by standard IBM. Hence, running LES+IBM can provide abundant flow details and some high-order turbulence statistics, such as TKE production, dissipation, diffusion, transport, etc. These terms will greatly help reveal the mechanism of inlet flow influence on corner vortices, provide instructions for separation control and improve current turbulence models. However, clearly boundary layer resolution is an issue and poses limitations.

In addition, it should also be noted that the eIBMl in mixed-fidelity modelling is still only available for engines at design points. The flow at fan blade trailing edge is controlled by the blade angle. This means the model will probably fail to simulate flows with high angles of attack at off-design points (e.g., near stall point). This problem could be tackled by adding a deviation model calibrated by the data from an efficiency map.

In total, this mixed-fidelity method can be further refined in the above ways and hence significantly improve the quality of numerical simulations for 3D designs or systematic optimisation at the final stage of a whole design process (Fig.8.4).

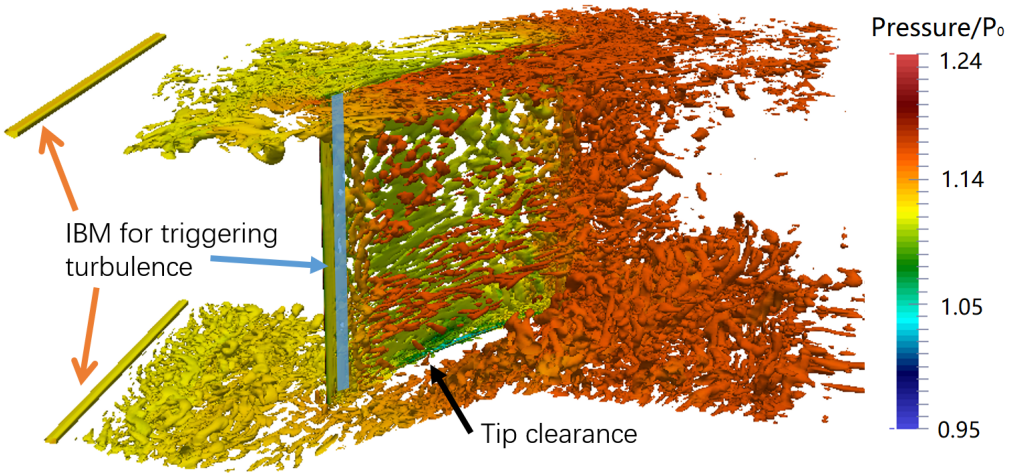

Fig. 8.3 Q-criterion for studies of blade tip clearance

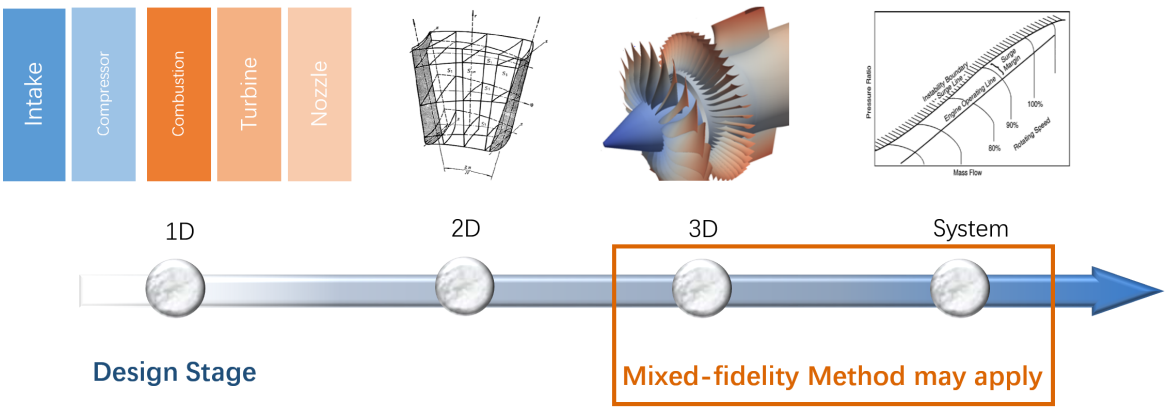

Fig. 8.4 Typical design process of aero-engines

References

[1] Abe, K. (2005). A hybrid les/rans approach using an anisotropy-resolving algebraic turbulence model. *International Journal of Heat and Fluid Flow*, 26(2):204–222.

[2] Abid, R., VATSA, V., JOHNSON, D., and WEDAN, B. (1989). Prediction of separated transonic wing flows with a non-equilibrium algebraic model. In *27th Aerospace Sciences Meeting*, page 558.

[3] ACARE (2017). Strategic research and innovation agenda. https://www.acare4europe.org/sites/acare4europe.org/files/document/ACARE-Strategic-Research-Innovation-Volume-1.pdf.

[4] Agrwal, N., Dutta, S., and Gandhi, B. (2016). Experimental investigation of flow field behind triangular prisms at intermediate reynolds number with different apex angles. *Experimental Thermal and Fluid Science*, 72:97–111.

[5] Alam, M. and Sandham, N. D. (2000). Direct numerical simulation of 'short'laminar separation bubbles with turbulent reattachment. *Journal of Fluid Mechanics*, 410:1–28.

[6] Arthurs, K. M., Moore, L. C., Peskin, C. S., Pitman, E. B., and Layton, H. (1998). Modeling arteriolar flow and mass transport using the immersed boundary method. *Journal of Computational Physics*, 147(2):402–440.

[7] Baldwin, B. and Lomax, H. (1978). Thin-layer approximation and algebraic model for separated turbulentflows. In *16th aerospace sciences meeting*, page 257.

[8] Banerjee, S., Krahl, R., Durst, F., and Zenger, C. (2007). Presentation of anisotropy properties of turbulence, invariants versus eigenvalue approaches. *Journal of Turbulence*, (8):N32.

[9] Bardino, J., Ferziger, J. H., and Reynolds, W. C. (1983). Improved turbulence models based on large eddy simulation of homogeneous, incompressible turbulent flows.

[10] Barthmes, S., Haug, J. P., Lesser, A., and Niehuis, R. (2016). Unsteady cfd simulation of transonic axial compressor stages with distorted inflow. In *Advances in Simulation of Wing and Nacelle Stall*, pages 303–321. Springer.

[11] Basdevant, C. and Sadourny, R. (1984). Numerical solution of incompressible flow: the mask method. *Lab di Meteorologie Dynamique, Ecole Normale Superieure, Paris (unpublished)*.

[12] Batten, P., Craft, T., Leschziner, M., and Loyau, H. (1999). Reynolds-stress-transport modeling for compressible aerodynamics applications. *AIAA journal*, 37(7):785–797.

[13] Bentaleb, Y., Lardeau, S., and Leschziner, M. A. (2012). Large-eddy simulation of turbulent boundary layer separation from a rounded step. *Journal of Turbulence*, (13):N4.

[14] Beyer, R. P. and LeVeque, R. J. (1992). Analysis of a one-dimensional model for the immersed boundary method. *SIAM Journal on Numerical Analysis*, 29(2):332–364.

[15] BILGER, R. (1975). A note on favre averaging in variable density flows. *Combustion Science and Technology*, 11(5-6):215–217.

[16] Bitter, M., Wartzek, F., Übelacker, S., Schiffer, H.-P. K., and Christian, J. (2015). Characterization of a distorted transonic compressor flow using dual-luminophore pressure-sensitive paint. In *10th Pacific Symposium on Flow Visualization and Image Processing (PSFVIP-10), fedOA (Federico II Open Archive), Naples, Italy*.

[17] Boris, J., Grinstein, F., Oran, E., and Kolbe, R. (1992). New insights into large eddy simulation. *Fluid dynamics research*, 10(4-6):199–228.

[18] Boris, J. P. (1990). On large eddy simulation using subgrid turbulence models comment 1. In *Whither turbulence? Turbulence at the crossroads*, pages 344–353. Springer.

[19] Bosch, G. and Rodi, W. (1998). Simulation of vortex shedding past a square cylinder with different turbulence models. *International journal for numerical methods in fluids*, 28(4):601–616.

[20] Bradshaw, P. (1973). Effects of streamline curvature on turbulent flow. Technical report, DTIC Document.

[21] Bradshaw, P. (1974). Possible origin of prandt's mixing-length theory. *Nature*, 249(5453):135.

[22] Breuer, M. (2002). *Direkte Numerische Simulation und Large-Eddy-Simulation turbulenter Strömungen auf Hochleistungsrechnern*. Shaker.

[23] Briscolini, M. and Santangelo, P. (1989). Development of the mask method for incompressible unsteady flows. *Journal of Computational Physics*, 84(1):57–75.

[24] Brodkey, R. S. (1995). *The phenomena of fluid motions*. Courier Corporation.

[25] Burchard, H. and Deleersnijder, E. (2001). Stability of algebraic non-equilibrium second-order closure models. *Ocean Modelling*, 3(1-2):33–50.

[26] Callahan, G. M. and Stenning, A. (1971). Attenuation of inlet flow distortion upstream of axial flow compressors. *Journal of Aircraft*, 8(4):227–233.

[27] Cao, T., Hield, P., and Tucker, P. G. (2016). Hierarchical immersed boundary method with smeared geometry. In *54th AIAA Aerospace Sciences Meeting*, volume 33, page 2130.

[28] Cao, T., Vadlamani, N. R., Tucker, P. G., Smith, A. R., Slaby, M., and Sheaf, C. T. (2017). Fan–intake interaction under high incidence. *Journal of Engineering for Gas Turbines and Power*, 139(4):041204.

[29] Chima, R. V. (2006). A three-dimensional unsteady cfd model of compressor stability. In *ASME Turbo Expo 2006: Power for Land, Sea, and Air*, pages 1157–1168. American Society of Mechanical Engineers.

[30] Chou, P. Y. (1945). On velocity correlations and the solutions of the equations of turbulent fluctuation. *Quarterly of Applied Mathematics*, 3(1):38–54.

[31] Chow, F. K. and Moin, P. (2003). A further study of numerical errors in large-eddy simulations. *Journal of Computational Physics*, 184(2):366–380.

[32] Clarke, D. K., Hassan, H., and Salas, M. (1986). Euler calculations for multielement airfoils using cartesian grids. *AIAA journal*, 24(3):353–358.

[33] Craft, T., Launder, B., and Suga, K. (1997). Prediction of turbulent transitional phenomena with a nonlinear eddy-viscosity model. *International Journal of Heat and Fluid Flow*, 18(1):15–28.

[34] Crumpton, P., Moinier, P., and Giles, M. (1997). An unstructured algorithm for high reynolds number flows on highly stretched grids. *Numerical methods in laminar and turbulent flow*, pages 561–572.

[35] Defoe, J., Narkaj, A., and Spakovszky, Z. (2009). A novel mpt noise prediction methodology for highly-integrated propulsion systems with inlet flow distortion.

[36] Defoe, J. J. and Spakovszky, Z. S. (2013). Effects of boundary-layer ingestion on the aero-acoustics of transonic fan rotors. *ASME J. Turbomach.*, 135(5):051013.

[37] Delville, J., Cordier, L., and Bonnet, J.-P. (1998). Large-scale-structure identification and control in turbulent shear flows. In *Flow Control*, pages 199–273. Springer.

[38] Diurno, G. V., Balaras, E., and Piomelli, U. (2001). Wall-layer models for les of separated flows. *Modern simulation strategies for turbulent flows*, pages 157–174.

[39] Du, L., Sun, X., and Yang, V. (2015). Generation of vortex lift through reduction of rotor/stator gap in turbomachinery. *Journal of Propulsion and Power*, 32(2):472–485.

[40] Dunham, J. (1965). Non-axisymmetric flows in axial compressors. *Mechanical Engineering Science Monograph, MESM*.

[41] Eastwood, S. J. and Tucker, P. G. (2011). Hybrid les—rans of complex geometry jets. *International Journal of Aeroacoustics*, 10(5-6):659–684.

[42] Eastwood, S. J., Tucker, P. G., Xia, H., and Klostermeier, C. (2009). Developing large eddy simulation for turbomachinery applications. *Philosophical Transactions of the Royal Society A: Mathematical, Physical and Engineering Sciences*, 367(1899):2999–3013.

[43] Emory, M. A. (2014). *Estimating model-form uncertainty in Reynolds-averaged Navier-Stokes closures*. PhD thesis.

[44] Fadlun, E., Verzicco, R., Orlandi, P., and Mohd-Yusof, J. (2000). Combined immersed-boundary finite-difference methods for three-dimensional complex flow simulations. *Journal of computational physics*, 161(1):35–60.

[45] Ferziger, J. (1993). Subgrid-scale modeling.

[46] Ferziger, J. H. and Peric, M. (2012). *Computational methods for fluid dynamics*. Springer Science & Business Media.

[47] Fidalgo, V. J., Hall, C., and Colin, Y. (2012). A study of fan-distortion interaction within the nasa rotor 67 transonic stage. *ASME J. Turbomach.*, 134(5):051011.

[48] Freund, J. B. (2001). Noise sources in a low-reynolds-number turbulent jet at mach 0.9. *Journal of Fluid Mechanics*, 438:277–305.

[49] Fritsch, G. and Giles, M. (1992). Second-order effects of unsteadiness on the performance of turbomachines. In *ASME 1992 International Gas Turbine and Aeroengine Congress and Exposition*, pages V001T01A130–V001T01A130. American Society of Mechanical Engineers.

[50] Fröhlich, J., Mellen, C. P., Rodi, W., Temmerman, L., and Leschziner, M. A. (2005). Highly resolved large-eddy simulation of separated flow in a channel with streamwise periodic constrictions. *Journal of Fluid Mechanics*, 526:19–66.

[51] Fureby, C., Knight, D. D., and Kupiainen, M. (2007). 11 compressible turbulent shear flows. *Implicit large eddy simulation: computing turbulent fluid dynamics*, page 329.

[52] Gao, F., Ma, W., Boudet, J., Ottavy, X., Lu, L., and Lebœuf, F. (2013). Numerical analysis of three-dimensional corner separation in a linear compressor cascade. In *ASME Turbo Expo 2013: Turbine Technical Conference and Exposition*, pages V06AT35A038–V06AT35A038. American Society of Mechanical Engineers.

[53] Gao, Y., Liu, Y., Zhong, L., Hou, J., and Lu, L. (2016). Study of the standard k-ε model for tip leakage flow in an axial compressor rotor. *International Journal of Turbo & Jet-Engines*, 33(4):353–360.

[54] Gatski, T. and Rumsey, C. (2002). Linear and nonlinear eddy viscosity models. *Closure strategies for turbulent and transitional flows*, pages 9–46.

[55] Germano, M., Piomelli, U., Moin, P., and Cabot, W. H. (1991). A dynamic subgrid-scale eddy viscosity model. *Physics of Fluids A: Fluid Dynamics*, 3(7):1760–1765.

[56] Ghosal, S. (1996). An analysis of numerical errors in large-eddy simulations of turbulence. *Journal of Computational Physics*, 125(1):187–206.

[57] Goldstein, D., Handler, R., and Sirovich, L. (1993). Modeling a no-slip flow boundary with an external force field. *Journal of Computational Physics*, 105(2):354–366.

[58] Gong, Y., Tan, C., Gordon, K., and Greitzer, E. (1998). A computational model for short wavelength stall inception and development in multi-stage compressors. In *ASME 1998 International Gas Turbine and Aeroengine Congress and Exhibition*, pages V001T01A114–V001T01A114. American Society of Mechanical Engineers.

[59] Gordon, K. A. (1999). *Three-dimensional rotating stall inception and effects of rotating tip clearance asymmetry in axial compressors*. PhD thesis, Massachusetts Institute of Technology.

[60] Gourdain, N., Gicquel, L. Y., and Collado, E. (2012). Comparison of rans and les for prediction of wall heat transfer in a highly loaded turbine guide vane. *Journal of propulsion and power*, 28(2):423–433.

[61] Grinstein, F. and Guirguis, R. (1992). Effective viscosity in the simulation of spatially evolving shear flows with monotonic fct models. *Journal of Computational Physics*, 101(1):165–175.

[62] Grinstein, F. F., Margolin, L. G., and Rider, W. J. (2007). *Implicit large eddy simulation: computing turbulent fluid dynamics*. Cambridge university press.

[63] Haase, W., Braza, M., and Revell, A. (2009). *DESider–A European Effort on Hybrid RANS-LES Modelling: Results of the European-Union Funded Project, 2004-2007*, volume 103. Springer Science & Business Media.

[64] Hah, C., Bergner, J., and Schiffer, H.-P. (2006). Short length-scale rotating stall inception in a transonic axial compressor: criteria and mechanisms. In *ASME turbo expo 2006: Power for land, sea, and air*, pages 61–70. American Society of Mechanical Engineers.

[65] Harten, A. (1983). High resolution schemes for hyperbolic conservation laws. *Journal of computational physics*, 49(3):357–393.

[66] Hasan, K. M., Basser, P. J., Parker, D. L., and Alexander, A. L. (2001). Analytical computation of the eigenvalues and eigenvectors in dt-mri. *Journal of Magnetic Resonance*, 152(1):41–47.

[67] He, C., Ma, Y., Liu, X., Sun, D., and Sun, X. (2018). Aerodynamic instabilities of swept airfoil design in transonic axial-flow compressors. *AIAA Journal*, pages 1–16.

[68] Hodson, H. (1998). Blade row interactions in low pressure turbines. *Lecture series-van Kareman Institute for fluid dynamics*, 2:A1–A124.

[69] Horlock, J. H. (1978). Actuator disk theory-discontinuities in thermo-fluid dynamics. *New York, McGraw-Hill International Book Co., 1978. 256 p.*

[70] Hu, G., Du, L., and Sun, X. (2014). An immersed boundary method for simulating an oscillating airfoil. In *Fluid-Structure-Sound Interactions and Control*, pages 343–349. Springer.

[71] Hu, G., Du, L., Zhong, G., and Sun, X. (2011). A numerical modeling of the vortex-induced vibration of cascade in turbomachinery using immersed boundary method. *journal of thermal science*, 20(3):229.

[72] Iaccarino, G. and Verzicco, R. (2003). Immersed boundary technique for turbulent flow simulations. *Applied Mechanics Reviews*, 56(3):331–347.

[73] Jiang, Y., Wang, X., Jing, X., and Sun, X. (2014). A study of three-dimensional acoustic scattering by arbitrary distribution multibodies using extended immersed boundary method. *Journal of Vibration and Acoustics*, 136(3):034505.

[74] Johansson, S. H., Davidson, L., and Olsson, E. (1993). Numerical simulation of vortex shedding past triangular cylinders at high reynolds number using a k-ε turbulence model. *International Journal for Numerical Methods in Fluids*, 16(10):859–878.

[75] Jones, W. and Launder, B. E. (1972). The prediction of laminarization with a two-equation model of turbulence. *International journal of heat and mass transfer*, 15(2):301–314.

[76] Kato, M. (1993). The modelling of turbulent flow around stationary and vibrating square cylinders. *Turbulent Shear Flow*, 1:10–4.

[77] Keetels, G. H., D'Ortona, U., Kramer, W., Clercx, H. J., Schneider, K., and van Heijst, G. J. (2007). Fourier spectral and wavelet solvers for the incompressible navier–stokes equations with volume-penalization: Convergence of a dipole–wall collision. *Journal of Computational Physics*, 227(2):919–945.

[78] Kim, S., Pullan, G., and Hall, C. (2018). Stall inception in low pressure ratio fans. In *ASME Turbo Expo 2018: Turbine Technical Conference and Exposition, Lillestrom, Norway, No. GT2018-75153*, number No. GT2018-75153. American Society of Mechanical Engineers.

[79] Klostermeier, C. (2008). *Investigation into the capability of large eddy simulation for turbomachinery design*. PhD thesis, University of Cambridge.

[80] Lapworth, L. (2004). Hydra-cfd: a framework for collaborative cfd development. In *International Conference on Scientific and Engineering Computation (IC-SEC), Singapore, June*, volume 30.

[81] Lardeau, S. and Leschziner, M. (2005). Unsteady rans modelling of wake–blade interaction: computational requirements and limitations. *Computers & Fluids*, 34(1):3–21.

[82] Larsson, J. and Wang, Q. (2014). The prospect of using large eddy and detached eddy simulations in engineering design, and the research required to get there. *Philosophical Transactions of the Royal Society of London A: Mathematical, Physical and Engineering Sciences*, 372(2022):20130329.

[83] Launder, B. E. and Jones, W. P. (1969). *On the prediction of laminarisation*. HM Stationery Office.

[84] Leschziner, M. A. (2000). Turbulence modelling for separated flows with anisotropy-resolving closures. *Philosophical Transactions of the Royal Society of London. Series A: Mathematical, Physical and Engineering Sciences*, 358(1777):3247–3277.

[85] Lesser, A., Schulze, S., Niehuis, R., Kähler, C., and Lieser, J. (2013). Analytical design of an inlet distortion generator and its experimental and numerical validation. In *New Results in Numerical and Experimental Fluid Mechanics VIII*, pages 33–41. Springer.

[86] Liang, A., Jing, X., and Sun, X. (2008). Constructing spectral schemes of the immersed interface method via a global description of discontinuous functions. *Journal of Computational Physics*, 227(18):8341–8366.

[87] Lieser, J., Biela, C., Pixberg, C., Schiffer, H.-P., Schulze, S., Lesser, A., Kähler, C., and R, N. (2011). Compressor rig test with distorted inflow using distortion generators.

[88] Lilly, D. K. (1992). A proposed modification of the germano subgrid-scale closure method. *Physics of Fluids A: Fluid Dynamics*, 4(3):633–635.

[89] LIU, X., SUN, D., SUN, X., and WANG, X. (2012). Flow stability model for fan/compressors with annular duct and novel casing treatment. *Chinese Journal of Aeronautics*, 25(2):143–154.

[90] Liu, Y., Lu, L., Fang, L., and Gao, F. (2011). Modification of spalart–allmaras model with consideration of turbulence energy backscatter using velocity helicity. *Physics Letters A*, 375(24):2377–2381.

[91] Liu, Y., Yan, H., Liu, Y., Lu, L., and Li, Q. (2016). Numerical study of corner separation in a linear compressor cascade using various turbulence models. *Chinese Journal of Aeronautics*, 29(3):639–652.

[92] Liu, Y., Yan, H., Lu, L., and Li, Q. (2017). Investigation of vortical structures and turbulence characteristics in corner separation in a linear compressor cascade using ddes. *Journal of Fluids Engineering*, 139(2):021107.

[93] Liu, Y., Yu, X., and Liu, B. (2008). Turbulence models assessment for large-scale tip vortices in an axial compressor rotor. *Journal of Propulsion and Power*, 24(1):15.

[94] Loiodice, S., Tucker, P., and Watson, J. (2010). Modeling of coupled open rotor engine intakes. In *48th AIAA Aerospace Sciences Meeting Including the New Horizons Forum and Aerospace Exposition*, page 840.

[95] Longley, J. and Greitzer, E. (1992). Inlet distortion effects in aircraft propulsion system integration.

[96] Longley, J. P. and Greitzer, E. M. (1993). Inlet distortion effects in aircraft propulsion system integration. In *AGARD Lecture Series in Fundamentals and Special Problems of Synthetic Aperture Radar (SAR)*, pages AGARD LS–183.

[97] Ma, Y., Cui, J., Vadlamani, N. R., and Tucker, P. (2018). Effect of fan on inlet distortion: A mixed-fidelity approach. *AIAA J.*

[98] Maertens, A. P. and Weymouth, G. D. (2015). Accurate cartesian-grid simulations of near-body flows at intermediate reynolds numbers. *Computer Methods in Applied Mechanics and Engineering*, 283:106–129.

[99] Majumdar, S., Iaccarino, G., and Durbin, P. (2001). Rans solvers with adaptive structured boundary non-conforming grids. *Annual Research Briefs, Center for Turbulence Research, Stanford University*, pages 353–466.

[100] Marble, F. E. (1964). Three-dimensional flow in turbomachines. *High Speed Aerodynamics and Jet Propulsion*, 10:83–166.

[101] Martinelli, L. (1987). Calculations of viscous flows with a multigrid method. Technical report, Princeton Univ., NJ (USA).

[102] Mayle, R. E. (1991). The role of laminar-turbulent transition in gas turbine engines. In *ASME 1991 International Gas Turbine and Aeroengine Congress and Exposition*, pages V005T17A001–V005T17A001. American Society of Mechanical Engineers.

[103] Mazzawy, R. S. (1977). Multiple segment parallel compressor model for circumferential flow distortion. *Journal of Engineering for Power*, 99(2):288–296.

[104] Meinke, M., Schröder, W., Krause, E., and Rister, T. (2002). A comparison of second-and sixth-order methods for large-eddy simulations. *Computers & Fluids*, 31(4-7):695–718.

[105] Menter, F. R., Kuntz, M., and Langtry, R. (2003). Ten years of industrial experience with the sst turbulence model. *Turbulence, heat and mass transfer*, 4(1):625–632.

[106] Mittal, R., Bonilla, C., and Udaykumar, H. (2003). Cartesian grid methods for simulating flows with moving boundaries. *Computational Methods and Experimental Measurements-XI*, pages 557–566.

[107] Mittal, R. and Iaccarino, G. (2005). Immersed boundary methods. *Annu. Rev. Fluid Mech.*, 37:239–261.

[108] Mittal, R., Utturkar, Y., and Udaykumar, H. (2002). Computational modeling and analysis of biomimetic flight mechanisms. In *40th AIAA Aerospace Sciences Meeting & Exhibit*, page 865.

[109] Mohd-Yusof, J. (1997). Combined immersed boudaries/b-splines methods for simulations in complex geometries, ctr annual research briefs, nasa ames.

[110] Moin, P., Squires, K., Cabot, W., and Lee, S. (1991). A dynamic subgrid-scale model for compressible turbulence and scalar transport. *Physics of Fluids A: Fluid Dynamics*, 3(11):2746–2757.

[111] Moinier, P. (1999). *Algorithm developments for an unstructured viscous flow solver*. PhD thesis, Oxford University.

[112] Nicoud, F. and Ducros, F. (1999). Subgrid-scale stress modelling based on the square of the velocity gradient tensor. *Flow, turbulence and Combustion*, 62(3):183–200.

[113] Nicoud, F., Toda, H. B., Cabrit, O., Bose, S., and Lee, J. (2011). Using singular values to build a subgrid-scale model for large eddy simulations. *Physics of Fluids*, 23(8):085106.

[114] Niehuis, R., Lesser, A., Probst, A., Radespiel, R., Schulze, S., Kähler, C., Spiering, F., and Kroll, N. (2013). Simulation of nacelle stall and engine response.

[115] Olsen, M. and Coakley, T. (2001). The lag model, a turbulence model for non equilibrium flows. In *15th AIAA Computational Fluid Dynamics Conference*, page 2564.

[116] Pearson, H. and McKenzie, A. (1959). Wakes in axial compressors. *The Aeronautical Journal*, 63(583):415–416.

[117] Perovic, D., Hall, C. A., and Gunn, E. J. (2015). Stall inception in a boundary layer ingesting fan. In *ASME Turbo Expo 2015: Turbine Technical Conference and Exposition*, pages V02AT37A031–V02AT37A031. American Society of Mechanical Engineers.

[118] Peskin, C. S. (1972). Flow patterns around heart valves: a numerical method. *Journal of computational physics*, 10(2):252–271.

[119] Peskin, C. S. (2002). The immersed boundary method. *Acta numerica*, 11:479–517.

[120] Piomelli, U. (1997). Large-eddy and direct simulation of turbulent flows.

[121] Plourde, G. and Stenning, A. (1968). Attenuation of circumferential inlet distortion in multistage axial compressors. *Journal of Aircraft*, 5(3):236–242.

[122] Prandtl, L. (1928). L. prandtl, z. angew. math. mech. 8, 85 (1928). *Z. Angew. Math. Mech.*, 8:136–139.

[123] Pullan, G., Young, A. M., and Day, I. J. (2015). Origins and structure of spike-type rotating stall. *ASME J. Turbomach.*, 137(5):051007.

[124] Rao, V. N., Tucker, P., Jefferson-Loveday, R., and Coull, J. (2013). Investigation of wake induced transition in low-pressure turbines using large eddy simulation. In *ASME Turbo Expo 2013: Turbine Technical Conference and Exposition*, pages V06CT42A008–V06CT42A008. American Society of Mechanical Engineers.

[125] RCS, I. (2014). Radome induced vortex shedding. http://itircs.blogspot.co.uk/2014/12/radome-validation-part-2.html. [Online; accessed 01-March-2017].

[126] Reid, C. (1969). The response of axial flow compressors to intake flow distortion. In *ASME 1969 Gas Turbine Conference and Products Show*, pages V001T01A029–V001T01A029. American Society of Mechanical Engineers.

[127] Roach, J., Fisher, T., Frankel, S., Sekar, B., and Kiel, B. (2008). Cfd predictions of damköhler number fields for reduced order modeling of v-gutter flame stability. In *46th AIAA Aerospace Sciences Meeting and Exhibit*, page 509.

[128] Rodi, W. (2017). *Turbulence models and their application in hydraulics*. Routledge.

[129] Roe, P. L. (1986). Characteristic-based schemes for the euler equations. *Annual review of fluid mechanics*, 18(1):337–365.

[130] Rolls-Royce (2014). Advanced and ultrafan programmes. https://www.rolls-royce.com/media/our-stories/innovation/2016/advance-and-ultrafan.aspx.

[131] Sagaut, P. (2002). Les and dns simulation of turbomachinery flows. *Recent developments in numerical methods for turbomachinery flows*, pages 2002–01.

[132] Saiki, E. and Biringen, S. (1996). Numerical simulation of a cylinder in uniform flow: application of a virtual boundary method. *Journal of Computational Physics*, 123(2):450–465.

[133] Sandberg, R. D., Michelassi, V., Pichler, R., Chen, L., and Johnstone, R. (2015). Compressible direct numerical simulation of low-pressure turbines—part i: Methodology. *ASME J. Turbomach.*, 137(5):051011.

[134] Scillitoe, A. D. (2017). *Towards predictive eddy resolving simulations for gas turbine compressors*. PhD thesis, University of Cambridge.

[135] Scillitoe, A. D., Tucker, P. G., and Adami, P. (2015). Evaluation of rans and zdes methods for the prediction of three-dimensional separation in axial flow compressors. In *ASME Turbo Expo 2015: Turbine Technical Conference and Exposition, Montreal, Canada*, pages V02BT39A041–V02BT39A041. American Society of Mechanical Engineers.

[136] Scillitoe, A. D., Tucker, P. G., and Adami, P. (2017). Numerical investigation of three-dimensional separation in an axial flow compressor: The influence of freestream turbulence intensity and endwall boundary layer state. *ASME J. Turbomach.*, 139(2):021011.

[137] Seddon, J. and Goldsmith, E. L. (1999). *Intake aerodynamics*. Amer Inst of Aeronautics &.

[138] Sirovich, L. (1967). Initial and boundary value problems in dissipative gas dynamics. *The Physics of Fluids*, 10(1):24–34.

[139] Sloan, D. G., Smith, P. J., and Smoot, L. D. (1986). Modeling of swirl in turbulent flow systems. *Progress in Energy and Combustion Science*, 12(3):163–250.

[140] Slotnick, J., Khodadoust, A., Alonso, J., Darmofal, D., Gropp, W., Lurie, E., and Mavriplis, D. (2014). CFD vision 2030 study: a path to revolutionary computational aerosciences.

[141] Smagorinsky, J. (1970). Numerical simulation of the global atmosphere. *The Global Circulation of the Atmosphere*, pages 24–41.

[142] Spalart, P. R. (2000). Strategies for turbulence modelling and simulations. *International Journal of Heat and Fluid Flow*, 21(3):252–263.

[143] Sun, X., Jiang, Y., Liang, A., and Jing, X. (2012). An immersed boundary computational model for acoustic scattering problems with complex geometries. *The Journal of the Acoustical Society of America*, 132(5):3190–3199.

[144] Sun, X., Ma, Y., Liu, X., and Sun, D. (2016). Flow stability model of centrifugal compressors based on eigenvalue approach. *AIAA Journal*.

[145] Svehla, R. A. (1962). Estimated viscosities and thermal conductivities of gases at high temperatures.

[146] Tang, Y., Liu, Y., and Lu, L. (2018). Solidity effect on corner separation and its control in a high-speed low aspect ratio compressor cascade. *International Journal of Mechanical Sciences*, 142:304–321.

[147] Temmerman, L., Leschziner, M. A., Mellen, C. P., and Fröhlich, J. (2003). Investigation of wall-function approximations and subgrid-scale models in large eddy simulation of separated flow in a channel with streamwise periodic constrictions. *International Journal of Heat and Fluid Flow*, 24(2):157–180.

[148] Tucker, P. (2011). Computation of unsteady turbomachinery flows: Part 1—progress and challenges. *Progress in Aerospace Sciences*, 47(7):522–545.

[149] Tucker, P. (2013). *Unsteady computational fluid dynamics in aeronautics*, volume 104. Springer Science & Business Media.

[150] Tucker, P. and Liu, Y. (2006). Turbulence modeling for flows around convex features. In *44th AIAA Aerospace Sciences Meeting and Exhibit*, page 716.

[151] Tucker, P. and Liu, Y. (2007). Turbulence modeling for flows around convex features giving rapid eddy distortion. *International Journal of Heat and Fluid Flow*, 28(5):1073–1091.

[152] Tucker, P. G. (2016). *Advanced computational fluid and aerodynamics*, volume 54. Cambridge University Press.

[153] Tyacke, J., Tucker, P., Jefferson-Loveday, R., Vadlamani, N. R., Watson, R., Naqavi, I., and Yang, X. (2014). Large eddy simulation for turbines: methodologies, cost and future outlooks. *ASME J. Turbomach.*, 136(6):061009.

[154] Tyacke, J. C., Mahak, M., and Tucker, P. G. (2016). Large-scale multifidelity, multiphysics, hybrid reynolds-averaged navier–stokes/large-eddy simulation of an installed aeroengine. *Journal of Propulsion and Power*, pages 997–1008.

[155] Ubald, B. N., Tucker, P. G., and Shahpar, S. (2017). Assessment of rans modelling for a complex stagnation probe case. In *55th AIAA Aerospace Sciences Meeting*, page 1229.

[156] Übelacker, S., Hain, R., and Kähler, C. J. (2016). Flow investigations in a stalling nacelle inlet under disturbed inflow. In *Advances in Simulation of Wing and Nacelle Stall*, pages 271–283. Springer.

[157] Udaykumar, H., Mittal, R., Rampunggoon, P., and Khanna, A. (2001). A sharp interface cartesian grid method for simulating flows with complex moving boundaries. *Journal of Computational Physics*, 174(1):345–380.

[158] Utturkar, Y., Mittal, R., Rampunggoon, P., and Cattafesta, L. (2002). Sensitivity of synthetic jets to the design of the jet cavity. In *40th AIAA Aerospace Sciences Meeting & Exhibit*, page 124.

[159] Vadlamani, N. R. (2014). *Numerical investigation of separated flows in low pressure turbines*. PhD thesis, University of Cambridge.

[160] Vaz, G., Pereira, F., and Eça, L. (2017). On the prediction of shear-layer flows with rans and srs models. In *Proceedings of the VII International Conference on Computational Methods in Marine Engineering (MARINE), Nantes, France*.

[161] Viecelli, J. A. (1969). A method for including arbitrary external boundaries in the mac incompressible fluid computing technique. *Journal of Computational Physics*, 4(4):543–551.

[162] Vreman, B., Geurts, B., and Kuerten, H. (1995). Subgrid-modelling in les of compressible flow. *Applied scientific research*, 54(3):191–203.

[163] Wang, D., Lu, L., and Li, Q. (2009). Improvement on sa model for predicting corner separation based on turbulence transport nature. In *45th AIAA/ASME/SAE/ASEE Joint Propulsion Conference & Exhibit*, page 4931.

[164] Wang, Z.-N., Tyacke, J., and Tucker, P. (2018). Large eddy simulation of serration effects on an ultra-high-bypass-ratio engine exhaust jet. *Comptes Rendus Mécanique*, 346(10):964–977.

[165] Wang, Z.-N., Tyacke, J., Tucker, P., and Boehning, P. (2019). Parallel computation of aeroacoustics of industrially relevant complex-geometry aeroengine jets. *Computers & Fluids*, 178:166–178.

[166] Wang, Z.-N. and Yuan, X. (2013). Unsteady mechanisms of compressor corner separation over a range of incidences based on hybrid les/rans. In *ASME Turbo Expo 2013: Turbine Technical Conference and Exposition*, pages V06AT35A030–V06AT35A030. American Society of Mechanical Engineers.

[167] Wartzek, F., Brandstetter, C., Holzinger, F., and Schiffer, H. (2015). Response of a transonic compressor to a massive inlet distortion. In *European Turbomachinery Conference, Madrid, Spain, Mar*, pages 23–27.

[168] Wartzek, F., Holzinger, F., Brandstetter, C., and Schiffer, H.-P. (2016). Realistic inlet distortion patterns interacting with a transonic compressor stage. In *Advances in Simulation of Wing and Nacelle Stall*, pages 285–302. Springer.

[169] Watson, R., Cui, J., Ma, Y., and Hield, P. (2017). Improved hierarchical modelling for aerodynamically coupled systems. In *ASME Turbo Expo 2017: Turbine Technical Conference and Exposition, Charlotte, USA*. American Society of Mechanical Engineers.

[170] Wenren, Y., Fan, M., Dietz, W., Hu, G., Braun, C., Steinhoff, J., and Grossman, B. (2001). Efficient eulerian computation of realistic rotorcraft flows using vorticity confinement-a survey of recent results. In *39th Aerospace Sciences Meeting and Exhibit*, page 996.

[171] Weymouth, G. D. and Yue, D. K. (2011). Boundary data immersion method for cartesian-grid simulations of fluid-body interaction problems. *Journal of Computational Physics*, 230(16):6233–6247.

[172] Wilcox, D. C. (1988a). Multiscale model for turbulent flows. *AIAA journal*, 26(11):1311–1320.

[173] Wilcox, D. C. (1988b). Reassessment of the scale-determining equation for advanced turbulence models. *AIAA journal*, 26(11):1299–1310.

[174] Wilcox, D. C. (2008). Formulation of the kw turbulence model revisited. *AIAA journal*, 46(11):2823–2838.

[175] Williams, J. F. (1973). Technical evaluation report. In *AGARD Conference Proceedings No. 131, On Noise Mechanisms*.

[176] Woodward, P., Porter, D., and Jacobs, M. (2003). 3-d simulations of turbulent compressible stellar convection. In *3D Stellar Evolution*, volume 293, page 45.

[177] Xu, L. (2002). Assessing viscous body forces for unsteady calculations. In *ASME Turbo Expo 2002: Power for Land, Sea, and Air*, pages 323–331. American Society of Mechanical Engineers.

[178] Xu, S. and Wang, Z. J. (2006). Systematic derivation of jump conditions for the immersed interface method in three-dimensional flow simulation. *SIAM Journal on Scientific Computing*, 27(6):1948–1980.

[179] Yan, H., Liu, Y., Li, Q., and Lu, L. (2018). Turbulence characteristics in corner separation in a highly loaded linear compressor cascade. *Aerospace Science and Technology*, 75:139–154.

[180] Yap, C. R. (1987). Turbulent heat and momentum transfer in recirculating and impinging flows.

[181] You, D., Wang, M., Moin, P., and Mittal, R. (2007). Large-eddy simulation analysis of mechanisms for viscous losses in a turbomachinery tip-clearance flow. *Journal of Fluid Mechanics*, 586:177–204.

Appendix A

eIBMl for Flow Frequencies

The eIBMl is also applied to capture the key frequencies in the scenario of fan-intake interaction. This is investigated via the simplified case of a 22.5° sector extracted from the Darmstadt Rotor with a single rotor. The case uses 8.6 M mesh nodes and is performed using implicit LES. Data are collected for around 10 flow throughs when the simulation is statistically steady. These data are recorded by three probes (Fig.A.1) placed near the shear layer $P1$, in the center of the bubble $P2$, and outside of the separation region $P3$ (close to the blade leading edge).

Figure A.2 depicts the iso-surface of the Q-criterion at 1×10^6 colored according to the static pressure. It can be seen that massive turbulence is generated by the beam in the upstream that then interacts with the downstream rotor. The rotor blade is also modelled by the eIBMl. Compared to the eIBMg case using LES, the separation bubble is larger and still exists within the blade passage (see Fig.A.3). This means that the modelling of fan blade has a substantial effect on the separation prediction. The dilation (divergence of velocity) is calculated to show the sound propagation. Due to the continuity equation

$$\frac{D\rho}{Dt} + \rho\nabla \cdot \boldsymbol{v} = 0, \tag{A.1}$$

the dilation denotes a density changing rate, and hence the pressure wave propagation shown in Fig. A.4. The turbulence from the beam encounters the rotor blade tip and then generates noise towards the upstream.

The time series data were collected via three probes (see Fig. A.1) and transformed by Fast Fourier Transform (FFT) , as shown in Fig.A.5. The time was non-dimensionalised by the period for one revolution ($T = 65\%/n_r$, $f_0 = 216.78Hz$) and the sampling time was the time step for the explicit scheme ($\Delta t = 3.72 \times 10^{-8}$). The lowest peak $f_s = 6.63f_0$ was detected by all the probes in Fig.A.5. Thus the

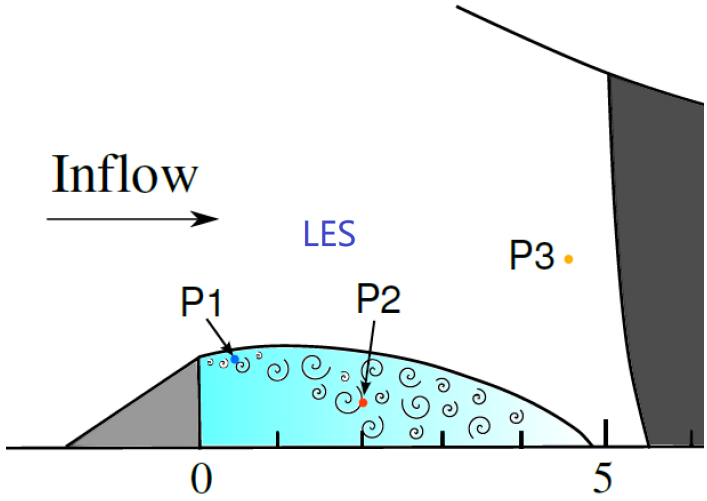

Fig. A.1 22.5° sector Case: probes for flow frequency collection

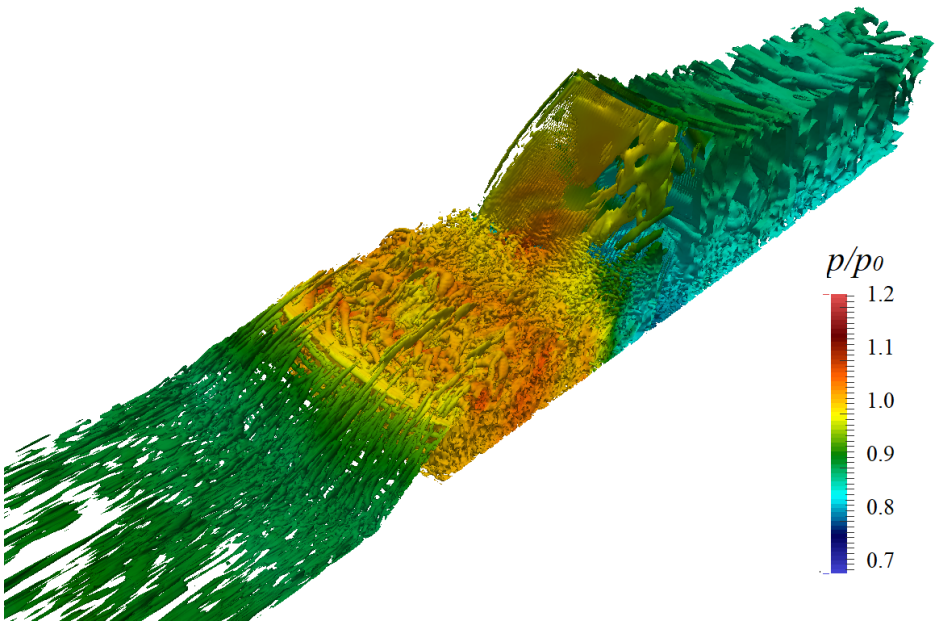

Fig. A.2 Iso-surface of Q-criterion 1×10^6 for the sector case, coloured by static pressure

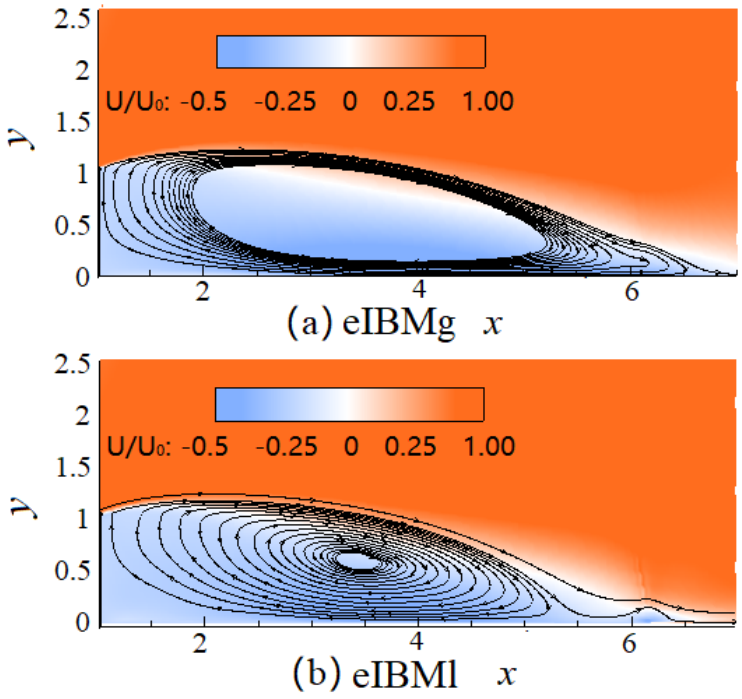

Fig. A.3 Separation bubbles predicted by eIBMg and eIBMl

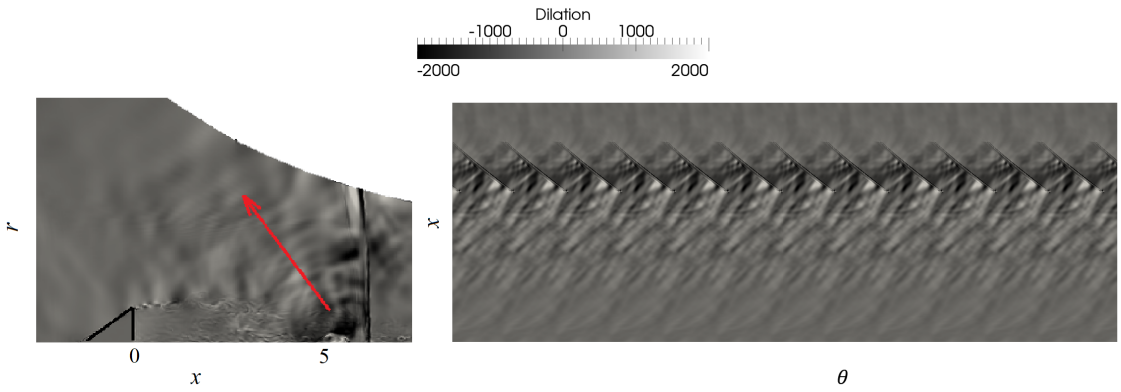

Fig. A.4 Contours of the dilation in $x-r$ and $x-\theta$ domains

Strouhal number can be calculated to be $St = f_s H/U_0 \approx 0.240$, where H is the height of the beam and U_0 is the velocity of main flow near the beam edge. This frequency f_s corresponds to the vortex shedding frequency. The second and higher frequency peaks $f_b = 16.51 f_0$, is only detected by Probe 3 and quite close to the theoretical blade passing frequency $16 f_0$. The other peaks $32.16 f_0$, $47.29 f_0$, $64.31 f_0$, etc. correspond to the harmonics $f_n = nNr f_0$, where $n = 1, 2, 3...$ and N_r is the number of rotor blades. However, these peaks were not found in other probes because they are within the separation and also further to the blade. These results indicate that the eIBMl

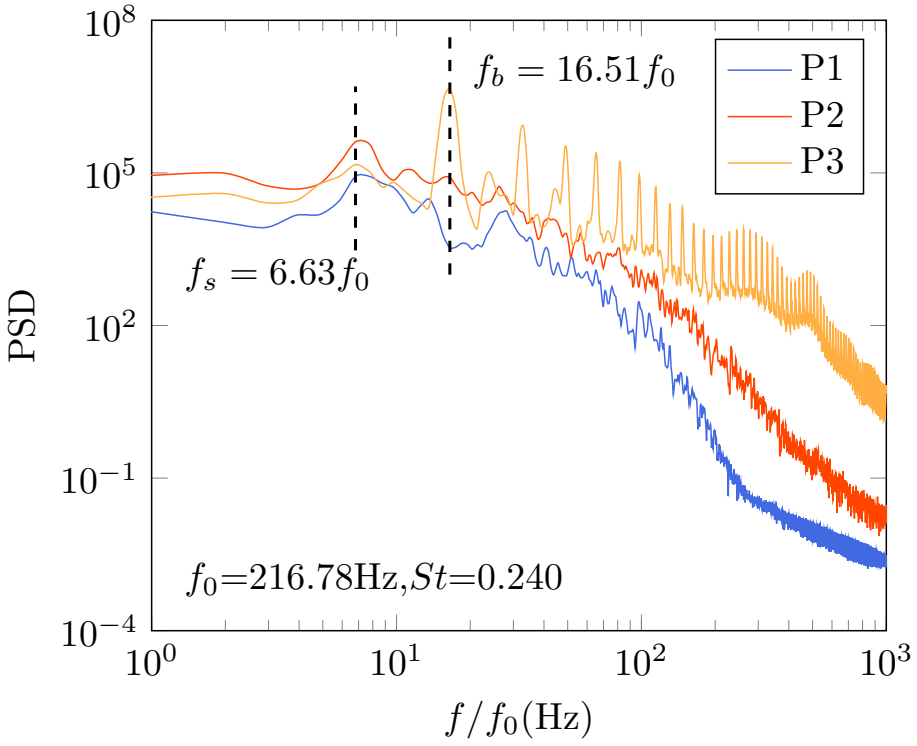

Fig. A.5 Flow frequencies around/within the separation bubble

can successfully provide accurate information about the wave propagation. This is a significant improvement to eIBMg.

Appendix B

Discrepancy between RANS and LES

The discrepancy between RANS and LES in the fan-intake scenario can be explained from the turbulence equations of the $k-\omega$ model, which is

$$\begin{aligned} \frac{\partial(\rho k)}{\partial t} + \frac{\partial(\rho u_j k)}{\partial x_j} &= \mathcal{P} - \mathcal{D}(k,\omega) + \mathcal{F}(k,\omega) \\ \frac{\partial(\rho \omega)}{\partial t} + \frac{\partial(\rho u_j k)}{\partial x_j} &= \frac{\gamma\omega}{k}\mathcal{P} - \mathcal{D}(k,\omega) + \mathcal{F}(k,\omega). \end{aligned} \tag{B.1}$$

These equations indicate that the difference may come from the production term $\mathcal{P} = -\rho\overline{u_i' u_j'}\dfrac{\partial U_i}{\partial x_j}$. As a eddy viscosity model, it assumes that Reynolds stresses are proportional to the strain tensor.

$$\begin{aligned} -\rho\overline{u_i' u_j'} &= 2\mu_t S_{ij} - \frac{2}{3}k\delta_{ij}, \\ S_{ij} &= \frac{1}{2}\left(\frac{\partial U_i}{\partial x_j} + \frac{\partial U_j}{\partial x_i}\right), \\ \mu_t &= \rho k/\omega \end{aligned} \tag{B.2}$$

Hence, the problem could either be associated with this linear relation between the stresses and strains or from the incorrect strain tensor S_{ij} field. To clarify this point, we fix the velocities according to LES results and repeat the case with the $k-\omega$ model. This strategy is inspired by the work of Gao and Liu et al [53]. Figure B.1 reveals that, even if the strain tensor is the same as the LES case, the TKE values are still differ significantly; the RANS result is almost three times higher than the LES value.

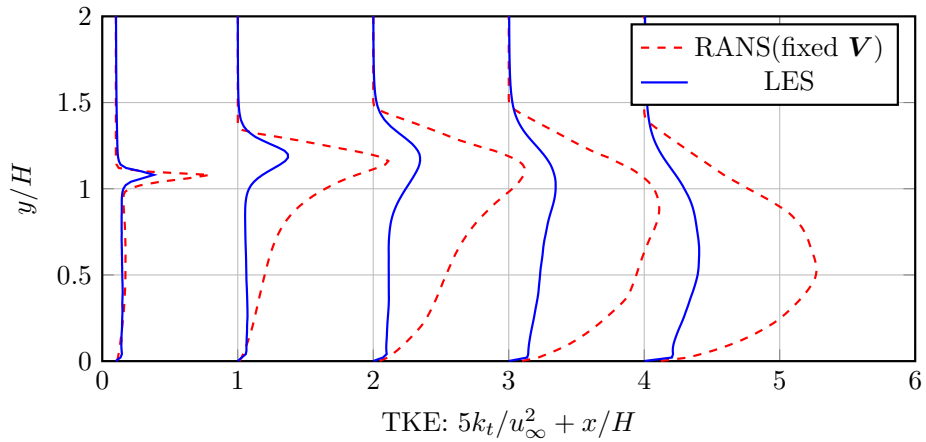

Fig. B.1 Comparison of TKE profiles obtained from LES against RANS (with frozen velocity field from LES), for the case 'Duct H'

This is because the velocity gradient $\dfrac{\partial U}{\partial y}$ is the dominant term in the TKE production within the reversed flow. When estimated by RANS, the stress $\mu_t \dfrac{\partial U}{\partial y}$ is higher than the actual stress $\rho\overline{u'v'}$. Hence, the production of TKE in RANS with fixed velocity also increases. This increase is approximately quadratic since $\mathcal{P}_{12} = \mu_t \left(\dfrac{\partial U}{\partial y}\right)^2$.

Hence, we may conclude that this linear relation is not applicable for this separated flow. According to Craft et al. [33], the result can be improved by adding a quadratic term to Equation B.2, which is aimed at reducing the production. On the other hand, turbulence models are constructed based on the local equilibrium between turbulence production and destruction; however, when separation occurs, this equilibrium state could be destroyed and strong non-equilibrium turbulence could then dominate [179]. Based on this concept, Liu et al. [90] made a first attempt to modify a turbulence model using helicity in order to take account of the turbulence energy backscatter when considering turbulence non-equilibrium in vortical flows. They modified the SA model using helicity, and the results showed that the modified SA model was able to significantly improve the predictive accuracy when simulating corner separation flow in compressors [146]. Recently, the modified SA model was also successfully used to predict the behaviour of fan flows at off-design conditions [78].